(NASA-CR-4186) TRANSONIC AEROELASTIC ANALYSIS OF LAUNCH VEHICLE CONFIGURATIONS Ph.D. Thesis (Stanford Univ.) 167 p
CSCL 01A
N89-14215
Unclas
H1/02 0166294

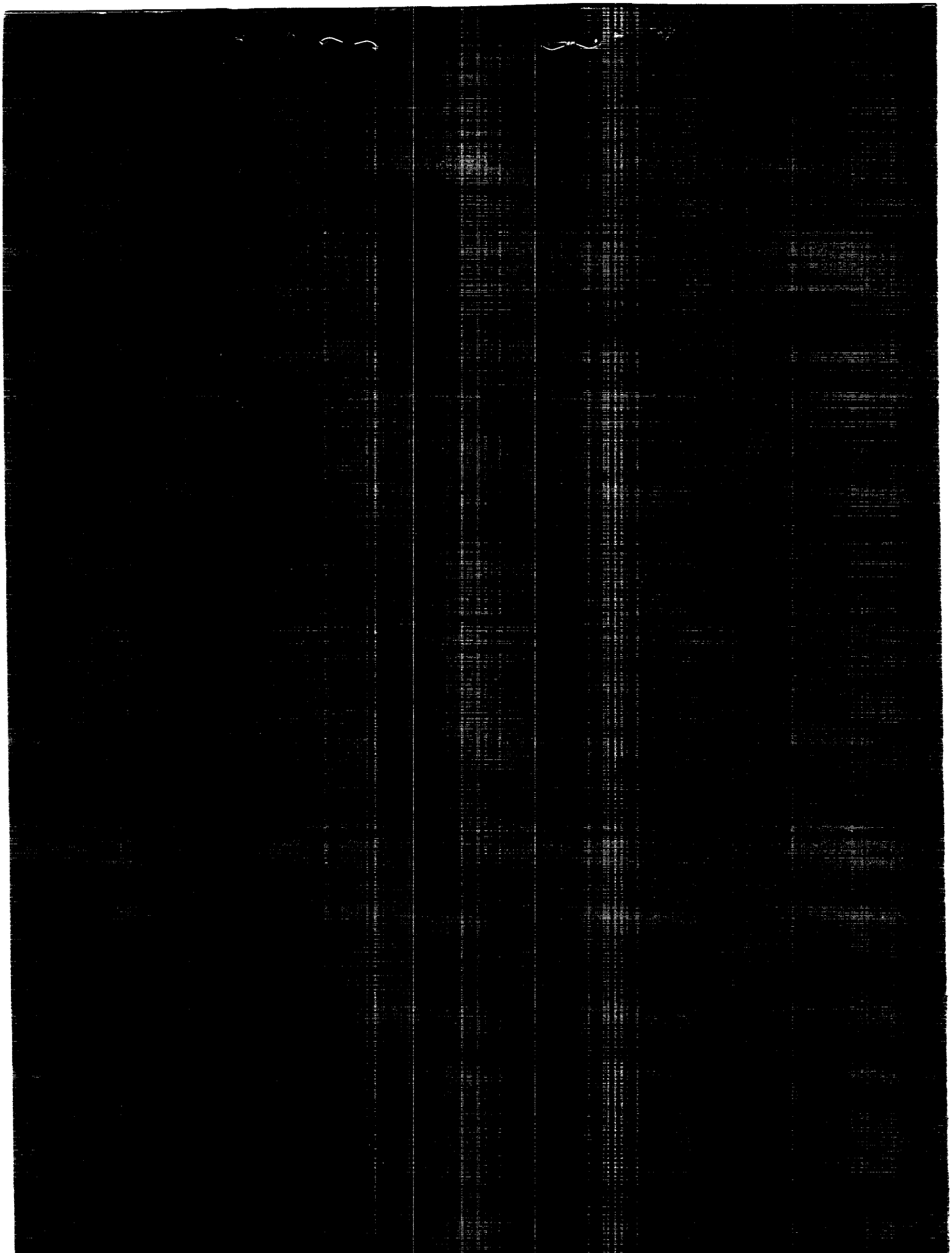

NASA Contractor Report 4186

# Transonic Aeroelastic Analysis of Launch Vehicle Configurations

João Luiz Filgueiras de Azevedo
*Stanford University*
*Stanford, California*

Prepared for
Langley Research Center
under Grant NGL 05-020-243

National Aeronautics
and Space Administration

**Scientific and Technical
Information Division**

**1988**

# Contents





PAGE 11 INTENTIONALLY BLANK

PRECEDING PAGE BLANK NOT FILMED

# List of Figures

*LIST OF FIGURES*

*LIST OF FIGURES*

*LIST OF FIGURES*

# List of Principal Symbols

| | |
|---|---|
| $a$ | speed of sound |
| $a_\infty$ | freestream speed of sound |
| $A$ | flux Jacobian matrix associated with the $\xi$-direction |
| $\hat{A}$ | inviscid part of flux Jacobian matrix $A$ |
| $B$ | flux Jacobian matrix associated with the $\eta$-direction |
| $\hat{B}$ | inviscid part of flux Jacobian matrix $B$ |
| $C$ | flux Jacobian matrix associated with the $\zeta$-direction |
| $\hat{C}$ | inviscid part of flux Jacobian matrix $C$ |
| $Cp$ | pressure coefficient, $\frac{2}{\gamma M_\infty^2}\left(\frac{p}{p_\infty}-1\right)$ |
| $C_p$ | specific heat at constant pressure |
| $C_v$ | specific heat at constant volume |
| $d$ | body diameter |
| $e$ | total energy per unit of volume of the fluid |
| $e_i$ | specific internal energy of the fluid |
| $E$ | flux vector in the $x$-direction |
| $\overline{E}$ | flux vector in the $\xi$-direction |
| $EI(x)$ | bending stiffness |
| $F$ | flux vector in the $y$-direction |
| $\overline{F}$ | flux vector in the $\eta$-direction |
| $F(\eta)$ | function used in outer region of turbulence model |
| $F_{Klab}(\eta)$ | Klebanoff intermittency factor |

| | |
|---|---|
| $F_z(x,t)$ | lateral external load |
| $G$ | flux vector in the $z$-direction |
| $\overline{G}$ | flux vector in the $\zeta$-direction |
| $\vec{G}$ | fluid body forces |
| $h$ | enthalpy of the fluid |
| $H$ | total enthalpy of the fluid |
| $I$ | identity matrix |
| $J$ | Jacobian of the transformation |
| $k$ | reduced frequency; constant in turbulence model |
| $l$ | length scale for inner region of turbulence model |
| $\ell_0$ | reference length |
| $\ell_b$ | dimensionless body length |
| $\ell(x,t)$ | dimensionless running normal force |
| $L_\xi$, $L_\eta$, $L_\zeta$ | left-hand side finite difference operators |
| $m(x)$ | mass per unit of body length |
| $\overline{m}_i$ | nondimensional generalized mass of the $i$-mode |
| $\tilde{m}_i$ | (dimensional) generalized mass of the $i$-mode |
| $M$ | Mach number |
| $M_\infty$ | freestream Mach number |
| $\hat{M}_\xi$ | viscous part of the flux Jacobian matrix $A$ |
| $\hat{M}_\eta$ | viscous part of the flux Jacobian matrix $B$ |
| $\hat{M}_\zeta$ | viscous part of the flux Jacobian matrix $C$ |
| $N$ | number of modes used in the aeroelastic analysis |
| $O$ | order of magnitude |
| $p$ | pressure |
| $p_\infty$ | freestream pressure |
| $P_i$ | generalized aerodynamic force |
| $Pr$ | Prandtl number |
| $Pr_t$ | turbulent Prandtl number |
| $\vec{q}$ | heat flux vector |
| $q_D$ | freestream dynamic pressure |

| | |
|---|---|
| $q_i$ | generalized modal coordinate |
| $q_x$, $q_y$, $q_z$ | cartesian components of the heat flux vector |
| $Q$ | vector of conserved quantities (cartesian coordinates); heat addition |
| $\overline{Q}$ | vector of conserved quantities (body-conforming coordinates) |
| $R$ | characteristic gas constant for air |
| $Re$ | freestream Reynolds number |
| $Re_D$ | freestream Reynolds number based on reference diameter |
| $R_\xi$, $R_\eta$, $R_\zeta$ | right-hand side finite difference operators |
| $t$ | time |
| $\Delta t$ | computational time step |
| $T$ | temperature |
| $T_p$ | period of integration for averaging the equations |
| $u$ | $x$-component of fluid velocity in the cartesian coordinate system |
| $u_\infty$ | freestream $x$-component of fluid velocity |
| $u_i$, $u_j$ | velocity components in cartesian coordinates, ($i$, $j = 1, 2, 3$) |
| $U_\infty$ | magnitude of the freestream velocity vector |
| $U$, $V$, $W$ | contravariant velocity components |
| $v$ | $y$-component of fluid velocity in the cartesian coordinate system |
| $v_\infty$ | freestream $y$-component of fluid velocity |
| $w$ | $z$-component of fluid velocity in the cartesian coordinate system |
| $w_\infty$ | freestream $z$-component of fluid velocity |
| $x$, $y$, $z$ | cartesian coordinates |
| $\alpha$ | angle of attack |
| $\beta_x$, $\beta_y$, $\beta_z$ | expressions that contain the viscous terms in the energy equation |
| $\gamma$ | ratio of specific heats |
| $\delta(x,t)$ | total deflection of the centerline |
| $\delta_\xi$, $\delta_\eta$, $\delta_\zeta$ | central difference operators |
| $\Delta_\xi$, $\Delta_\eta$, $\Delta_\zeta$, $\Delta_t$ | forward difference operators |
| $\nabla_\xi$, $\nabla_\eta$, $\nabla_\zeta$ | backward difference operators |
| $\epsilon_E$ | artificial dissipation coefficient for explicit side |
| $\epsilon_I$ | artificial dissipation coefficient for implicit side |

| | |
|---|---|
| $\zeta$ | circumferential coordinate in body conforming system |
| $\zeta_i$ | modal damping coefficient |
| $\eta$ | normal coordinate in body conforming system |
| $\theta(t)$ | rigid body centerline angular deflection |
| $\theta_0$ | half-amplitude angle of the oscillation |
| $\kappa$ | coefficient of thermal conductivity |
| $\lambda$ | second coefficient of viscosity |
| $\mu$ | viscosity coefficient; effective viscosity coefficient |
| $\mu_\infty$ | freestream viscosity coefficient |
| $\mu_\ell$ | molecular (laminar) viscosity coefficient |
| $\mu_t$ | eddy (turbulent) viscosity coefficient |
| $\nu_i$ | generalized modal velocity |
| $\xi$ | longitudinal coordinate in body conforming system |
| $\rho$ | density |
| $\rho_\infty$ | freestream density |
| $\sigma$ | amplification factor |
| $\tau$ | time in the body conforming system |
| $\tau_{ij}$ | component of the viscous stress tensor, $(i, j = x, y, z)$ |
| $\phi_i(x)$ | normal mode of vibration |
| $\omega$ | frequency |
| $\omega_i$ | natural frequency of the $i$-th mode |
| $\overline{\omega}$ | nondimensional frequency, $\frac{\ell_a \omega}{a_\infty}$ |
| $\lvert\omega\rvert$ | magnitude of vorticity vector |

# Chapter 1

# Introduction

## 1.1 Background

The transonic flight regime has proven to be very difficult to analyze because of the inherent nonlinearities associated with the equations governing the flow at transonic speeds, even in their most simplified form. It is well known that, due to these nonlinearities, small changes in geometry or freestream conditions do not necessarily produce small changes in the flow solution around the vehicle. Particularly for unsteady problems, which is the case in any flutter analysis, the shock motions and variations in the shock strength can be significant even for small oscillations of the body. In some cases shock-boundary layer interaction phenomenon can strongly influence the point of flow separation. Besides being another nonlinear effect, it also means that the position of separation is moving as the shock location and strength vary with the body motion.

These combined problems have, over the years, meant that no methods were developed which can treat general transonic flows. On the other hand, despite all its difficulties, the transonic regime is very important in aeronautical applications. Methods that would be able to perform routine aeroelastic analyses are necessary, since current transport aircraft usually cruise in this regime and military aircraft maneuver in it. Even missiles, or launch vehicles in general, that are designed to acquire a very high speed in a reasonably short time, have to pass safely through

transonic speeds. Such launch vehicles are the focal subject of the present investigation.

From the point of view of the aeroelastician the need to take into consideration the inherent nonlinearities of transonic flow is specially annoying because it prevents his accustomed use of superposition. Of course, this is not to say that one can never find useful linearized solutions in the transonic case. For instance, the work of Landahl [1] shows that if, the reduced frequencies are high enough, linearized equations do a good job of predicting the unsteady aerodynamic forces on streamlined wings and bodies. Another example of linearized transonic solutions can be found in applications of the *indicial method* (e. g. , Ballhaus and Goorjian [2] and Nixon [3]) . This method is a more limited form of superposition in which unsteady aerodynamic solutions are given as linear perturbations about nonlinear steady state solutions. For small amplitudes of body motion and small shock motions, this method has proved to be an acceptable approach to aeroelastic analysis.

For the problems treated here, however, no linearization is possible since the nonlinear nature of the aerodynamic forces is essential to capture the physical phenomena involved. This work undertakes to analyze the aeroelastic stability of ballistic vehicles during their transonic phase of flight. Although the methodology developed can be used for any flight vehicle, the reader will recognize that the particular problems being addressed are most likely to occur on ballistic vehicles (boosters), especially those carrying so-called *hammerhead* payloads. In such cases, the problem can be compounded by the existence of relatively large regions of separated flow.

Since the meaning of a *hammerhead* payload may not be familiar to all readers, it is important to mention that throughout this work the term will denote all those launch vehicles where the payload has a larger diameter than the adjacent booster stage. It is clear that such a configuration will always be associated with some form of boattail right at the front of the booster, which creates the possibility that at least some of the vehicle could be immersed in a region of separated flow.

The interest in such vehicle configurations, as well as in blunt geometries in general, is related to the fact that they are sometimes very attractive options for

the designer. Aeroelastic problems have, however, been observed in the past on certain vehicles with these configurations [4,5,6] when passing through the transonic regime. A study of nonlinear hammerhead effects is presented in considerable detail by Woods and Ericsson [4] for an Atlas-Able IV launch vehicle, which was one of the configurations that actually experienced flutter problems during transonic flight in the early 1960's. Another example where the hammerhead could have been a possible source of aeroelastic instability was the original Seasat-A launch vehicle, as described by Ericsson and Reding [5]. In this case, the solution adopted completely eliminated the hammerhead by enclosing both the payload and the Agena upper stage in a fairing with a diameter equal to the first-stage Atlas booster diameter. Besides true flutter cases, some failures in early launch vehicles may have been associated with buffeting during the transonic phase of flight, as described by Rainey [6] .

The classical approach to the analysis of the aeroelastic phenomena present in the transonic phase of flight of ballistic launch vehicles has been to use experimental data for the unsteady aerodynamic pressures together with some simplified structural-dynamic representation of the vehicle. It is typified by the examples presented in References [4], [5] and [6] . Actually, not only in the analysis of launch vehicle problems but in any situation where transonic and separated flows are present, the usual practice has been to rely on empirical, or semi-empirical, methods for the treatment of the aerodynamic terms, as can be seen from References [7] through [10] . The main difficulty with these analyses is exactly that they require the use of experimental data for the unsteady aerodynamic pressures in order to formulate the aeroelastic problem. In some cases, since unsteady pressure data are not usually available, steady data are adapted in a quasi-steady fashion.

This whole idea of relying entirely on experimental aerodynamic data may be highly undesirable in many situations. For instance, in the early stages of design of a new vehicle, or when some modifications to an existing vehicle have to be made to accommodate a payload with a larger diameter than the booster's uppermost stage, such experimental data are not available. The problem is usually handled

building wind tunnel models, testing them, and modifying the design if aeroelastic problems appear. This can be very expensive during the design cycle, not to mention that it is perhaps another reason the aeroelastician is usually seen as a *policeman* as mentioned by Ashley and co-authors [11]. Thus, the motivation for the present work includes the development of the capability for calculating, as part of the solution, the aerodynamic environment the vehicle is subjected to. Given the necessary aerodynamic tools, the aeroelastic stability analysis can be performed. Eventually, this computational procedure will become sufficiently cost-efficient to be incorporated in the design cycle, at least in the transonic regime where the usual linearized methods break down.

## 1.2 Computational Approach

The recent progress in the field of Computational Fluid Dynamics (CFD) has allowed the simulation of transonic flowfields through the use of finite difference, or finite volume, techniques. However, much more current research is focussed on steady transonic calculations than on unsteady ones. The reason for this is that unsteady calculations, and their aeroelastic applications, require that the equations be solved in a *time-accurate* manner. As a result, the time-step sizes that can be taken in the time integration of the equations are severely restricted and increase considerably the computer cycles required for solution.

There is also the question of at which level of approximation to perform those computations. For some problems, it is sufficient to consider the transonic small disturbance equation, whereas in others a Navier-Stokes formulation would be appropriate. Interesting surveys in this regard, indicating also the stage of development at the time of publication, are presented by Peterson [12] and by McCroskey, Kutler and Bridgeman [13]. It is no surprise that most of the work that can be found in the literature is restricted to airfoil or wing flows. The aerodynamic formulation is restricted to the transonic small disturbance or to the full potential equations, since these formulations are less computationally demanding than more complex ones based on the Euler or the Navier-Stokes equations.

Some examples of applications of CFD methods to unsteady transonic aerodynamic calculations and to aeroelastic analyses, where the aerodynamic formulation is based on the small disturbance or the full potential equations, can be found in References [14]–[30]. The computational requirements, even in those cases, are by no means trivial. Certainly they are already within acceptable limits of present computers, as the work in these references shows. The study of transonic aileron buzz by Steger and Bailey [31] can be considered one of the "classical" examples of the use of CFD for aeroelastic analysis; even before 1980 it employed a Navier-Stokes formulation for the flow solver. A few other cases, where similar complex formulations are used, can also be found in the literature. For example, References [32] and [33] include applications of Euler equations, but still to airfoil or wing problems.

The main difficulty when one starts to consider transonic aeroelastic problems of bodies is that usually the disturbances are large enough that a potential formulation is no longer adequate. Furthermore, the description of the aerodynamic phenomena important to the aeroelastic analysis, such as the topology of flow separation or shock-boundary layer interactions, may be beyond the scope of potential methods. In other words, one has to resort to the Euler or Navier-Stokes equations in order to appropriately simulate the physical flow features involved [34]. For these cases very little has actually been published, although the idea of how one should proceed to perform aeroelastic analysis is somewhat well established [35]. The computational requirements, both in terms of time and storage, are the major challenge, since grid systems that would support a Navier-Stokes solution for typical launch vehicle shapes are bound to be large, and CPU times associated with unsteady transonic Navier-Stokes solutions are also substantial.

## 1.3 The Present Method

The approach followed in the present work uses CFD techniques to perform aeroelastic analyses of launch vehicle configurations by coupling the structural-dynamic equations representing the vehicle with an unsteady flow solver appropriate for the physical situation being treated.

The mechanism underlying the aeroelastic instabilities observed in flight involves the existence of phase lags between the aerodynamic forces and the motion. In such circumstances, these loads can do positive work on the oscillating vehicle. For launch vehicle configurations, the accurate calculation of these lags involves resolving the important features of the flow, which include transonic shocks and their motion, shock-boundary layer interactions, and shock-induced flow separation. The problem of flow separation is particularly important for hammerhead configurations, where the existence of merged regions of separation [5] can have a definite influence on the vehicle's aeroelastic stability. In summary, then, we can conclude that the aeroelastic phenomena observed in flight indicate that, in the case of the ballistic vehicles being emphasized here, the correct flow equations that should be used are the Navier-Stokes equations.

The coupling of the two sets of equations is performed by integrating both of them simultaneously in time and ensuring that the data generated by one set is used in the next time step of the other. The aerodynamic equations are solved in a time-accurate fashion, and their solution provides the forcing terms for the aeroelastic analysis, which typically are weighted integrals of the pressure distribution along the body surface. Solution of the structural-dynamic equations gives the new deformed shape of the body, and so the boundary conditions for the aerodynamic solution at the next time step.

The subject of *time-accuracy* of the aerodynamic equations deserves a more detailed discussion. A solution would be considered *time-accurate* in a numerical sense if all the scales supported by the computational mesh are being accurately resolved, which in practical terms implies that the CFL number is at most of the order one everywhere in the computational domain. Since the CFL, or Courant, number can be interpreted as the ratio of the length scale obtained by the product of some characteristic velocity times the time step over the length scale determined by the grid size, it is clear that this is a very restrictive condition in terms of the maximum steps sizes that could be used. This is not the meaning we intend to assign to this expression in the present work. Here, the solution is being called *time-accurate*

in an aerodynamic sense, meaning that all the important aerodynamic phenomena of interest are being resolved accurately. Since the time scales associated with the structural-dynamic phenomena we will be studying here are much larger than those associated with the pure aerodynamic phenomena, as we will demonstrate later, by enforcing time-accuracy in an aerodynamic sense we automatically have time-accuracy in an aeroelastic sense.

Since full solution of the Navier-Stokes equations around complex geometries is still beyond our computational capabilities, the method employed here solves the thin layer approximation to the Reynolds-Averaged Navier-Stokes equations, where turbulence closure is obtained by using an algebraic eddy viscosity model. Before the aeroelastic analysis could be started, the aerodynamic equations must be marched in time in order to obtain an initial *steady state* solution for the flow around the body, assuming that it does not deform under the loads. Once this initial solution is obtained, one can start to oscillate the body and, from then on, the aerodynamic solution must be time-accurate since the flow solver will be coupled to the structural-dynamic equations as previously described. By tracing the growth or decay of a perturbed oscillation, the aeroelastic stability of a given configuration can be ascertained.

In the following chapters, the formulation of the problem and the detailed description of the method will be presented, together with the results obtained in the various cases analyzed. The theoretical formulation that underlies the present approach will be presented in Chapters 2 and 3 . Chapters 4 through 6 will describe several applications of the method, both for unsteady aerodynamic calculations as well as aeroelastic analyses. Finally, Chapter 7 will summarize the possible contributions of the present research, present its conclusions, and discuss some recommendations for future work.

# Chapter 2

# Formulation of the Aerodynamic Problem

## 2.1 The Navier-Stokes Equations

In order to correctly represent the physical phenomena present in this problem, the appropriate set of flow equations to be used are the Navier-Stokes equations. These equations can be written in differential form [36] as :

continuity equation:

$$\frac{D\rho}{Dt} + \rho \nabla . \vec{u} = 0 \tag{2.1}$$

conservation of momentum equations:

$$\rho \frac{D\vec{u}}{Dt} = -\nabla p + \nabla . \bar{\bar{\tau}} + \rho \vec{G} \tag{2.2}$$

energy equation:

$$\rho \frac{DH}{Dt} = \frac{\partial p}{\partial t} + \nabla . [\bar{\bar{\tau}} . \vec{u} - \vec{q}] + \rho \vec{G} . \vec{u} + Q \tag{2.3}$$

where the symbol $D/Dt$ indicates the *substantial* or *material derivative*, the vector $\vec{G}$ represents the body forces, and $Q$ is the heat addition.

The set of equations above requires some constitutive relations in order to form a *closed* system of equations. Starting with the equation of state, a perfect gas [37] is assumed such that one can write

$$p = \rho RT = (\gamma - 1)\, \rho e_i \tag{2.4}$$

where the specific internal energy of the fluid, $e_i$, is given by

$$e_i = C_v T \tag{2.5}$$

The heat flux vector is given by the Fourier law of heat conduction

$$\vec{q} = -\kappa(\nabla T) \tag{2.6}$$

The components of the viscous stress tensor, $\bar{\bar{\tau}}$ , can be obtained from

$$\tau_{ij} = \mu\left(\frac{\partial u_i}{\partial x_j} + \frac{\partial u_j}{\partial x_i}\right) - \frac{2}{3}\mu(\nabla.\vec{u})\,\delta_{ij} \tag{2.7}$$

where we are considering an isotropic fluid and also that the coefficient of bulk viscosity $\lambda$ is simply given by: $\lambda = -\frac{2}{3}\mu$ . Finally, the total enthalpy of the fluid, $H$, is defined as

$$H = h + \frac{1}{2}|\vec{u}|^2 = e_i + \frac{p}{\rho} + \frac{1}{2}|\vec{u}|^2 \tag{2.8}$$

where for a perfect gas one can also write the enthalpy $h = C_p T$ .

Equations 2.1, 2.2 and 2.3 are written in the non-conservation form. This may create numerical problems when computing flow quantities across a shock wave, since the use of the non-conservation form can cause loss, or creation, of mass and momentum across the shock. So, from a numerical point of view, it is very important to recast this set of equations in the conservation-law form, or divergent form. Before doing that, however, we will introduce the assumptions that in the problems being treated here there are no body forces $\left(\vec{G} = 0\right)$ and no heat addition $(Q = 0)$ . It probably should be pointed out that the *body forces* which we are referring to here are field effects such as gravity, for example. The introduction of these assumptions is not a necessary step at this point in the formulation. However, since they would be invoked later anyway, one might as well use them now and simplify the algebra. It should be noted that the reason for using the above assumptions is physical, i. e. , in the flight regime being treated the contribution of the terms being disregarded is indeed negligible.

Rewriting Equations 2.1–2.3 in index notation, with the repeated-index implying summation, and remembering that the substantial derivative is given by

$$\frac{D(\,)}{Dt} = \frac{\partial(\,)}{\partial t} + \vec{u}.\nabla(\,) \tag{2.9}$$

one obtains the following equations :

$$\frac{\partial \rho}{\partial t} + u_j \frac{\partial \rho}{\partial x_j} + \rho \frac{\partial u_j}{\partial x_j} = 0 \tag{2.10}$$

$$\rho \left[ \frac{\partial u_i}{\partial t} + u_j \frac{\partial u_i}{\partial x_j} \right] = -\frac{\partial p}{\partial x_i} + \frac{\partial \tau_{ij}}{\partial x_j} \tag{2.11}$$

$$\rho \left[ \frac{\partial H}{\partial t} + u_j \frac{\partial H}{\partial x_j} \right] = \frac{\partial p}{\partial t} + \frac{\partial}{\partial x_j} [\tau_{ij} u_i - q_j] \tag{2.12}$$

Defining the total energy per unit of volume, $e$ , as

$$e \equiv \rho \left[ e_i + \frac{1}{2} u_j u j \right] \tag{2.13}$$

the equations can be written in the conservation-law form in the following way,

continuity:
$$\frac{\partial \rho}{\partial t} + \frac{\partial}{\partial x_j} (\rho u_j) = 0 \tag{2.14}$$

momentum:
$$\frac{\partial (\rho u_i)}{\partial t} + \frac{\partial (\rho u_i u_j)}{\partial x_j} + \frac{\partial p}{\partial x_i} - \frac{\partial \tau_{ij}}{\partial x_j} = 0 \tag{2.15}$$

energy:
$$\frac{\partial e}{\partial t} + \frac{\partial}{\partial x_j} [(e + p) u_j - \tau_{ij} u_i + q_j] = 0 \tag{2.16}$$

Full solution of Equations 2.14–2.16 around complex geometries is still beyond our computational capabilities, since the number of grid points required to capture all the scales of a turbulent flow at flight Reynolds numbers would be prohibitive. The alternative approach consists then in averaging the flow variables such that they can be expressed as a mean flow quantity plus a zero-mean perturbation. In particular, if a mass weighted averaging is used, it is possible to rewrite the equations in terms of the averaged quantities *almost* in the same form as Equations 2.14–2.16 . A generic quantity $z$ is averaged such that

$$z = \overline{z} + z' \tag{2.17}$$

where : $\overline{z} \equiv \frac{1}{T_p} \int_{t_0}^{t_0 + T_p} z \, dt$

Here the period of integration $T_p$ should be small compared to the time scale for

variations in the mean flow quantities but should be large enough to provide some averaging over the high frequency turbulent scales.

The flow variables can be written as:

$$\begin{aligned} \rho &= \overline{\rho} + \rho' \\ \rho u_i &= \overline{\rho u_i} + (\rho u_i)' \\ e &= \overline{e} + e' \\ p &= \overline{p} + p' \\ \tau_{ij} &= \overline{\tau}_{ij} + \tau'_{ij} \\ q_i &= \overline{q}_i + q'_i \\ \rho H &= \overline{\rho H} + (\rho H)' \\ \rho h &= \overline{\rho h} + (\rho h)' \end{aligned} \tag{2.18}$$

However, if averaged velocities are necessary, for example, some other form of averaging is required, since the quantity that was averaged above is the momentum. So, for quantities like velocity and enthalpy, another average is defined as

$$\begin{aligned} \tilde{u}_i &\equiv \overline{\rho u_i}/\overline{\rho} \\ \tilde{h} &\equiv \overline{\rho h}/\overline{\rho} \end{aligned} \tag{2.19}$$

and with these new definitions one could write

$$\begin{aligned} u_i &= \tilde{u}_i + u''_i \\ h &= \tilde{h} + h'' \end{aligned} \tag{2.20}$$

It is important to note, however, that perturbation quantities such as $u''_i$ and $h''$ do not necessarily have zero mean value.

If we perform the averaging process on Equations 2.14–2.16 , the following governing equations are obtained,
continuity:

$$\frac{\partial \overline{\rho}}{\partial t} + \frac{\partial}{\partial x_j}(\overline{\rho}\tilde{u}_j) = 0 \tag{2.21}$$

momentum:

$$\frac{\partial}{\partial t}(\overline{\rho}\tilde{u}_i) + \frac{\partial}{\partial x_j}(\overline{\rho}\tilde{u}_i\tilde{u}_j) + \frac{\partial \overline{p}}{\partial x_i} - \frac{\partial}{\partial x_j}\left(\overline{\tau}_{ij} - \overline{\rho u_i'' u_j''}\right) = 0 \tag{2.22}$$

energy:

$$\frac{\partial \overline{e}}{\partial t} + \frac{\partial}{\partial x_j}\left[\left(\overline{e} + \overline{p}\right)\tilde{u}_j\right] + \frac{\partial}{\partial x_j}\left(\overline{\rho u_j'' h}\right)$$

$$-\frac{\partial}{\partial x_j}\left[\tilde{u}_i\left(\overline{\tau}_{ij} - \overline{\rho u_i'' u_j''}\right) + \overline{u_i''\left(\tau_{ij} - \frac{\rho u_i'' u_j''}{2}\right)}\right] + \frac{\partial \overline{q}_j}{\partial x_j} = 0 \tag{2.23}$$

One can observe that the *new* terms are:

$\overline{\rho u_i'' u_j''}$ called Reynolds stress terms;

$\overline{\rho u_j'' h}$ called Reynolds heat flux terms;

$\overline{u_i''\left(\tau_{ij} - \frac{\rho u_i'' u_j''}{2}\right)}$ called Reynolds dissipation terms.

It is evident at this point that these new terms would require some additional closure equations. It so happens, however, that as one tries to derive a new equation to calculate, say, the second order tensor $\overline{\rho u_i'' u_j''}$ , another *new* term is introduced, namely the third order tensor $\overline{\rho u_i'' u_j'' u_k''}$ . This constitutes the so called *turbulence closure problem*, i. e. , every time one tries to derive an equation for one of these new terms, at least another new tensor one order higher than the previous one is introduced.

An alternate approach, which we shall follow here, is the Boussinesq concept of *effective viscosity* [38, 39], whereby the turbulent mixing is modelled by upgrading the usual *molecular* viscosity coefficient by some quantity usually called the *eddy viscosity* coefficient. We will postpone the discussion of the particular turbulence model being used here until a later section. By now, it is sufficient to say that the turbulent mixing will be modelled by an eddy viscosity coefficient, such that the viscosity coefficient that appears on the definition of the viscous stress terms will be formed as [40]

$$\mu \leftarrow \mu_\ell + \mu_t \tag{2.24}$$

Here $\mu_\ell$ is the molecular viscosity coefficient and $\mu_t$ is the eddy viscosity coefficient. Similarly, the coefficient of thermal conductivity $\kappa$ can be obtained as

$$\kappa \leftarrow \kappa_\ell + \kappa_t = \frac{C_p \mu_\ell}{Pr} + \frac{C_p \mu_t}{Pr_t} \tag{2.25}$$

where $Pr$ is the Prandtl number and $Pr_t$ is the *turbulent* Prandtl number.

With the introduction of the model above mentioned into Equations 2.21–2.23 , they can now be expressed only in terms of the averaged quantities, i. e. , all the terms that involved perturbations (primed and double-primed terms) are in some sense *replaced* by the model. From now on, we shall drop all the *bars* and *tildas* in the variables, just to simplify the notation, but one should understand that we are talking about the averaged quantities. The equations can then be rewritten for the averaged variables as

continuity:

$$\frac{\partial \rho}{\partial t} + \frac{\partial}{\partial x_j}(\rho u_j) = 0 \tag{2.26}$$

momentum:

$$\frac{\partial}{\partial t}(\rho u_i) + \frac{\partial}{\partial x_j}(\rho u_i u_j + p\delta_{ij} - \tau_{ij}) = 0 \tag{2.27}$$

energy:

$$\frac{\partial e}{\partial t} + \frac{\partial}{\partial x_j}\left[(e+p)\,u_j - \tau_{ij}u_i + q_j\right] = 0 \tag{2.28}$$

where

$$\tau_{ij} = (\mu_\ell + \mu_t)\left(\frac{\partial u_i}{\partial x_j} + \frac{\partial u_j}{\partial x_i}\right) - \frac{2}{3}(\mu_\ell + \mu_t)\frac{\partial u_k}{\partial x_k}\delta_{ij} \tag{2.29}$$

$$q_j = -\left(\frac{\mu_\ell}{Pr} + \frac{\mu_t}{Pr_t}\right)\gamma\frac{\partial e_i}{\partial x_j} \tag{2.30}$$

pressure is still given by Equation 2.4 , and the specific internal energy can be obtained as

$$e_i = \frac{e}{\rho} - \frac{1}{2}u_j u_j \tag{2.31}$$

The above set of equations constitutes the so-called Reynolds-Averaged Navier-Stokes equations, and they are the aerodynamic equations that are actually being solved in this work. The equations are written above for a cartesian set of coordinates. As we will see shortly, this is not entirely desirable, and so we will turn our attention now to the problem of coordinate transformation.

## 2.2 Coordinate Transformation

Before proceeding with our discussion, it is useful to rewrite the flow governing equations in the matrix form they are usually seen in CFD applications. So, Equations 2.26–2.28 can be rewritten in strong conservation-law form, still in cartesian coordinates, as:

$$\frac{\partial Q}{\partial t} + \frac{\partial E}{\partial x} + \frac{\partial F}{\partial y} + \frac{\partial G}{\partial z} = 0 \tag{2.32}$$

where the vector of conserved quantities $Q$ is

$$Q = \begin{Bmatrix} \rho \\ \rho u \\ \rho v \\ \rho w \\ e \end{Bmatrix} \tag{2.33}$$

and the flux vectors $E$ , $F$ and $G$ are

$$E = \begin{Bmatrix} \rho u \\ \rho u^2 + p - \tau_{xx} \\ \rho uv - \tau_{xy} \\ \rho uw - \tau_{xz} \\ (e + p - \tau_{xx})\, u - \tau_{xy} v - \tau_{xz} w + q_x \end{Bmatrix} \tag{2.34}$$

$$F = \begin{Bmatrix} \rho v \\ \rho uv - \tau_{xy} \\ \rho v^2 + p - \tau_{yy} \\ \rho vw - \tau_{yz} \\ (e + p - \tau_{yy})\, v - \tau_{xy} u - \tau_{yz} w + q_y \end{Bmatrix} \tag{2.35}$$

$$G = \begin{Bmatrix} \rho w \\ \rho uw - \tau_{xz} \\ \rho vw - \tau_{yz} \\ \rho w^2 + p - \tau_{zz} \\ (e + p - \tau_{zz})\, w - \tau_{xz} u - \tau_{yz} v + q_z \end{Bmatrix} \tag{2.36}$$

It is convenient, for the purpose of actually implementing the flow solver code, to have the governing equations transformed to a general body-conforming curvilinear coordinate system. This will make the formulation in the code independent of the details of the actual topology being solved, besides making it very convenient for applying the boundary conditions and implementing turbulence models. The transformation is usually known only numerically, which does not pose any difficulty since what one really wants to know are the metrics of the transformation and its Jacobian. Following the usual procedure in the CFD literature (see, for instance, References[41]-[45]), one can convert the Navier-Stokes equations from cartesian coordinates to general curvilinear coordinates by means of the transformation :

$$\begin{aligned} \tau &= t \\ \xi &= \xi(x,y,z,t) \\ \eta &= \eta(x,y,z,t) \\ \zeta &= \zeta(x,y,z,t) \end{aligned} \tag{2.37}$$

Using chain rule expansions, the derivatives in terms of the cartesian variables can be expressed in terms of the curvilinear derivatives, in matrix form, as

$$\begin{Bmatrix} \frac{\partial}{\partial t} \\ \frac{\partial}{\partial x} \\ \frac{\partial}{\partial y} \\ \frac{\partial}{\partial z} \end{Bmatrix} = \begin{bmatrix} 1 & \xi_t & \eta_t & \zeta_t \\ 0 & \xi_x & \eta_x & \zeta_x \\ 0 & \xi_y & \eta_y & \zeta_y \\ 0 & \xi_z & \eta_z & \zeta_z \end{bmatrix} \begin{Bmatrix} \frac{\partial}{\partial \tau} \\ \frac{\partial}{\partial \xi} \\ \frac{\partial}{\partial \eta} \\ \frac{\partial}{\partial \zeta} \end{Bmatrix} \tag{2.38}$$

or conversely,

$$\begin{Bmatrix} \frac{\partial}{\partial \tau} \\ \frac{\partial}{\partial \xi} \\ \frac{\partial}{\partial \eta} \\ \frac{\partial}{\partial \zeta} \end{Bmatrix} = \begin{bmatrix} 1 & x_\tau & y_\tau & z_\tau \\ 0 & x_\xi & y_\xi & z_\xi \\ 0 & x_\eta & y_\eta & z_\eta \\ 0 & x_\zeta & y_\zeta & z_\zeta \end{bmatrix} \begin{Bmatrix} \frac{\partial}{\partial t} \\ \frac{\partial}{\partial x} \\ \frac{\partial}{\partial y} \\ \frac{\partial}{\partial z} \end{Bmatrix} \tag{2.39}$$

Due to the special form of the transformation matrices above, the Jacobian of the transformation, $J$ , can be simply written

$$J = |\partial(\xi,\eta,\zeta)/\partial(x,y,z)|$$

or in the form it is actually used in computation

$$J^{-1} = |\partial(x,y,z)/\partial(\xi,\eta,\zeta)| \tag{2.40}$$

Substituting the transformation expressions given by Eq. 2.38 into Eq. 2.32 , one can obtain:

$$\begin{aligned}\frac{\partial Q}{\partial \tau} + \xi_t \frac{\partial Q}{\partial \xi} + \eta_t \frac{\partial Q}{\partial \eta} + \zeta_t \frac{\partial Q}{\partial \zeta} + \xi_x \frac{\partial E}{\partial \xi} + \eta_x \frac{\partial E}{\partial \eta} + \zeta_x \frac{\partial E}{\partial \zeta} \\ + \xi_y \frac{\partial F}{\partial \xi} + \eta_y \frac{\partial F}{\partial \eta} + \zeta_y \frac{\partial F}{\partial \zeta} + \xi_z \frac{\partial G}{\partial \xi} + \eta_z \frac{\partial G}{\partial \eta} + \zeta_z \frac{\partial G}{\partial \zeta} &= 0\end{aligned} \tag{2.41}$$

Multiplying the above equation by $J^{-1}$ , and completing the t ms such that at least some of them can be written in divergence form, we have

$$\begin{aligned}&\frac{\partial}{\partial \tau}\left(J^{-1}Q\right) + \frac{\partial}{\partial \xi}\left[J^{-1}\left(\xi_t Q + \xi_x E + \xi_y F + \xi_z G\right)\right] \\ &+ \frac{\partial}{\partial \eta}\left[J^{-1}\left(\eta_t Q + \eta_x E + \eta_y F + \eta_z G\right)\right] + \frac{\partial}{\partial \zeta}\left[J^{-1}\left(\zeta_t Q + \zeta_x E + \zeta_y F + \zeta_z G\right)\right] \\ &- \left\{ Q\left[\frac{\partial}{\partial \tau}\left(J^{-1}\right) + \frac{\partial}{\partial \xi}\left(J^{-1}\xi_t\right) + \frac{\partial}{\partial \eta}\left(J^{-1}\eta_t\right) + \frac{\partial}{\partial \zeta}\left(J^{-1}\zeta_t\right)\right]\right. \\ &\quad + E\left[\frac{\partial}{\partial \xi}\left(J^{-1}\xi_x\right) + \frac{\partial}{\partial \eta}\left(J^{-1}\eta_x\right) + \frac{\partial}{\partial \zeta}\left(J^{-1}\zeta_x\right)\right] \\ &\quad + F\left[\frac{\partial}{\partial \xi}\left(J^{-1}\xi_y\right) + \frac{\partial}{\partial \eta}\left(J^{-1}\eta_y\right) + \frac{\partial}{\partial \zeta}\left(J^{-1}\zeta_y\right)\right] \\ &\quad \left. + G\left[\frac{\partial}{\partial \xi}\left(J^{-1}\xi_z\right) + \frac{\partial}{\partial \eta}\left(J^{-1}\eta_z\right) + \frac{\partial}{\partial \zeta}\left(J^{-1}\zeta_z\right)\right]\right\} = 0\end{aligned} \tag{2.42}$$

If we follow the work on Ref. [41] , and use Eqs. 2.38 and 2.39 , an expression for the Jacobian of the transformation can be found as

$$J = \left(x_\xi y_\eta z_\zeta + x_\eta y_\zeta z_\xi + x_\zeta y_\xi z_\eta - x_\xi y_\zeta z_\eta - x_\eta y_\xi z_\zeta - x_\zeta y_\eta z_\xi\right)^{-1} \tag{2.43}$$

Similarly, the following metric relations can be found

$$\begin{aligned}\xi_x &= J\left(y_\eta z_\zeta - y_\zeta z_\eta\right) & \xi_y &= J\left(x_\zeta z_\eta - x_\eta z_\zeta\right) \\ \xi_z &= J\left(x_\eta y_\zeta - x_\zeta y_\eta\right) & \eta_x &= J\left(y_\zeta z_\xi - y_\xi z_\zeta\right) \\ \eta_y &= J\left(x_\xi z_\zeta - x_\zeta z_\xi\right) & \eta_z &= J\left(x_\zeta y_\xi - x_\xi y_\zeta\right) \\ \zeta_x &= J\left(y_\xi z_\eta - y_\eta z_\xi\right) & \zeta_y &= J\left(x_\eta z_\xi - x_\xi z_\eta\right) \\ \zeta_z &= J\left(x_\xi y_\eta - x_\eta y_\xi\right)\end{aligned}$$

$$\begin{aligned} \xi_t &= -x_\tau \xi_x - y_\tau \xi_y - z_\tau \xi_z \\ \eta_t &= -x_\tau \eta_x - y_\tau \eta_y - z_\tau \eta_z \\ \zeta_t &= -x_\tau \zeta_x - y_\tau \zeta_y - z_\tau \zeta_z \end{aligned} \tag{2.44}$$

Working with the above metric relations and the Jacobian expression, one can prove that all the terms inside the curly brackets in Eq. 2.42 are identically zero. If we define, then,

$$\begin{aligned} \overline{Q} &\equiv J^{-1}Q = J^{-1} \begin{Bmatrix} \rho \\ \rho u \\ \rho v \\ \rho w \\ e \end{Bmatrix} \\ \overline{E} &\equiv J^{-1}(\xi_t Q + \xi_x E + \xi_y F + \xi_z G) \\ \overline{F} &\equiv J^{-1}(\eta_t Q + \eta_x E + \eta_y F + \eta_z G) \\ \overline{G} &\equiv J^{-1}(\zeta_t Q + \zeta_x E + \zeta_y F + \zeta_z G) \end{aligned} \tag{2.45}$$

the governing equations can be rewritten, still in strong conservation-law form, but for a general set of curvilinear coordinates, as:

$$\frac{\partial \overline{Q}}{\partial \tau} + \frac{\partial \overline{E}}{\partial \xi} + \frac{\partial \overline{F}}{\partial \eta} + \frac{\partial \overline{G}}{\partial \zeta} = 0 \tag{2.46}$$

This matrix equation, or its equivalent set of scalar equations, is essentially what is implemented for the flow governing equations on the code developed. The above still does not really explain the details of the numerical implementation of these equations, and a later section will be dedicated to address this issue.

## 2.3 Turbulence Model

As previously mentioned, the concept of an *effective* viscosity coefficient is used here in order to model the turbulent mixing by upgrading the *molecular* viscosity coefficient by the so called *eddy* viscosity coefficient. In the present work, the *eddy* viscosity coefficient, $\mu_t$ , is obtained from the two-layer Baldwin and Lomax [46]

algebraic model, which is implemented here in the usual way for wall-bounded shear layers[47,48] as

$$\mu_t = \begin{cases} (\mu_t)_{\text{inner}} & , \eta \leq \eta_{\text{crossover}} \\ (\mu_t)_{\text{outer}} & , \eta > \eta_{\text{crossover}} \end{cases} \tag{2.47}$$

Here $\eta$ is the *curvilinear distance* normal from the wall and $\eta_{\text{crossover}}$ is the smallest value of $\eta$ at which the inner and outer formulations give equal values.

The inner region uses the Prandtl-Van Driest formulation, such that

$$(\mu_t)_{\text{inner}} = \rho l^2 |\omega| \tag{2.48}$$

where $|\omega|$ is the magnitude of the local vorticity vector, and the length scale $l$ is obtained as

$$l = k\eta \left[1 - \exp\left(-\frac{\eta^+}{A^+}\right)\right]$$

and $\eta^+ = \left(\eta\sqrt{\rho_w \tau_w}\right)/\mu_w$ , $k = 0.4$ , $A^+ = 26$ .

The formulation for the outer region is similar to a Clauser formulation and is given by

$$(\mu_t)_{\text{outer}} = KC_{cp}F_{wake}F_{Kleb}(\eta) \tag{2.49}$$

where

$$F_{wake} = \text{the smaller of} \begin{pmatrix} \eta_{max}F_{max} \\ C_{wk}\eta_{max}U_{dif}^2/F_{max} \end{pmatrix}$$

The values of $\eta_{max}$ and $F_{max}$ are obtained from the function

$$F(\eta) = \eta|\omega| \left[1 - \exp\left(-\frac{\eta^+}{A^+}\right)\right]$$

where $F_{max}$ is the maximum value of $F(\eta)$ in the profile, and $\eta_{max}$ is the value of $\eta$ at which it occurs. The function $F_{Kleb}(\eta)$ , called the Klebanoff intermittency factor, is given by

$$F_{Kleb}(\eta) = \left[1 + 5.5\left(\frac{C_{Kleb}\eta}{\eta_{max}}\right)^6\right]^{-1}$$

Finally, $U_{dif}$ is the difference between maximum and minimum total velocity magnitudes in the profile (note that the minimum total velocity is zero for boundary layers), and the constants used have the following values : $K = 0.0168$ , $C_{cp} = 1.6$ , $C_{wk} = 0.25$ , and $C_{Kleb} = 0.3$ .

## 2.4 Numerical Implementation

It is always good practice to perform some form of nondimensionalization on the equations being used, even if it merely is to ensure more generality in the formulation. The choice of dimensionless parameters is somewhat arbitrary, so long as one does things consistently. In the present work, the density $\rho$ is scaled by the freestream density $\rho_\infty$ , the cartesian velocity components $u$, $v$ and $w$ are nondimensionalized with respect to the freestream speed of sound $a_\infty$ , and the total energy per unit of volume $e$ is referenced to $\rho_\infty a_\infty^2$ .

For simplicity of notation we will not use different symbols to denote the nondimensional variables, but we will continue to use the same nomenclature as before. The reader should keep in mind, however, that we will be refering to the nondimensionalized variables for the remainder of this development. Equation 2.46 can still be written as

$$\frac{\partial \overline{Q}}{\partial \tau} + \frac{\partial \overline{E}}{\partial \xi} + \frac{\partial \overline{F}}{\partial \eta} + \frac{\partial \overline{G}}{\partial \zeta} = 0$$

where the vector of conserved quantities $\overline{Q}$ is still written as previously defined. The reader should remember, though, that we are now referring to the nondimensional quantities, despite keeping the same nomenclature. It is instructive at this point, however, to rewrite the flux vectors with all their components in the general curvilinear coordinate system and to include the modifications caused by the nondimensionalization process. Thus, they can be written as

$$\overline{E} = J^{-1} \left\{ \begin{array}{c} \rho U \\ \rho u U + p\xi_x - \frac{M_\infty}{Re}\left(\tau_{xx}\xi_x + \tau_{xy}\xi_y + \tau_{xz}\xi_z\right) \\ \rho v U + p\xi_y - \frac{M_\infty}{Re}\left(\tau_{xy}\xi_x + \tau_{yy}\xi_y + \tau_{yz}\xi_z\right) \\ \rho w U + p\xi_z - \frac{M_\infty}{Re}\left(\tau_{xz}\xi_x + \tau_{yz}\xi_y + \tau_{zz}\xi_z\right) \\ (e+p)\,U - p\xi_t - \frac{M_\infty}{Re}\left(\beta_x\xi_x + \beta_y\xi_y + \beta_z\xi_z\right) \end{array} \right\} \qquad (2.50)$$

$$\overline{F} = J^{-1}\left\{\begin{array}{c} \rho V \\ \rho u V + p\eta_x - \frac{M_\infty}{Re}\left(\tau_{xx}\eta_x + \tau_{xy}\eta_y + \tau_{xz}\eta_z\right) \\ \rho v V + p\eta_y - \frac{M_\infty}{Re}\left(\tau_{xy}\eta_x + \tau_{yy}\eta_y + \tau_{yz}\eta_z\right) \\ \rho w V + p\eta_z - \frac{M_\infty}{Re}\left(\tau_{xz}\eta_x + \tau_{yz}\eta_y + \tau_{zz}\eta_z\right) \\ (e+p)V - p\eta_t - \frac{M_\infty}{Re}\left(\beta_x\eta_x + \beta_y\eta_y + \beta_z\eta_z\right) \end{array}\right\} \tag{2.51}$$

$$\overline{G} = J^{-1}\left\{\begin{array}{c} \rho W \\ \rho u W + p\zeta_x - \frac{M_\infty}{Re}\left(\tau_{xx}\zeta_x + \tau_{xy}\zeta_y + \tau_{xz}\zeta_z\right) \\ \rho v W + p\zeta_y - \frac{M_\infty}{Re}\left(\tau_{xy}\zeta_x + \tau_{yy}\zeta_y + \tau_{yz}\zeta_z\right) \\ \rho w W + p\zeta_z - \frac{M_\infty}{Re}\left(\tau_{xz}\zeta_x + \tau_{yz}\zeta_y + \tau_{zz}\zeta_z\right) \\ (e+p)W - p\zeta_t - \frac{M_\infty}{Re}\left(\beta_x\zeta_x + \beta_y\zeta_y + \beta_z\zeta_z\right) \end{array}\right\} \tag{2.52}$$

In the above equations, $M_\infty$ is the freestream Mach number defined as

$$M_\infty = \frac{\mathcal{U}_\infty}{a_\infty} \tag{2.53}$$

where $\mathcal{U}_\infty = \sqrt{u^2 + v^2 + w^2}$ is the magnitude of the freestream velocity vector. $Re$ is the Reynolds number, given in the usual way by

$$Re = \frac{\rho_\infty \mathcal{U}_\infty \ell_0}{\mu_\infty} \tag{2.54}$$

where $\mu_\infty$ is the freestream (laminar) viscosity coefficient and $\ell_0$ is the reference length. It should also be mentioned that any viscosity coefficient that appears on the formulation is nondimensionalized with respect to $\mu_\infty$. The contravariant velocity components, $U$, $V$ and $W$, are defined as

$$\begin{aligned} U &= \xi_t + \xi_x u + \xi_y v + \xi_z w \\ V &= \eta_t + \eta_x u + \eta_y v + \eta_z w \\ W &= \zeta_t + \zeta_x u + \zeta_y v + \zeta_z w \end{aligned} \tag{2.55}$$

The $\beta_x$, $\beta_y$ and $\beta_z$ terms are given by

$$\begin{aligned} \beta_x &= \tau_{xx}u + \tau_{xy}v + \tau_{xz}w - q_x \\ \beta_y &= \tau_{xy}u + \tau_{yy}v + \tau_{yz}w - q_y \\ \beta_z &= \tau_{xz}u + \tau_{yz}v + \tau_{zz}w - q_z \end{aligned} \tag{2.56}$$

All the other variables that appear in the above equations have been previously defined, and again we call the reader's attention for the fact the *dimensional* variables should be just replaced by their nondimensional counterparts in those definitions. It is interesting to note that the three dimensionless numbers usually encountered when nondimensionalizing the Navier-Stokes equations, namely Mach number, Reynolds number and Prandtl number also appear. Although not explicitly shown in the equations immediately above, the Prandtl number arises in our case through the way in which we have defined the components of the heat flux vector, $q_x$, $q_y$ and $q_z$ .

The Beam and Warming implicit approximate factorization scheme[49, 50] is used for the solution of the finite difference equations. The spatial derivatives in Equation 2.46 are approximated using three-point, second-order central differencing, and the implicit Euler method is used for the time march. With this method, we can write

$$\overline{Q}^{n+1} = \overline{Q}^{n} + \Delta t \left( \frac{\partial \overline{Q}}{\partial \tau} \right)^{n+1} + \mathcal{O}\left(\Delta t^2\right) \tag{2.57}$$

where by $\mathcal{O}(\Delta t^2)$ we mean that this is a first order method in time, and the superscript $n$ indicates at which instant of time the quantity should be evaluated. If Equation 2.46 is substituted in the above, we obtain

$$\overline{Q}^{n+1} = \overline{Q}^{n} - \Delta t \left( \frac{\partial \overline{E}}{\partial \xi} + \frac{\partial \overline{F}}{\partial \eta} + \frac{\partial \overline{G}}{\partial \zeta} \right)^{n+1} + \mathcal{O}\left(\Delta t^2\right) \tag{2.58}$$

Since the flux vectors are nonlinear functions of the vector of conserved quantities, in order to solve for $\overline{Q}^{n+1}$ , while maintaining the order of accuracy of the method, the nonlinearity is removed by a local Taylor series expansion about $\overline{Q}^{n}$ . This process yields

$$\begin{aligned} \overline{E}^{n+1} &= \overline{E}^{n} + A^{n}\left(\overline{Q}^{n+1} - \overline{Q}^{n}\right) + \mathcal{O}\left(\Delta t^2\right) \\ \overline{F}^{n+1} &= \overline{F}^{n} + B^{n}\left(\overline{Q}^{n+1} - \overline{Q}^{n}\right) + \mathcal{O}\left(\Delta t^2\right) \\ \overline{G}^{n+1} &= \overline{G}^{n} + C^{n}\left(\overline{Q}^{n+1} - \overline{Q}^{n}\right) + \mathcal{O}\left(\Delta t^2\right) \end{aligned} \tag{2.59}$$

where $A$, $B$ and $C$ are the Jacobian matrices given by

$$A = \frac{\partial \overline{E}}{\partial \overline{Q}}$$

$$B = \frac{\partial \overline{F}}{\partial \overline{Q}}$$

$$C = \frac{\partial \overline{G}}{\partial \overline{Q}}$$

Substituting the linearized expressions into Eq. 2.58 one obtains

$$\begin{aligned}\left[I + \Delta t\left(\frac{\partial}{\partial \xi}A^n + \frac{\partial}{\partial \eta}B^n + \frac{\partial}{\partial \zeta}C^n\right)\right]\overline{Q}^{n+1} \;=\; & \\ \left[I + \Delta t\left(\frac{\partial}{\partial \xi}A^n + \frac{\partial}{\partial \eta}B^n + \frac{\partial}{\partial \zeta}C^n\right)\right]\overline{Q}^n & \\ -\Delta t\left(\frac{\partial \overline{E}}{\partial \xi} + \frac{\partial \overline{F}}{\partial \eta} + \frac{\partial \overline{G}}{\partial \zeta}\right)^n + \mathcal{O}\left(\Delta t^2\right) & \end{aligned} \tag{2.60}$$

where $I$ is the identity matrix.

In order to make the solution algorithm more cost effective, an approximate factorization of the three-dimensional operator into three one-dimensional operators is introduced. Following the work of Beam and Warming [49], and Pulliam [41], a term of the form

$$\left[\Delta t^3\left(\frac{\partial B^n}{\partial \eta}\frac{\partial A^n}{\partial \xi} + \frac{\partial C^n}{\partial \zeta}\frac{\partial A^n}{\partial \xi} + \frac{\partial B^n}{\partial \eta}\frac{\partial C^n}{\partial \zeta}\right) + \Delta t^4\frac{\partial B^n}{\partial \eta}\frac{\partial C^n}{\partial \zeta}\frac{\partial A^n}{\partial \xi}\right]\left(\frac{\overline{Q}^{n+1} - \overline{Q}^n}{\Delta t}\right)$$

can be added to the left-hand side of unfactored equation. Furthermore, one should note that the added term is of order $\Delta t^3$ and therefore does not alter the order of accuracy of the method. With the above term, the equation can be factored such that the algorithm can be written in the so-called *delta form* as

$$\begin{aligned}\left(I + \Delta t\frac{\partial}{\partial \eta}B^n\right)\left(I + \Delta t\frac{\partial}{\partial \zeta}C^n\right)\left(I + \Delta t\frac{\partial}{\partial \xi}A^n\right)\Delta_t\overline{Q}^n \;=\; & \\ -\Delta t\left(\frac{\partial \overline{E}}{\partial \xi} + \frac{\partial \overline{F}}{\partial \eta} + \frac{\partial \overline{G}}{\partial \zeta}\right)^n + \mathcal{O}\left(\Delta t^2\right) & \end{aligned} \tag{2.61}$$

where $\Delta_t$ is a forward difference operator in time, such that

$$\Delta_t\overline{Q}^n = \overline{Q}^{n+1} - \overline{Q}^n$$

With the introduction the three-point second order central differencing to approximate the space derivatives, the final form of the algorithm can be written

as

$$L_\eta L_\zeta L_\xi \Delta_t \overline{Q}^n = R_\xi + R_\eta + R_\zeta \tag{2.62}$$

where the above operators are defined as

$$\begin{aligned}
L_\xi &= \left(I + \Delta t \delta_\xi \hat{A}^n - \epsilon_I \Delta t J^{-1} \nabla_\xi \Delta_\xi J - \Delta t M_\infty \mathrm{Re}^{-1} \overline{\delta_\xi} J^{-1} \hat{M}_\xi^n J\right) \\
L_\eta &= \left(I + \Delta t \delta_\eta \hat{B}^n - \epsilon_I \Delta t J^{-1} \nabla_\eta \Delta_\eta J - \Delta t M_\infty \mathrm{Re}^{-1} \overline{\delta_\eta} J^{-1} \hat{M}_\eta^n J\right) \\
L_\zeta &= \left(I + \Delta t \delta_\zeta \hat{C}^n - \epsilon_I \Delta t J^{-1} \nabla_\zeta \Delta_\zeta J - \Delta t M_\infty \mathrm{Re}^{-1} \overline{\delta_\zeta} J^{-1} \hat{M}_\zeta^n J\right) \\
R_\xi &= -\Delta t \delta_\xi \overline{E}^n - \epsilon_E \Delta t J^{-1} \left(\nabla_\xi \Delta_\xi\right)^2 J \overline{Q}^n \\
R_\eta &= -\Delta t \delta_\eta \overline{F}^n - \epsilon_E \Delta t J^{-1} \left(\nabla_\eta \Delta_\eta\right)^2 J \overline{Q}^n \\
R_\zeta &= -\Delta t \delta_\zeta \overline{G}^n - \epsilon_E \Delta t J^{-1} \left(\nabla_\zeta \Delta_\zeta\right)^2 J \overline{Q}^n
\end{aligned} \tag{2.63}$$

Here $\delta_\xi$ , $\delta_\eta$ and $\delta_\zeta$ are central difference operators; $\nabla_\xi$ , $\nabla_\eta$ and $\nabla_\zeta$ are backward difference operators; and $\Delta_\xi$ , $\Delta_\eta$ and $\Delta_\zeta$ are forward difference operators in the $\xi$- , $\eta$- , and $\zeta$-directions, respectively. For example,

$$\begin{aligned}
\delta_\xi \overline{Q}^n_{i,j,k} &= \frac{1}{2}\left[\overline{Q}^n_{i+1,j,k} - \overline{Q}^n_{i-1,j,k}\right] \\
\nabla_\xi \overline{Q}^n_{i,j,k} &= \overline{Q}^n_{i,j,k} - \overline{Q}^n_{i-1,j,k} \\
\Delta_\xi \overline{Q}^n_{i,j,k} &= \overline{Q}^n_{i+1,j,k} - \overline{Q}^n_{i,j,k}
\end{aligned}$$

The $\overline{\delta_\xi}$, $\overline{\delta_\eta}$ and $\overline{\delta_\zeta}$ are midpoint operators used to maintain a compact three point second order accurate central difference scheme when differencing the viscous terms in the left-hand side. As previously described, the $\Delta_t$ is a forward difference operator in time.

The Jacobian matrices were split such that $\hat{A}$, $\hat{B}$ and $\hat{C}$ contain, respectively, the inviscid terms of $A$, $B$ and $C$, whereas $\hat{M}_\xi$, $\hat{M}_\eta$ and $\hat{M}_\zeta$ contain the viscous terms. Expressions for these matrices are given in Appendix A. A few extra words may be important to clarify the need for midpoint operators when working on the viscous terms. The left-hand side matrices, as defined in Equations 2.63, are block tridiagonal matrices where each block is $5 \times 5$. However, the viscous terms themselves, i. e. , the components of the $\hat{M}$ matrices, already involve derivatives of the velocity components in the case of the viscous stress terms and of the internal energy in the case of the heat flux terms. Therefore, if we insist in using central

differences, we need to use midpoint operators in order to avoid a five point stencil, which would cause the operators to become full-block pentadiagonal. With the midpoint operators we can keep the matrices block tridiagonal while retaining the order of accuracy of the method.

Although linear stability analysis shows that the fully implicit algorithm is unconditionally stable, stability bounds are encountered in practice. The problem comes about because of the nonlinear interactions in the convection terms of the momentum equations. The problem can be understood easily if one thinks in terms of waves interacting. When two waves interact, one of the products is a new wave of higher frequency, which frequency is the sum of the original ones. This frequency *cascading* will, at some point, exceed the resolution capacity of a finite mesh, with the result that these frequencies either alias back into the lower frequency range or pile up at the high frequency side. If not controlled, this process may cause serious inaccuracies and quite possibly numerical instability. The usual way the problem is handled is to introduce some form of numerical dissipation into the algorithm, with an error level that should not interfere with the accuracy of any viscous effects being captured in the solution. Some numerical schemes, generically known as *upwind* schemes, intrinsically have this numerical dissipation built into the scheme by the way they use one sided differences. Central difference schemes, however, do not have this numerical dissipation built into the scheme, and so it must be explicitly added in order to control the nonlinear instabilities above described.

The procedure adopted here consists of introducing a constant-coefficient, fourth-order artificial dissipation in the right-hand side operators, and constant-coefficient, second-order artificial dissipation in the left-hand side operators. In the right-hand side, or *explicit* side, the amount of artificial disspation introduced is controlled by the coefficient $\epsilon_E$ , and on the left-hand side, or *implicit* side, it is controlled by the coefficient $\epsilon_I$ (see Equations 2.63). Ideally, one would like to use fourth-order artificial dissipation on both implicit and explicit sides, because the use of different orders of numerical dissipation schemes does introduce a small numerical error on the solution. However, once again the issue of solution efficiency dictates that we settle for the second-order numerical dissipation on the left-hand side, because a

fourth-order scheme would cause a five point stencil and so block pentadiagonal matrices.

One possible way to deal with the problem of having different orders of artificial dissipation schemes on the implicit and explicit sides is to use the so-called *diagonal algorithm*, described by Pulliam and Chaussee[43] . The idea of the diagonal algorithm is based on the diagonalization of the inviscid left-hand side matrices as described by Warming, Beam and Hyett[51] . These authors show that the Jacobian matrices $\hat{A}$, $\hat{B}$ and $\hat{C}$ have real eigenvalues and a complete set of eigenvectors, and so can be diagonalized. It is clear that for viscous calculations the algorithm cannot be rigorously applied, since in order to diagonalize the left-hand side operators we need to neglect the implicit viscous terms. However, results by Pulliam and Steger[52] show that for steady viscous flows and in convection dominated unsteady flows the diagonal algorithm, as described above, produces very good results. Furthermore, it allows the use of the fourth-order artificial dissipation scheme in the left-hand side operators because, despite the fact that this makes the matrices block pentadiagonal, now each block is a five by five diagonal matrix, making the *inversion* process fairly inexpensive even for a block pentadiagonal system. In the present work some attempt was made to program the diagonal algorithm, however there were questions concerning the accuracy of the algorithm in the case of self-excited unsteady calculations *, which is exactly what our aeroelastic analyses are. Hence the idea was abandoned.

Although not explicitly mentioned in the previous equations, freestream subtraction[53] is performed in the flux vectors when computing the right-hand side terms in Equation 2.62 . The reason for this comes is that, when arbitrary curvilinear coordinates and general finite differences are used, there are small numerical errors introduced in the calculation of the metrics of the transformation which may cause the code to be unable to reproduce the freestream (or an uniform flow). By performing the freestream subtraction in the flux vectors, we ensure the capability of recovering freestream and reduce the overall error of the method.

Since a viscous formulation is used here, at body walls we have no-slip boundary conditions, i. e. , $u = v = w = 0$ for steady problems, or $u = x_\tau$ , $v = y_\tau$

* Pulliam, T.H., personal communication, May 1986.

and $w = z_\tau$ for unsteady cases. Here $x_\tau$, $y_\tau$ and $z_\tau$ are the cartesian components of the grid velocity due to body motion. We assume also adiabatic walls and zero normal pressure gradient at body walls. Uniform freestream is enforced at the upstream and far-field lateral boundaries. The treatment given to the downstream boundary depends on the value of the freestream Mach number. For a supersonic freestream, the downstream boundary is extrapolated from interior values. For a subsonic freestream, according to characteristic relations, there are four characteristics propagating downstream and one propagating upstream. To be consistent with that, pressure is then fixed at the downstream boundary (at its freestream value) and the other quantities are extrapolated from interior values. From a strictly numerical point of view, it should be mentioned that all the boundary conditions are treated explicitly in the present work. This means that they are applied using the information available at the present time step.

There are some important points concerning the boundary conditions that should be further discussed. In an attempt to save computational points in the grid, the approach primarily used in the present work does not consider a body base, but rather stops the computation at some point along the cylindrical afterbody section. This may cause some concern when computing subsonic flows, since we will be assuming freestream pressure at this computational exit plane whereas the flow will probably not be completely back to a freestream condition due to the presence of the body. Essentially, there is an error being introduced, but care is being exercised in order to make the afterbody cylindrical section long enough that whatever errors are introduced at the downstream boundary will not propagate upstream to the point of influencing the region of interest in the solution. Later, some results will be presented that illustrate this point and confirm our statement that the regions of interest are not being contaminated by whatever errors are introduced at the downstream boundary.

Another point of concern is the treatment of the far-field lateral boundaries. Since we have a body at angle of attack, lift will be generated and so there is a question about the conservation of circulation in the far-field. To be precise, far-field

lateral boundary conditions should have some way of enforcing this conservation-of-circulation boundary condition. However, since we are dealing with three dimensional bodies of revolution in the present work, we do not feel that the added accuracy is worth the complication of the boundary conditions. Moreover, the results obtained seem to corroborate our assumptions, indicating that assuming freestream conditions in the upstream and far-field lateral boundaries is good enough for the present case.

Finally, the reasoning behind the zero normal pressure gradient condition at the wall should be addressed. The code is implemented with the assumption that $\eta$ is the normal direction, and so this boundary condition is enforced by setting $\partial p/\partial \eta$ to zero at the wall. Strictly speaking, for a viscous formulation there is no theoretical reasoning that would lead to the zero normal pressure gradient condition without the introduction of any simplifying assumption. In particular, for viscous flows over curved walls this condition is not completely correct. However, if we study results from boundary layer theory [54] and evidence from experimental measurements on boundary layers, we observe that the pressure is approximately constant throughout the thickness of the boundary layer. In our case, we can also argue that this *boundary layer* assumption is being used only on the points that are nearest to the wall. In other words, although there is a physical boundary layer, the zero normal pressure condition is only being used up to the first grid surface off the body and not throughout the whole layer. It should be pointed out that there are cases where this condition can be rigorously demonstrated. For the general case in a Navier-Stokes formulation, however, the justification for its use is based on experimental, as well as numerical, evidence in conjunction with the insight provided by boundary layer theory.

For each time step Equation 2.62 is solved by forming the right-hand side and then *inverting* separately, and in the sequence indicated, each of the left-hand side operators through the use of an L-U decomposition algorithm for block tridiagonal matrices. In the cases when an "O" type mesh is used in the circumferential direction, i. e. , the grid is completely wrapped around the body for the full 360°, the grid is said to be *periodic* in the circumferential direction. For periodic grids, it is

necessary to program periodic tridiagonal solvers, because in this case the left-hand side matrix is not strictly tridiagonal but has extra blocks in the upper right and the lower left corners. Appendix B has more details about the handling of periodic tridiagonal matrices.

The database is structured in a pencil format which minimizes the amount of data that has to be stored in main memory at a given time. The pencil data structure concept, as well as the procedure for solving Equation 2.62 when the database has such a format, are described in detail by Deiwert and Rothmund[55] A pictorial idea of a general body configuration in physical space, together with how this is mapped into computational space and showing the various blocks boundaries, is presented in Figure 2.1 . Pencils of data are formed by storing sequentially the blocks in the given sweep direction while keeping the pencil base restricted to one block dimension in the other coordinates. Incidentally, this is a good point to mention that the code primarily used (as the flow solver) in this work evolved from a steady state version of the ARC3D code that the authors of Reference[55] had optimized to run on a CDC Cyber 205 computer. The code is highly vectorized and makes extensive use of random, or asynchronous, I/O in order to improve its efficiency for a problem that is definitely not core contained.

The computational mesh for all the cases considered in this work was generated using algebraic methods, since for the regular geometries typical of launch vehicle configurations these methods are able to provide sufficiently good grids and they are very simple to use. It is important to realize that, since the goal is to perform aeroelastic analyses, the body will be deforming as the solution proceeds. This means that some form of grid reshaping is necessary in order to account for this deformation. In the present approach, the complete grid is regenerated at every time step (when performing aeroelastic calculations), which is another reason why it is important to use algebraic grid generation methods which are very fast. If one decides to analyze more complex geometries, say a vehicle with strap-on boosters, probably a more elaborated grid generation scheme should be adopted.

Both exponential and hyperbolic-tangent[56] grid stretching techniques are used where necessary to cluster grid points in the regions of higher flow gradients. One

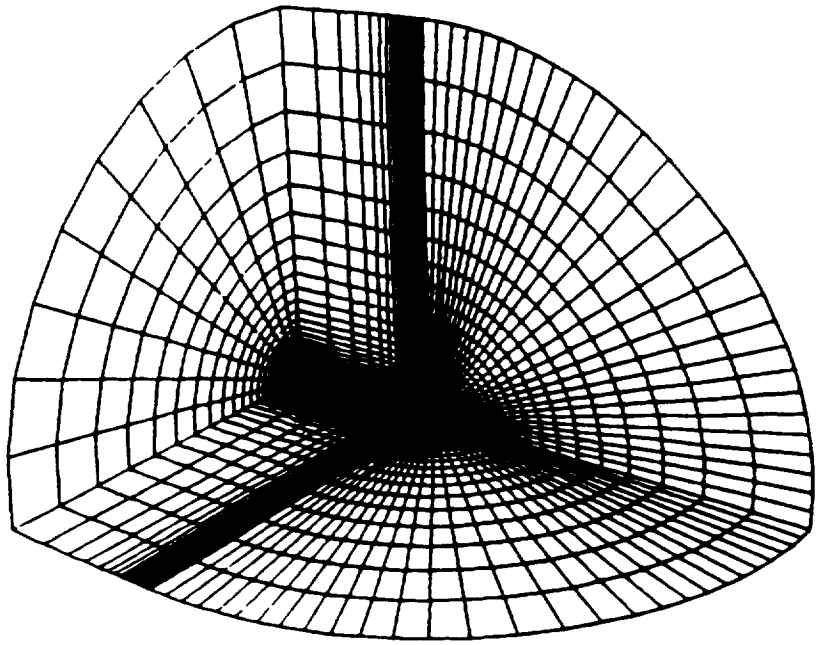

(*a*) Physical space.

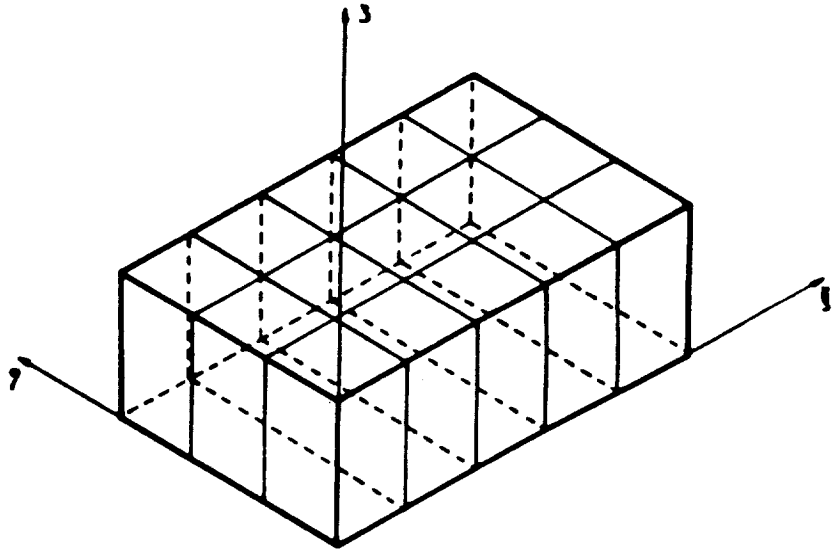


(*b*) Computational space.

Figure 2.1: General body configuration illustrating the pencil (and block) data structure format.

obvious instance where such clustering must occur is close to the body in the normal direction, since we need a very refined grid in order to capture the viscous effects. Other situations where clustering is necessary may include regions where shocks are expected to occur, or regions of rapid expansion, for instance, where the body may have the sharp corners[57] typical of boattails and flares. A final note with regard to grid clustering is that, despite the fact the viscous terms are kept in all three coordinate directions in the present formulation, the approach used here should still be considered within the scope of the thin layer approximation to the Reynolds-Averaged Navier-Stokes equations[58]. This is because the grids used are too coarse in the longitudinal and circumferential directions to capture completely the viscous effects in these directions.

# Chapter 3

# Aeroelastic Formulation

## 3.1 Equations of Motion

The structural-dynamic equations for the vehicle are developed by considering free-free flexural vibration of an elongated beam with variable properties. They are cast in modal form. It is assumed that the angle of attack remains low enough that no lateral forces will appear, and so bending in only one plane has to be considered. The formulation developed is quite general, even allowing for rigid body degrees of freedom, although in the applications presented here the rigid body degrees of freedom were assumed to be constrained.

The equations of motion for a general beam in planar vibration can be found in the extensive literature (see, for instance, References [59]-[62] . In terms of *engineering* beam theory several degrees of approximation exist from which a selection must be made. For the approach adopted here, it is not particularly important to go over all the exact details of the derivation of these equations, since we will simply assume that mode shapes and natural frequencies of free vibration are available to us. The modes could have been obtained either from structural-dynamic tests or from some dynamic finite element structural analysis of the vehicle. Moreover, we will not discuss the issue of how structural damping is introduced into the formulation but simply take it as a given quantity, obtained either from experiment or some theoretical model. Finally, it should be clear that, although the overall

aeroelastic formulation is nonlinear (as we hope to demonstrate throughout this development) , the strictly structural-dynamic formulation is linear and the principle of superposition can be applied.

For the sake of completeness, and to clarify the dimensions of the quantities involved here, the equation of motion for a beam in flexural vibration is presented. When the effects of shear and rotary inertia are neglected,

$$m(x)\frac{\partial^2 \delta}{\partial t^2} + \frac{\partial^2}{\partial x^2}\left[EI(x)\frac{\partial^2 \delta}{\partial x^2}\right] = F_z(x,t)$$

where $\delta(x,t)$ is the total lateral deflection of the centerline of the beam, $m(x)$ is the mass per unit of length, $EI(x)$ is the bending stiffness, and $F_z(x,t)$ is the lateral external load applied to the beam (units of force per unit of length). Again, it is very important to stress that the equation above is merely an example of what a very simplified equation of motion for lateral vibration of an elongated beam might look like. As mentioned by Bisplinghoff and Ashley[60], "shear, rotary inertia, and several other effects are automatically accounted for" when a modal superposition solution technique is used.

The total deflection $\delta(x,t)$ at any station along the body can be expressed[59], using a modal approach, as

$$\delta(x,t) = \sum_{i=1}^{\infty} q_i(t)\,\phi_i(x) \tag{3.1}$$

where $q_i(t)$ are the generalized normal coordinates and $\phi_i(x)$ are the normal modes. To be consistent with the aerodynamic formulation, we will assume that $\delta(x,t)$ and $q_i(t)$ have been nondimensionalized with respect to the same reference length $\ell_0$ used for the aerodynamic equations. It should be mentioned that the use of a modal approach assumes that the structure and the frequencies of interest are such that disturbances are felt almost instantaneously throughout the structure. In other words, problems with travelling structural waves, which are common in very large space structures, are of no concern for the vehicles considered here. It is also clear that in actual application only a finite number of modes is considered. In other

words Eq. 3.1 should be more properly written as

$$\delta(x,t) = \sum_{i=1}^{N} q_i(t)\phi_i(x)$$

where $N$ represents the number of modes employed in the analysis.

Since the normal coordinates are not coupled either elastically or inertially, the equation of motion for the i-th cooordinate can be written as

$$\overline{m}_i \left[\ddot{q}_i(t) + 2\zeta_i\overline{\omega}_i\dot{q}_i(t) + \overline{\omega}_i^2 q_i(t)\right] = P_i(t) \tag{3.2}$$

Here the quantities have already been nondimensionalized, and the dots indicate derivatives with respect to (nondimensional) time. The nondimensional natural frequencies, $\overline{\omega}_i$, are defined by

$$\overline{\omega}_i = \frac{\ell_0\omega_i}{a_\infty} \tag{3.3}$$

where $\omega_i$ is the natural free-free bending frequency in the i-th mode, $\ell_0$ is the reference length used for nondimensionalization of the aerodynamic equations, and $a_\infty$ is the freestream speed of sound. It is interesting to point out that the nondimensional frequency above is not the same as the so-called *reduced frequency*[59,60,63], which is a parameter usually seen in aeroelastic or unsteady aerodynamic applications. However, since that reduced frequency, $k$, is usually defined as

$$k = \frac{\omega\ell_0}{U_\infty}$$

they are related by

$$\overline{\omega}_i = M_\infty k_i$$

The nondimensional generalized masses, $\overline{m}_i$, can be obtained from the actual vehicle mass distribution, $m(x)$, from

$$\overline{m}_i = \int_0^{\ell_b} \frac{m(x)}{\rho_\infty \ell_0^2}\phi_i(x)\phi_i(x)dx \tag{3.4}$$

where $\rho_\infty$ is the freestream density and $\ell_b$ is the (nondimensional) body length. If the (dimensional) generalized masses $\tilde{m}_i$ are already known, say, from experimental

results, it is clear that the integration described above is not necessary, and the nondimensionalization is simply obtained by

$$\overline{m}_i = \frac{\tilde{m}_i}{\rho_\infty \ell_0^3} \tag{3.5}$$

It is important to emphasize that in the present approach the natural frequencies, the structural damping coefficients ($\zeta_i$), the normal modes and the mass distribution are considered input data. They are assumed to be known either from tests or any other theoretical analysis.

The real difference in the present approach, when compared to classical aeroelastic analysis, is associated with the generalized aerodynamic forces, $P_i(t)$, which in this case are calculated from

$$P_i(t) = \int_0^{\ell_b} \ell(x,t)\phi_i(x)dx \tag{3.6}$$

Here $\ell(x,t)$ is the nondimensional running normal force acting on the vehicle, obtained from suitable circumferential integrations of the body pressure distribution. Note that the *dimensional* counterpart to $\ell(x,t)$ would have units of force per unit of length, and also that since we are dealing with small angle of attack cases $\ell(x,t)$ is numerically very close to the running lift on the body. The important point is that the true nonlinear character of the present analysis is somewhat *hidden* in the generalized aerodynamic forces, because the pressure distribution around the body is obtained from the numerical solution of the Navier-Stokes equations. Note that $P_i(t)$ is identified with mode $i$, but has contributions of all modes through $\ell(x,t)$ . In this fashion all transonic aerodynamic nonlinearities are captured by the method, whereas the structural-dynamic formulation is still kept very simple.

Some points regarding the assumption that the angle of attack remains small should be further clarified. First, and probably the most important reason why this assumption is introduced, is the fact that the kind of boosters we are most interested in here are prevented from attaining large angles of attack because the loads on the structure would be tremendous. Most such vehicles have some maximum angle of attack that, if exceeded, cause the launch to be aborted by the destruction of the vehicle. For the Saturn V , this maximum tolerable angle of attack was

approximately 4 degrees*. Second, there is nothing to indicate that the kind of instability we are concerned with is a high-angle-of-attack phenomenon. Quite to the contrary, since the major mechanism that drives the instability is associated with lags in the aerodynamic forces due to the shock motion[64], its effect would be more pronounced at very small angles of attack where the streamwise location of the shock can actually be forward in the leeward side (when compared to the windward side) for a portion of the motion and backward for the rest of it. Another important observation is that there is no conceptual difficulty in extending the present method to treat cases where asymmetric separation, or yaw angle exists, such that bending in both planes and twisting of the vehicle are to be considered. It is just a matter of coding the necessary geometric considerations and introducing the structural modes associated with the added degrees of freedom. As far as the aerodynamic formulation is concerned, it is valid for any angle of attack; its more stringent limitation is associated with the turbulence model which originally was derived for attached or mildly separated flows.

## 3.2 Solution of Aeroelastic Equations

Since the calculation of the flow solution at each time step, and so the evaluation of $P_i(t)$ , is much more time consuming then the solution of the structural-dynamic equations, some constraints are imposed on the numerical method that can be used for the time integration of Equation 3.2. The idea of transforming the second order equation into a first order system as usually done in control theory may seem attractive, but it is not very practical in this case. For instance, any implicit method or any predictor-corrector sequence, which would typically involve the evaluation of the forcing term at an instant of time ahead of the current time, would become prohibitive as far as computational time is concerned with present computers. On the other hand, the explicit Euler method can be shown to be always unstable in such situations by a simple linear stability analysis.

The procedure selected to advance Equation 3.2 in time consists of a straight finite differencing of both the first and second time derivatives, as also done by

* Ashley, H., personal communication, July 1987.

Steger and Bailey [31], Guruswamy and Yang[65], and Borland and Rizzetta[66]. Using second order accurate formulas, we can approximate those derivatives as

$$\ddot{q}_i \cong \frac{q_{i,n+1} - 2q_{i,n} + q_{i,n-1}}{(\Delta t)^2}$$

$$\dot{q}_i \cong \frac{q_{i,n+1} - q_{i,n-1}}{2\Delta t}$$

Here the subscript $i$ refers to the mode considered and the subscript $n$ refers to the time level at which the quantity is evaluated. With the above formulas, the expression for $q_{i,n+1}$ , i. e. , the generalized deflection of mode $i$ at time $n+1$ , is given by

$$q_{i,n+1} = \frac{\left[2 - (\Delta t)^2 \varpi_i^2\right] q_{i,n} - (1 - \Delta t \zeta_i \varpi_i)\, q_{i,n-1} + (\Delta t)^2 \tilde{P}_{i,n}}{(1 + \Delta t \zeta_i \varpi_i)} \qquad (3.7)$$

where, for simplicity of notation, we have denoted $\tilde{P}_i(t) = P_i(t)/\overline{m}_i$.

Linear stability analysis of the above scheme shows that it is conditionally stable. However, this really poses no constraint in the time step size for aeroelastic analysis, because the values of $\Delta t$ required for the stability, and more importantly the time-accuracy, of the aerodynamic equations alone is much smaller than whatever restrictions could be imposed by the conditional stability of the above scheme (for values of natural frequency that would be of any concern for aeroelastic stability). More on the stability properties of this Equation 3.7 scheme will be discussed in the next section. The analysis also shows that for $\zeta_i \to 0$ the scheme is numerically non-dissipative, which is of course the expected result since central differences are being used. This is important to avoid *hiding* physically unstable solutions because of numerical dissipation introduced by the method.

The coupling of the two sets of equations, the Navier-Stokes equations governing the flow behavior and the above described structural-dynamic equations governing the oscillating vehicle behavior, is performed in the following way. At each time step, the aerodynamic equations are solved in a time-accurate fashion, and their solution provides the forcing terms for the aeroelastic analysis. These are weighted integrals of the pressure distribution along the body surface, as one can see from Equation 3.6 . Solution of the structural-dynamic equations gives the new deformed

shape of the body, as well as the body oscillating velocities, and therefore the boundary conditions for the aerodynamic solution at the next time step. By tracing the growth or decay of a perturbed oscillation, the aeroelastic stability of a given configuration can be ascertained.

Note that once the response in terms of the generalized coordinates, $q_i$'s, is calculated, the total deflection of the body centerline, $\delta(x,t)$, can be determined. Since we are assuming that body cross-sections do not deform, this means that the total deflection of the body surface is known, and the grid can be regenerated. The solution process, as implemented here, recalculates the whole computational mesh at every time step to account for the deformation and motion of the body. This was done to provide greater generality to the method and enable it to treat not so small deflections.

Finally, it should be stressed that, in the present implementation of the method, the rigid body degrees of freedom were assumed to be somehow constrained, and only the elastic ones were considered. There is no additional conceptual difficulty in including the rigid body modes in the current code. However, results by Woods and Ericsson [4] seem to indicate that the inclusion of these modes is not critical for determining the aeroelastic stability of a given vehicle, for the kinds of configurations and phenomena dealt with in the present work.

## 3.3 Stability Considerations

In this section we intend to discuss further the numerical stability of the scheme implemented for the solution of the aeroelastic equations. The main objective here is to substantiate the claims made in the previous section regarding the stability and accuracy of the algorithm. The techniques used in this analysis are the same ones usually employed in the analysis of computational fluid dynamics schemes and are described in detail by Lomax *. A linear stability analysis of the scheme implemented for the solution of the aerodynamic equations, i. e. , the compressible Navier-Stokes equations, can be found in the literature (see for instance Reference[67] ) and will not be discussed here.

* Lomax,, H., Numerical Methods in Fluid Mechanics, Notes for course AA214A, Dept. of Aeronautics and Astronautics, Stanford University, Autumn Quarter, 1983.

The numerical algorithm being implemented here is given by Equation 3.7. Since the generalized aerodynamic forces are a *forcing term* in this case, for stability analysis we should take $\tilde{P}_{i,n} = 0$. Considering $q_{i,n+1} = \sigma q_{i,n}$, where $\sigma$ is the sometimes called *amplification factor*, and replacing this into Equation 3.7, one obtains

$$\sigma q_{i,n} = \frac{(2 - \Delta t^2 \varpi_i^2)\, q_{i,n} - (1 - \Delta t \zeta_i \varpi_i)\, \sigma^{-1} q_{i,n}}{(1 + \Delta t \zeta_i \varpi_i)} \tag{3.8}$$

Cancelling out the common term $q_{i,n}$ and solving for $\sigma$ we obtain

$$\sigma = \frac{(2 - \Delta t^2 \varpi_i^2) \pm \sqrt{\Delta t^4 \varpi_i^4 - 4 \Delta t^2 \varpi_i^2 (1 - \zeta_i)}}{2(1 + \Delta t \zeta_i \varpi_i)} \tag{3.9}$$

The stability requirement is given by

$$|\sigma| \leq 1 \tag{3.10}$$

or, in words, the stability region is described by the circle of unit radius in the complex $\sigma$-plane.

A complete analysis of the above expression for $\sigma$ is probably beyond the point we want to make here. It is interesting to note that there are essentially two parameters that have to be considered, namely $\Delta t \varpi_i$ and $\zeta_i$. Since for most practical applications the structural damping coefficient is a small quantity, it is instructive to study the limiting case when $\zeta_i$ is zero. In this case the expression for the amplification factor becomes

$$\sigma = \frac{1}{2}\left[\left(2 - \Delta t^2 \varpi_i^2\right) \pm \Delta t \varpi_i \sqrt{\Delta t^2 \varpi_i^2 - 4}\right] \tag{3.11}$$

which shows that the scheme is numerically stable for $\Delta t \varpi_i \leq 2$ for the case of zero structural damping. Since the structural frequencies that would be of interest are usually below 50 to 80 Hz, and also due to the fact that the nondimensional frequencies are being refered to the speed of sound, it is safe to state that $\varpi_i$ will, at its largest, be a number around unity. However, this shows that the conditional stability of the scheme poses no additional constraint on the time steps that could possibly be taken, because the maximum time step required to ensure time-accuracy of the aerodynamic equations alone is at least one order of magnitude, and quite

possibly two orders of magnitude, smaller than the one determined by the above condition. Moreover, the expression above shows that the modulus of $\sigma$ is exactly equal to 1 for all values of $\Delta t\,\varpi_i \leq 2$, which means that the numerical scheme is also non-dissipative*.

In support of previous statements, we will consider now the other possibility that has been suggested before, i. e. , to transform the second order equation into a system of first order ones and then use the explicit Euler method for the time march. We will show that this produces an unstable numerical algorithm. Rewriting Equation 3.2 as a first order system produces

$$\begin{cases} \dot{q}_i(t) = \nu_i(t) \\ \dot{\nu}_i(t) = \tilde{P}_i(t) - \varpi_i^2 q_i(t) - 2\zeta_i \varpi_i \nu_i(t) \end{cases} \tag{3.12}$$

where we are essentially defining a new variable $\nu_i \equiv \dot{q}_i$, and the *dots* indicate derivatives with respect to nondimensional time, as before. Using the explicit Euler method, we can write

$$\begin{cases} \dot{q}_i \cong \frac{q_{i,n+1} - q_{i,n}}{\Delta t} = \nu_{i,n} \\ \dot{\nu}_i \cong \frac{\nu_{i,n+1} - \nu_{i,n}}{\Delta t} = \tilde{P}_{i,n} - \varpi_i^2 q_{i,n} - 2\zeta_i \varpi_i \nu_{i,n} \end{cases}$$

which then produces the following set of finite difference equations

$$\begin{cases} q_{i,n+1} = q_{i,n} + \Delta t \nu_{i,n} \\ \nu_{i,n+1} = (1 - 2\Delta t \zeta_i \varpi_i)\, \nu_{i,n} - \Delta t \varpi_i^2 q_{i,n} + \Delta t \tilde{P}_{i,n} \end{cases}$$

For stability analysis, the forcing term is set to zero and we assume that $q_{i,n+1} = \sigma q_{i,n}$ and $\nu_{i,n+1} = \sigma \nu_{i,n}$. Writing the resulting equation in matrix form, we obtain

$$\begin{bmatrix} (\sigma - 1) & -\Delta t \\ -\Delta t \varpi_i^2 & (\sigma - 1 + 2\Delta t \zeta_i \varpi_i) \end{bmatrix} \begin{Bmatrix} q_{i,n} \\ \nu_{i,n} \end{Bmatrix} = 0$$

The characteristic equation is obtained by setting the determinant of the coefficient matrix to zero, which gives

$$(\sigma - 1)(\sigma - 1 + 2\Delta t \zeta_i \varpi_i) - \Delta t^2 \varpi_i^2 = 0$$

* Lomax., H., Numerical Methods in Fluid Mechanics, Notes for course AA214A, Dept. of Aeronautics and Astronautics, Stanford University, Autumn Quarter, 1983.

If we consider again the limiting case of zero structural damping, the roots of the above equation can be easily obtained as

$$\sigma_{1,2} = 1 \pm \Delta t \varpi_i$$

which shows the method is always unstable for any value of parameter $\Delta t \varpi_i$ . Numerical experiments support this theoretical result, indicating that in this case the instability of the explicit Euler method is a very practical problem.

# Chapter 4

# Study of Hemisphere-Cylinder Cases

## 4.1 Introduction

The aerodynamic code being used in the present investigation evolved from a version of the ARC3D code[41] that Deiwert and Rothmund[55] had running on a CDC Cyber 205 computer. The code had been optimized for the Cyber 205 architecture, but the formulation therein did not allow for general unsteady problems since it was missing the metric terms associated with time derivatives. The first major programming task undertaken here consisted of the introduction of the unsteady terms into the aerodynamic equations. Before attempting any aeroelastic analysis or even such complex configurations as the hammerhead, it was important to check the new code on some problem with a simpler geometry that would allow for validation of the modifications introduced.

Due to the simplicity of the geometry, while still keeping the general launch vehicle shape, a hemisphere-cylinder configuration was chosen to test the code. Such a configuration is also attractive from the standpoint that experimental or other computational results are available from the literature. The following sections will describe the cases studied with such configuration, which include steady state results for freestream Mach numbers of 0.5, 0.6, and 1.5 (all cases at zero angle of

attack), as well as unsteady results for a rigid body pitching oscillation. It should be noted that for these calculations the turbulence model was turned off, so that they are *laminar* computational results. Turbulent flow cases were run only for the hammerhead payload configurations, which will be discussed in the subsequent chapters.

## 4.2 Grid Generation

The body conforming computational mesh was generated using algebraic methods, and the same mesh was used for all hemisphere-cylinder cases analyzed. Grid lines run in the longitudinal, normal and circumferential directions, and 50, 40 and 20 grid points were used, respectively, in these directions. It should be pointed out that this is a fairly coarse grid system, since again the point of these computations was mainly to pinpoint any possible problems with the code before attempting any aeroelastic solutions on more complex geometries.

A general three dimensional view of body and grid can be seen in Figure 4.1, and details of typical grid planes, i. e. , longitudinal and crossflow planes, can be seen in Figure 4.2 . Mesh points in the normal direction are clustered near the body in order to capture viscous effects, and a 25% exponential grid stretching is used in this direction. Over the hemispherical part of the body, grid lines in the longitudinal direction are placed at equal angular increments, and over the cylindrical part of it, these lines are equally spaced. The 50 points used in the longitudinal direction are distributed such that 15 of them are over the hemispherical part of the body, and the other 35 are located along the cylindrical section. Grid lines in the circumferential direction are generated by rotating one longitudinal plane at equally spaced angles around the body. Note that two circumferential planes are overlapped in order to facilitate the enforcement of the boundary conditions when operating in this direction.

The positive orientation of the circumferential direction is chosen such that a right-handed system is obtained. In the present implementation of the code, this means clockwise for an observer looking at the body from upstream. This is very

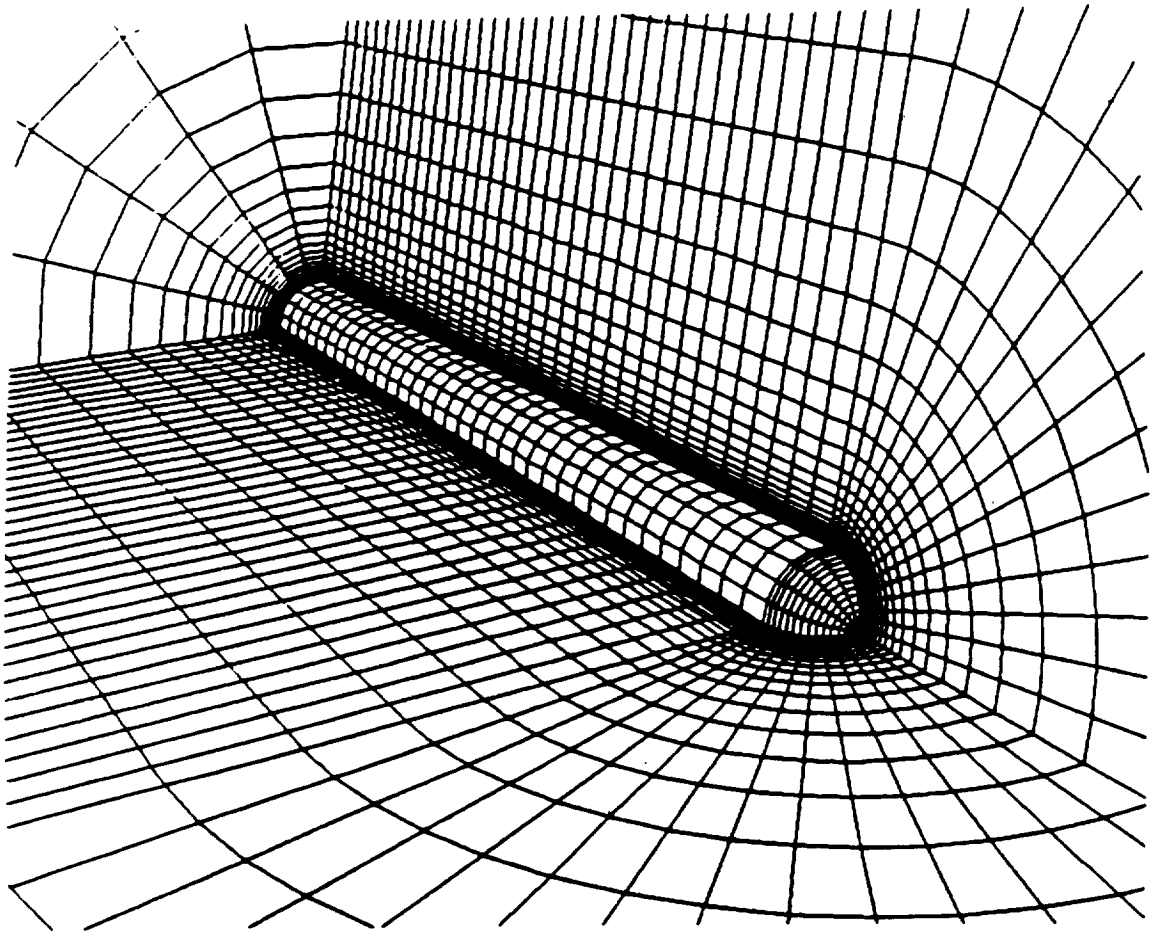

Figure 4.1: General three dimensional view of the hemisphere-cylinder grid.

ORIGINAL PAGE IS
OF POOR QUALITY

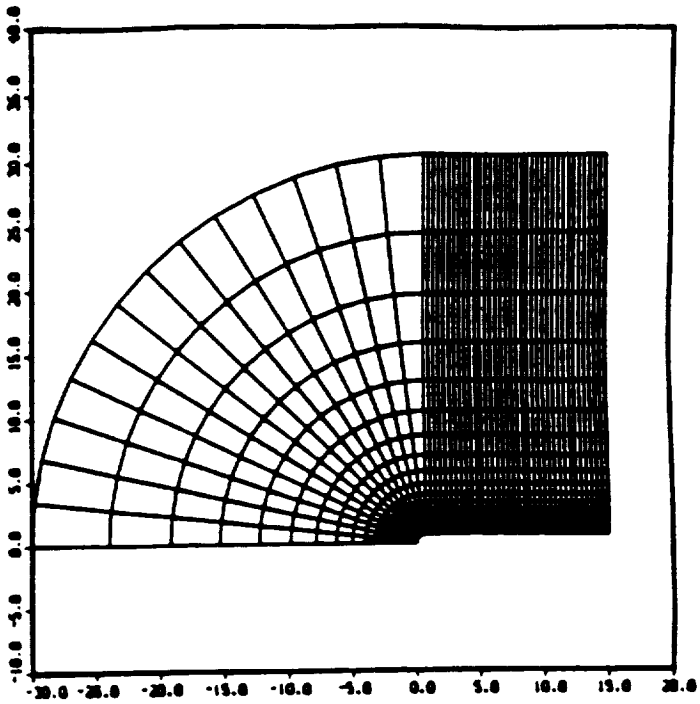

(*a*) Longitudinal plane.

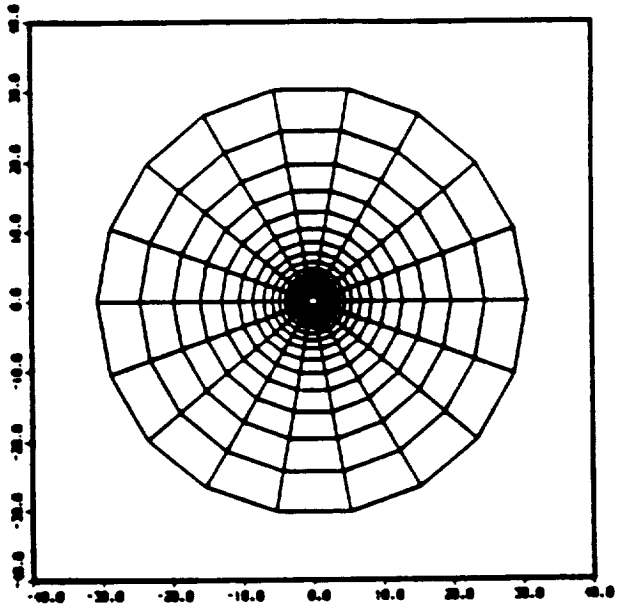

(*b*) Crossflow plane.

Figure 4.2: Details of hemisphere-cylinder typical grid planes.

important to ensure that anywhere on the body surface, or actually in the whole flowfield, the mathematical normal to any infinitesimal region is positive pointing outward. This becomes a crucial issue when computing particle traces with the graphics post-processing programs used to obtain the flow visualization figures that will be presented below.

## 4.3 Steady State Results

As initial tests for the code, we started with subsonic freestream cases. It is clear that low subsonic cases should converge faster to a steady state, because forward-going signals would propagate faster. However, one should be careful not to approach the incompressible limit. Essentially the problem is that we are using a compressible Navier-Stokes formulation, and the system of equations becomes ill-behaved when the incompressible limit is approached because the energy equation becomes redundant. Hence, for all the subsonic cases run here, care was exercised to ensure that some compressibility effects were present and the above described numerical problems avoided. Subsequently, one low supersonic case was run to verify the capabilities of the code for supersonic problems.

The first case run for the hemisphere-cylinder configuration was at a Mach number of 0.5, for zero angle of attack and a Reynolds number of 1.5 million based on the cylindrical section diameter. Pressure coefficient contours for the converged steady state solution along two opposing longitudinal planes can be seen on Figure 4.3 . Mach contours and density (nondimensionalized with respect to freestream) contours are also shown in the same figure. In this case it really does not matter whether these are side, or top, views of the body, because the solution is axisymmetric.

Since experimental results could not be found for this case in the literature, the present computations were compared to results obtained from another finite difference code, namely the F3D code[68, 53] generously made available to the present author by Ying*. Both codes have a Navier-Stokes formulation, and the laminar flow option was used. The F3D computations were performed on a Cray 2 supercomputer, but the grid system was essentially the same as that used for the

* Ying, S.X., personal communication, September 1986.

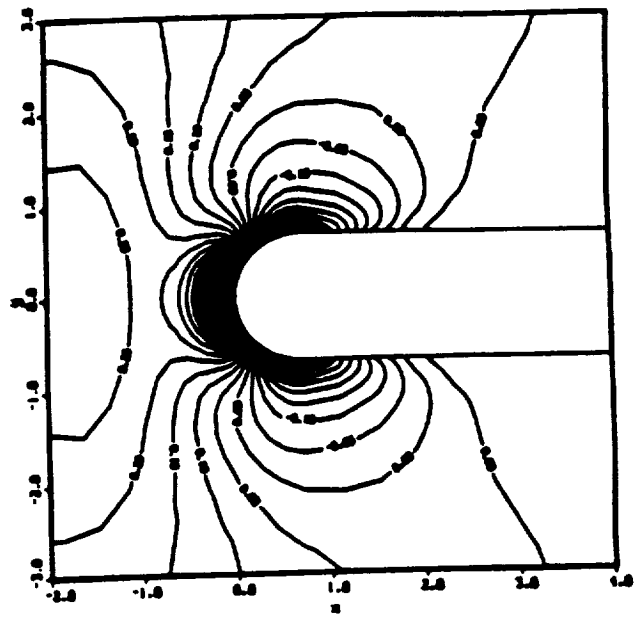

(a) Pressure coefficient contours.

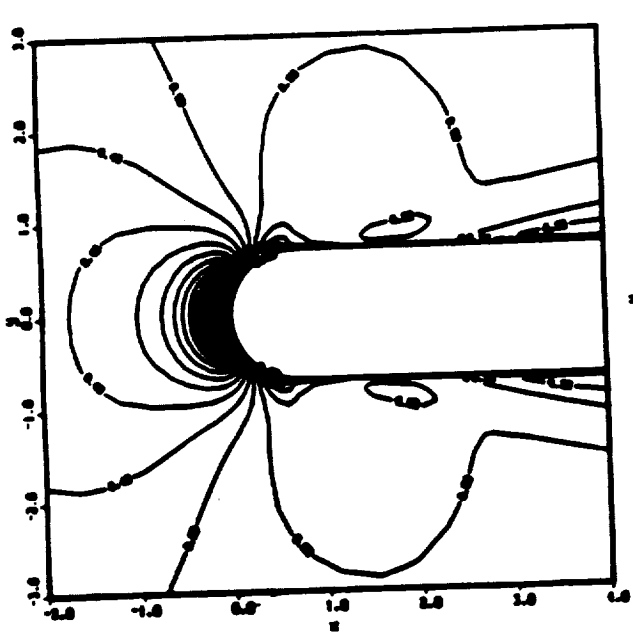

(b) Mach number contours.

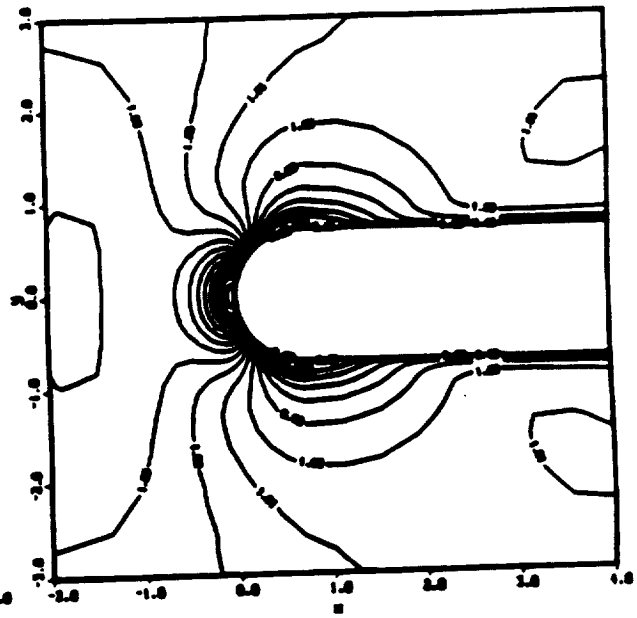

(c) Density contours.

Figure 4.3: Flow solution for hemisphere-cylinder at $M_\infty = 0.5$ and $\alpha = 0°$ .

ORIGINAL PAGE IS
OF POOR QUALITY

ORIGINAL PAGE IS
OF POOR QUALITY



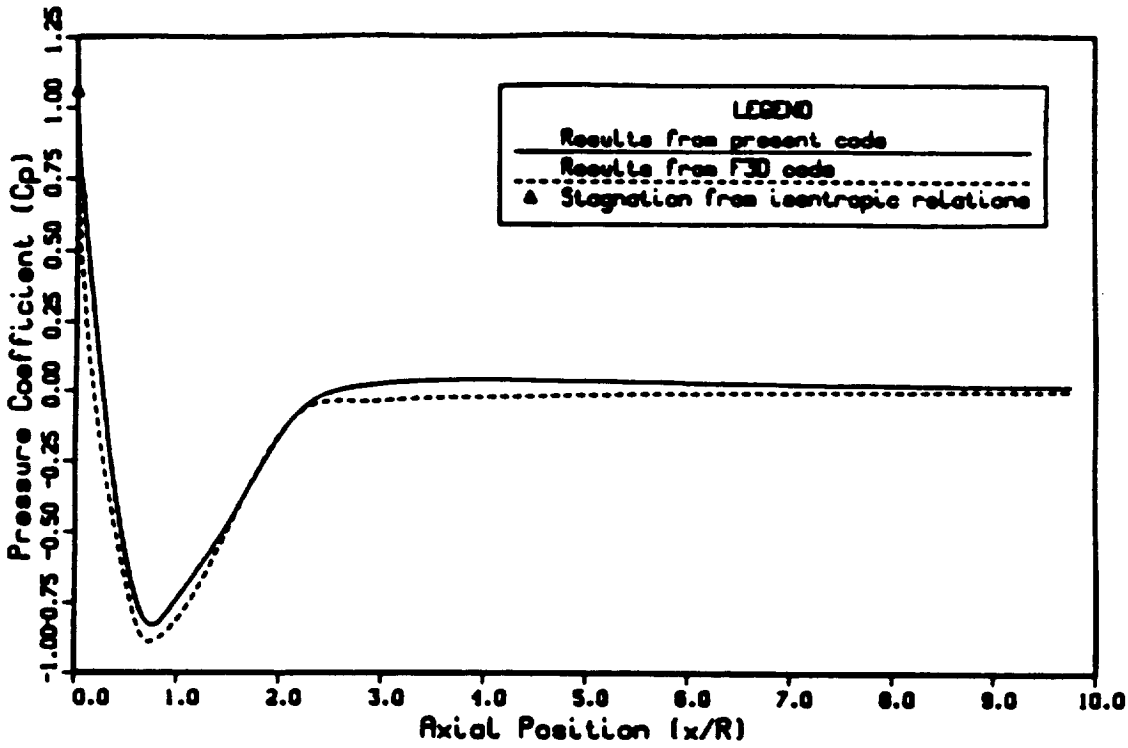


Figure 4.4: Pressure coefficient distribution on the body for hemisphere-cylinder at $M_\infty = 0.5$, $\alpha = 0°$, and $Re_D = 1.5 \times 10^6$ .

Cyber computations in order to make the two calculations comparable. Plots of the pressure coefficient distributions on the body for the two computations are presented on Figure 4.4 . As can be seen from this figure, the two computations show good agreement. The results from the F3D code indicate a *faster* expansion over the hemispherical part of the body, and also predict a slightly higher magnitude for the negative peak $Cp$ around the hemisphere-cylinder intersection. Both computations show this negative peak on the pressure coefficient occuring ahead of the hemisphere-cylinder intersection. The F3D results also seem to return faster to the freestream pressure value over the cylindrical section of the body. Also shown on Figure 4.4 is the value of the pressure coefficient at the nose stagnation point as predicted by isentropic relations [37]. These relations predict $Cp = 1.06$ at the stagnation point, and both calculations agree well with that value.

The next hemisphere-cylinder case studied involved a flight Mach number $M_\infty =$

0.6, zero angle of attack, and the Reynolds number $Re = 490000$ based on the reference diameter. The Reynolds number in this case was chosen to match the experimental results presented by Hsieh[69, 70], whose wind tunnel static pressure distributions for a hemisphere-cylinder are in the Mach number range of interest for this work and therefore were used for these benchmark computations. Computational values of pressure coefficient, Mach number, and density contours for this case are shown in Figure 4.5 . It can be seen from Figure 4.6 , which shows pressure coefficient distributions on the body for both the present computation and experiment[69], that the computed results agree well with the experimental ones. The only region along the body where the computations seem to have some difficulty in following the experiment is on the recompression side of the expansion region around the hemispher-cylinder intersection. However, it is well known that expansion regions are particularly difficult to predict accurately. Considering that this is such a coarse grid system it is fair to say that the code is doing a good job in this case. It should also be noted that the negative peak $Cp$ is being very well predicted, both in strength and location.

Finally, it is important to point out that this a fully subsonic flow, in other words, there are no supersonic pockets in it. Although the ultimate objective of this work is to investigate transonic flows, it was felt that the grid system was too coarse to try to capture transonic shocks and all the possible complexity associated with them, such as shock-boundary layer interactions and flow separation due to those interactions. For this reason, no transonic cases were analyzed for the hemisphere-cylinder configuration, and instead a low supersonic case is considered next. Transonic flow examples were studied for the hammerhead configurations, in which case much more refined grids were created.

Computational results for a freestream Mach number $M_\infty = 1.5$ case can be seen in Figure 4.7. In this example the Reynolds number was 1.386 million, based on the reference diameter, and again zero angle of attack was considered. A plot of the bow shock location, calculated based on pressure gradient results, is shown in Figure 4.8 . It should be pointed out that in Figure 4.8($b$) we actually have a complete shock surface. It was plotted only as lines in order to let the body

ORIGINAL PAGE IS
OF POOR QUALITY

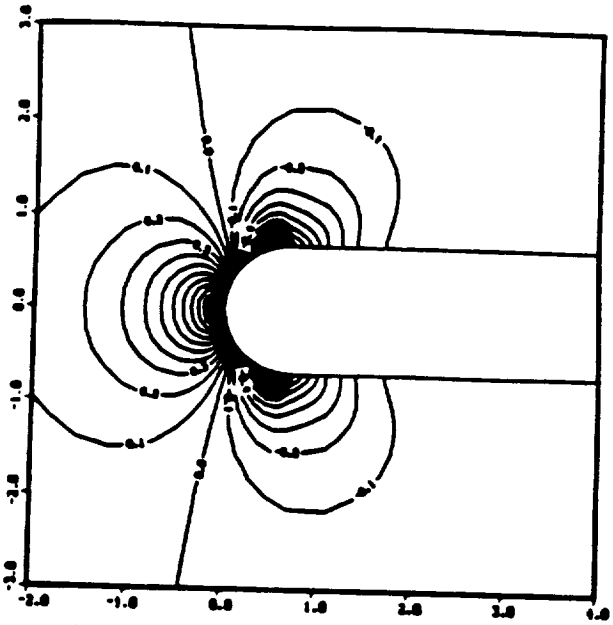

(a) Pressure coefficient contours.

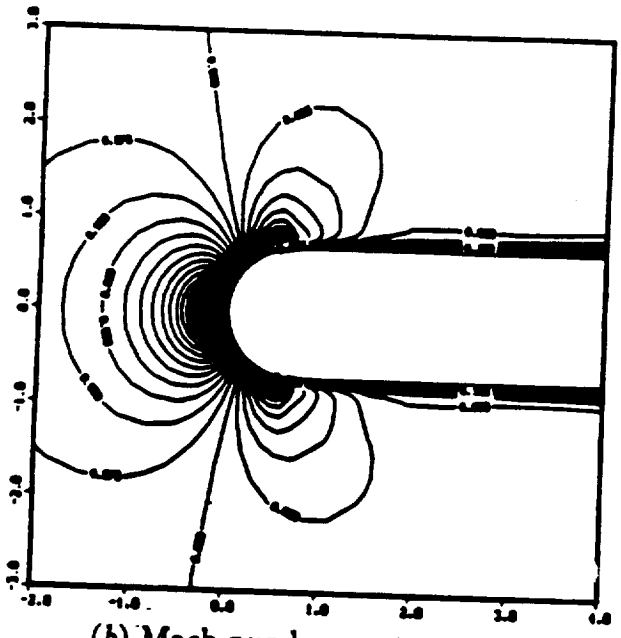

(b) Mach number contours.

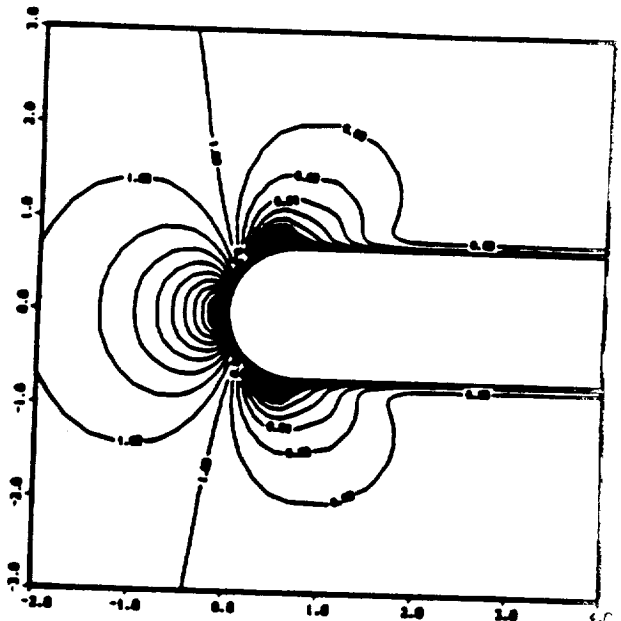

(c) Density contours.

Figure 4.5: Computed flow solution for hemisphere-cylinder at $M_\infty = 0.6$, $\alpha = 0°$, and $Re_D = 490000$ .

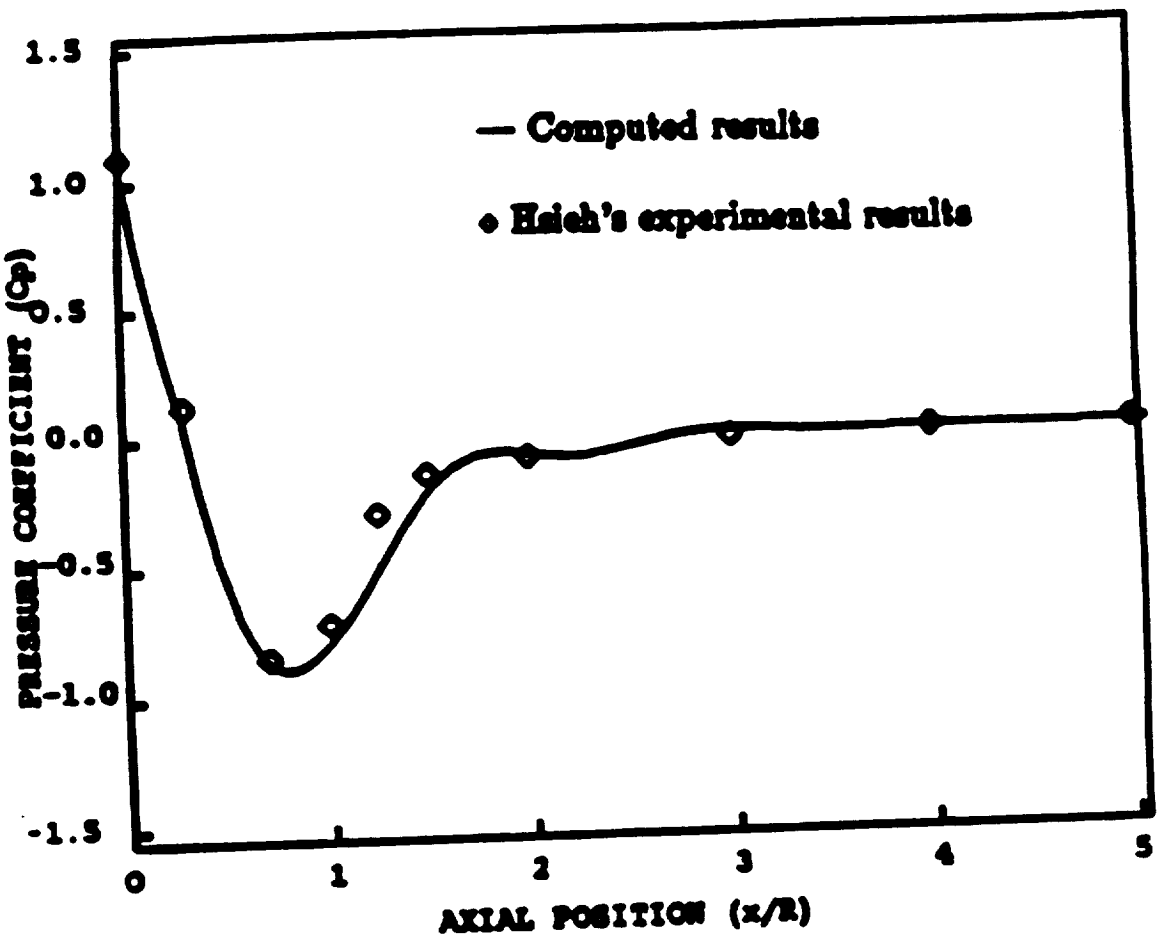


Figure 4.6: Pressure coefficient distribution on hemisphere-cylinder at $M_\infty = 0.6$ and zero angle of attack.

ORIGINAL PAGE IS
OF POOR QUALITY

ORIGINAL PAGE IS
OF POOR QUALITY

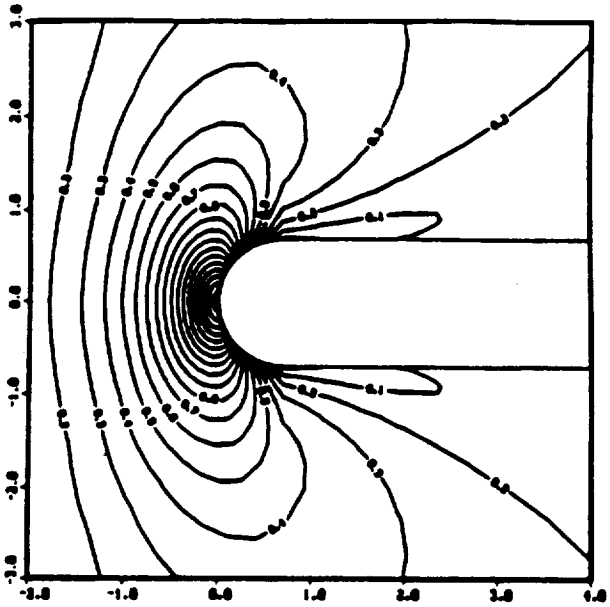

(a) Pressure coefficient contours.

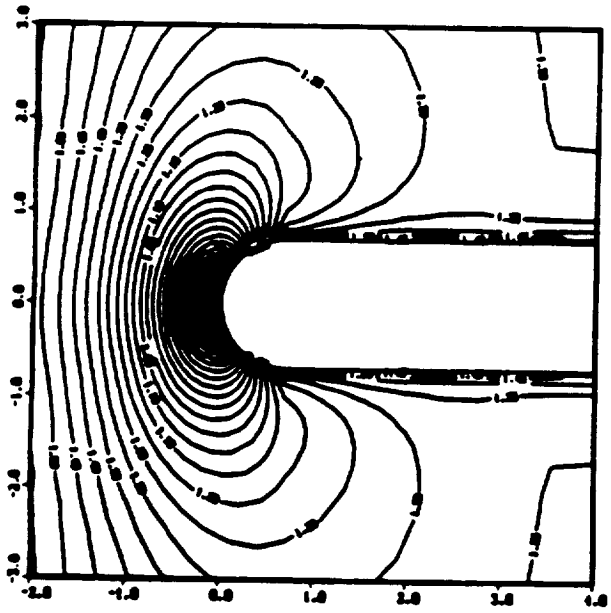

(b) Mach number contours.

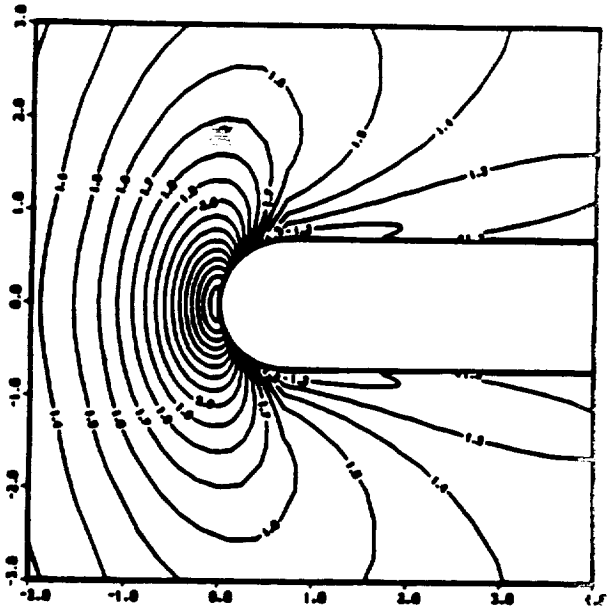

(c) Density contours.

Figure 4.7: Computed flow solution for hemisphere-cylinder at $M_\infty = 1.5$, $\alpha = 0°$, and $Re_D = 1.386 \times 10^6$ .

ORIGINAL PAGE IS
OF POOR QUALITY

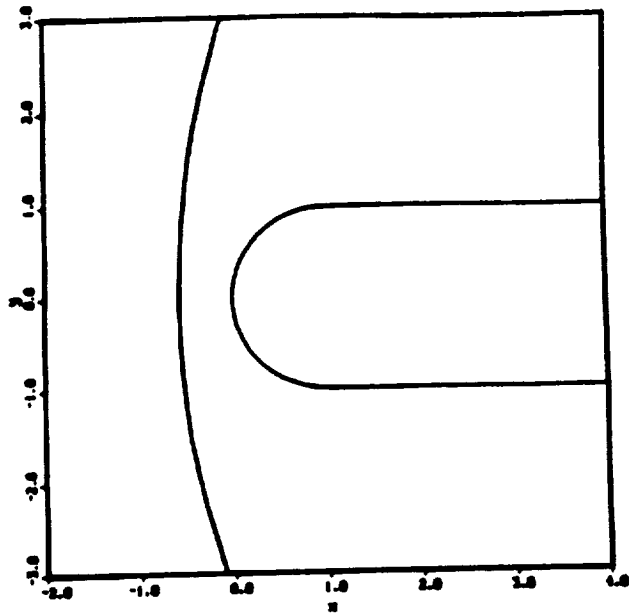

(a) 2-D view.

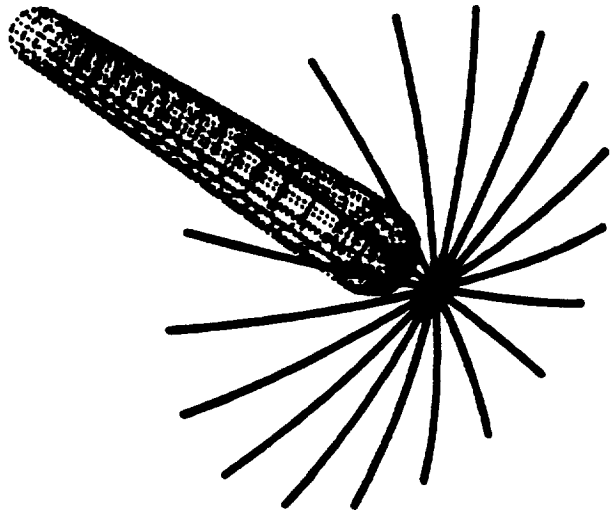

(b) 3-D view.

Figure 4.8: Shock location based on pressure gradient for hemisphere-cylinder at $M_\infty = 1.5$ and $\alpha = 0°$ .

also be seen behind the shock. The shock standoff distance can be calculated as $-0.57$ , nondimensionalized with respect to the radius of the cylindrical section. This result compares well with the value of $-0.60$ for the shock standoff distance for a hemisphere-cylinder obtained from shadowgraphs, presented in Reference [69]. It is clear, however, from the contour plots in Figure 4.7 that the computations are not capturing such a crisp, well-defined shock as Figure 4.8 suggests. The most obvious reason for this failure is the coarseness of the grid. But the main point we intend to demonstrate with these results, namely, that the code is capable of performing well for supersonic freestream conditions, is still valid. The results are in the correct range despite the fact we have used a coarse grid.

Although the steady state cases studied for the hemisphere-cylinder configuration cannot be considered extremely difficult problems for many existing computational fluid dynamics codes, the results shown provided enough confidence in the present code that we moved on to more complex examples. The steady state solution described above for a freestream Mach number $M_\infty = 0.6$ was used as the initial solution for the study of a forced unsteady case, which will be described next.

## 4.4 Pitching Oscillations

As a first actual unsteady test of the code, the hemisphere-cylinder vehicle was subjected to a rigid body sinusoidal pitch oscillation in a flow with $M_\infty = 0.6$ . The nondimensional frequency of the oscillation was taken as 0.4, and the half-amplitude angle of the oscillation was $\theta_0 = 5°$ . The pitch axis was considered to be at the computational downstream boundary, which in this case is about 10 body diameters from the nose. The steady state solution previously obtained at this Mach number was used as initial condition for the unsteady calculation as previously mentioned.

It should be pointed out that the frequency of the oscillation is rather large, perhaps two to four times larger what one should realistically expect to find in flight. Since experimental, or computational, results could not be found in the literature for the type of oscillatory motion we were interested in, regardless of the value of frequency considered, the high value of dimensionless frequency was chosen mainly

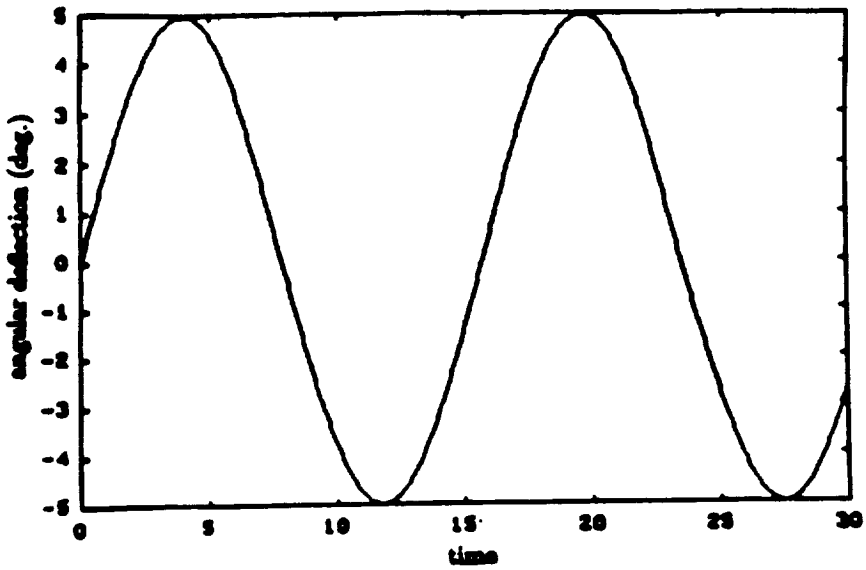


Figure 4.9: Angular amplitude of centerline deflection for forced sinusoidal pitching oscillation.

to allow for a faster computational turnaround time. The reader should observe that, for the cases considered here, the maximum allowable time step was completely determined by the aerodynamics. The body motion, however, is determined by the product $\varpi\Delta t$ . It is important to note that, despite the coarse grid being used, the computational costs of these unsteady calculations is not negligible. Since the idea behind these computations was primarily one of checking on the code, a higher frequency would still allow for some qualitative study of the performance of the code, while permitting a faster turnaround.

The angular deflection of the body centerline, versus time, is shown in Figure 4.9 . Time histories of the running normal force, i. e. , the normal force per unit of axial length for two axial stations along the body, can be seen in Figure 4.10 . It is important to point out that the "time" on both figures is the nondimensional time. The distribution of the running normal force along the body is shown in Figure 4.11 for several instants of time during the oscillation. Unfortunately no experimental or computational results could be found to compare with the present calculations, but they seem to produce the kind of behavior that could be expected for this forced oscillation.

ORIGINAL PAGE IS
OF POOR QUALITY

ORIGINAL PAGE IS
OF POOR QUALITY

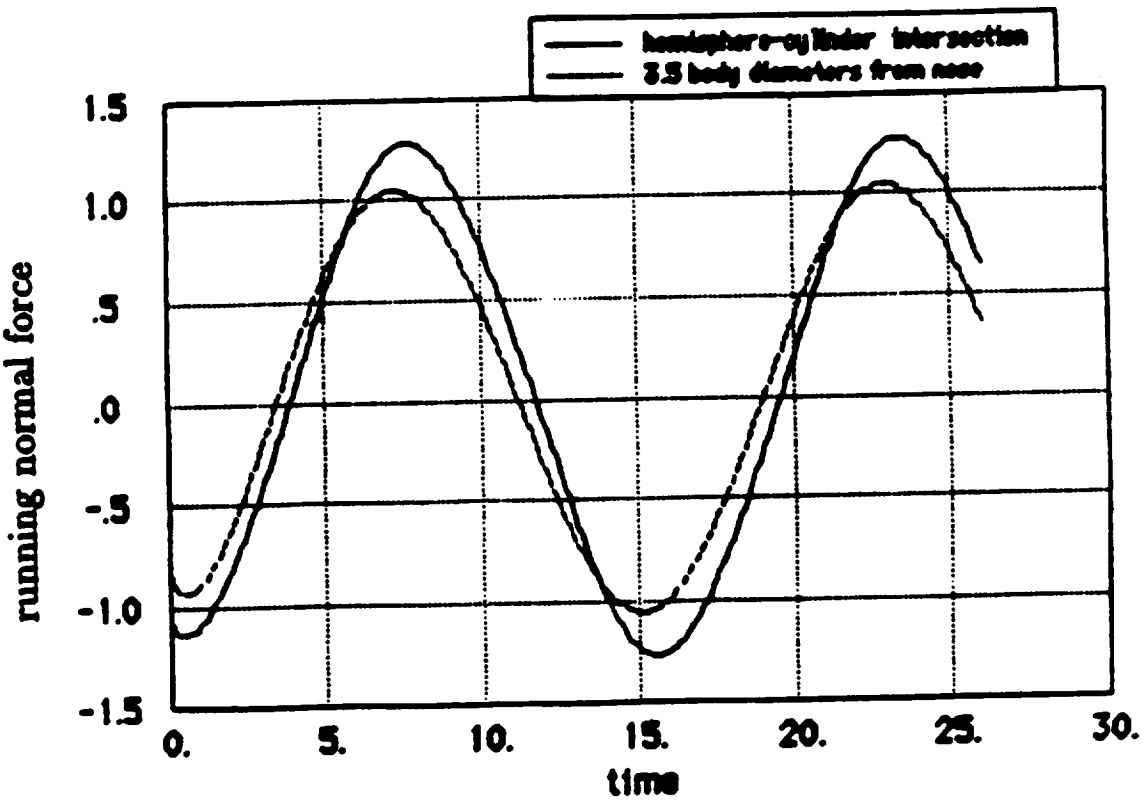


Figure 4.10: Unsteady aerodynamic load on a hemisphere-cylinder undergoing a sinusoidal pitching oscillation with $\overline{\omega} = 0.4$ ($M_\infty = 0.6$ , $\alpha = 0°$ , $\theta_0 = 5°$) .

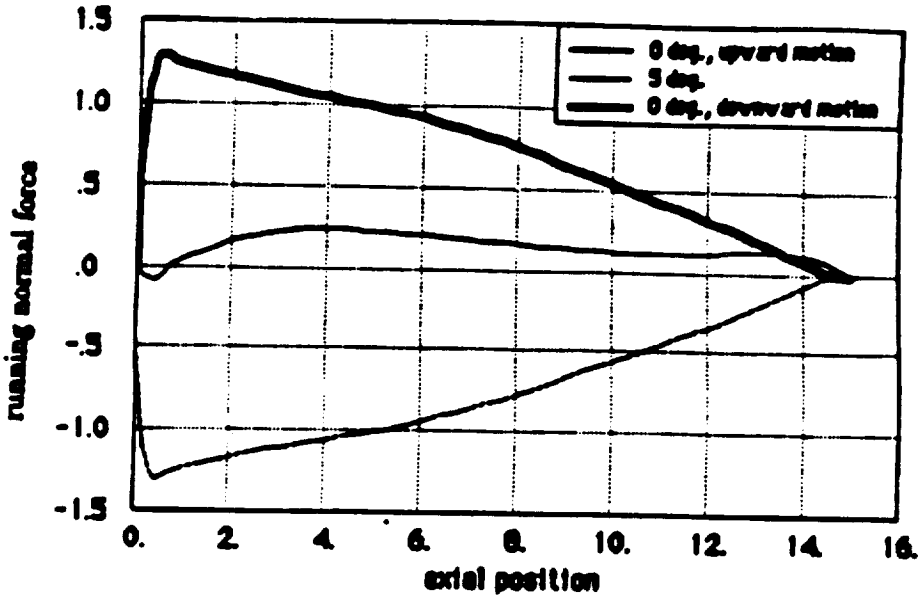


(a) Distributions for $\theta = 0°$ (upward and downward motions) and for $\theta = 5°$ .

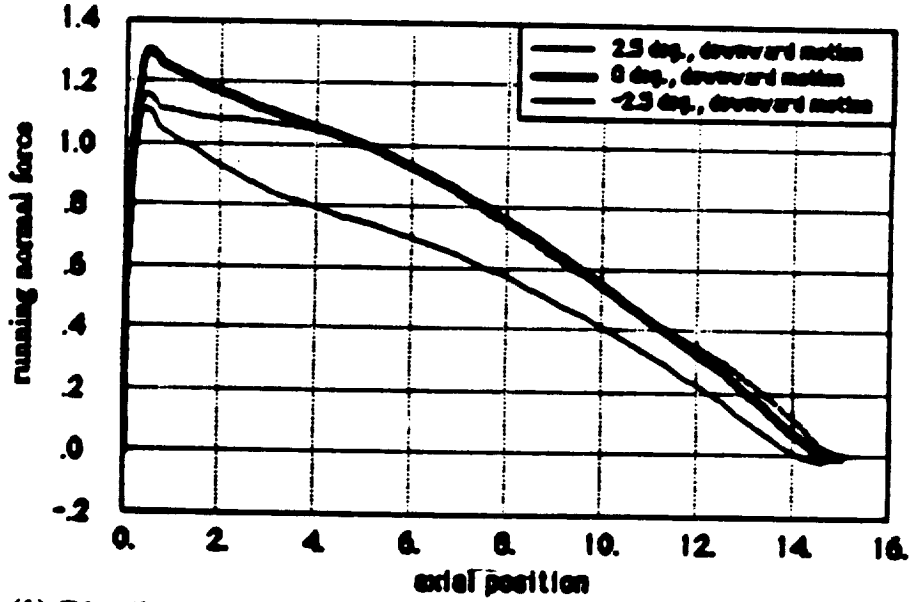


(b) Distributions for $\theta = 2.5$ , 0. , and $-2.5°$ , downward motion.

Figure 4.11: Comparative plots of unsteady aerodynamic load distribution on hemisphere-cylinder in pitch oscillation ($M_\infty = 0.6$ , $\alpha = 0°$ , $\varpi = 0.4$ , $\theta_0 = 5°$).

From Figures 4.10 and 4.11 one can see that the unsteady aerodynamic loads on the body lag the motion with a phase shift of almost 90°, and that the influence of the freestream angle of attack at any instant along the oscillation is very small in determining the total load at that time instant. For example, from Figure 4.11 we can see that at $\theta = 0°$ in the downward stroke the load is close to its maximum value, and at the "top" of the oscillation, $\theta = 5°$, the load is actually very small. In other words, the loads in phase with the angular displacement are small compared to the ones induced by body oscillating velocities. Figure 4.10 also shows that the phase lag decreases as we move from the forebody to the aft portion of the body, as one might expect since the pitch axis is located at the downstream boundary.

The reason for such a large phase lag in the aerodynamic forces, when compared to the body motion, is easy to understand in the light of the very high value of nondimensional frequency. Actually, in this case, the velocities induced by the motion on the forebody are comparable to freestream velocities. Since we start with a steady flow at time zero, we expect that the flow field will settle down to its steady-state, simple harmonic limiting behavior after some time. The high frequency also explains why these initial transients die out quickly in this case, which can be seen from Figure 4.12 , where the running normal force distribution along the body is shown for the same pitch angle position at two different cycles of the oscillation. The curves almost coincide, indicating that after only a half-cycle of oscillation the initial transients have already died out.

In summary, for such a heavily forced oscillation, one should expect to see the aerodynamic loads being determined primarily by the motion itself, and the present computations indeed display this feature. Although the unsteady computations could not be validated against any experimental results, the correct expected behavior is reproduced by the present calculations. The main objective of the analysis of the hemisphere-cylinder configurations can be considered as accomplished. In the following sections we will turn our attention to the primary focus of the present work, which is to apply the unsteady aerodynamic formulation to the analysis of aeroelastic problems in the transonic flight regime.

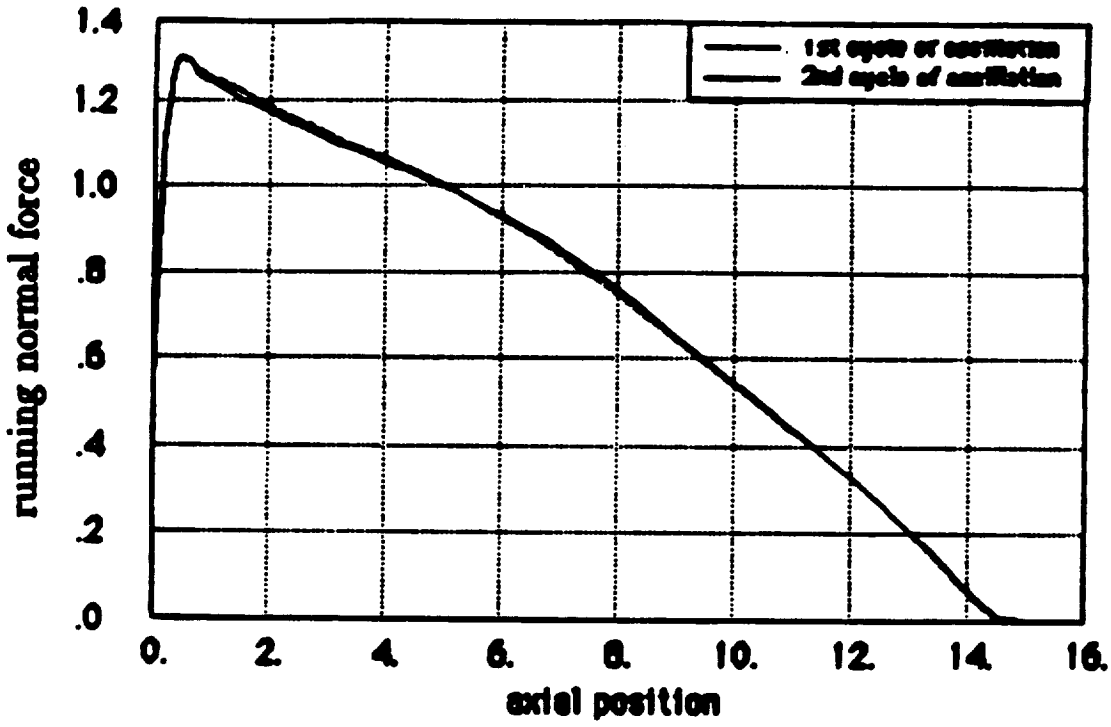


Figure 4.12: Unsteady aerodynamic load distribution on a pitching hemisphere-cylinder at $\theta = 0°$ (downward motion) for the 1st and 2nd cycles of oscillation.

# Chapter 5

# A General Hammerhead Payload Problem

## 5.1 Preliminary Remarks

The configuration under consideration in this section does not attempt to reproduce the geometry of any particular vehicle, but it has all the major characteristics one is likely to encounter in a hammerhead payload. For instance, it has a blunt nose and the payload diameter is larger than the adjacent boosting stage (which implies the existence of some form of boattail on the forebody). There is a flare region which is bound to produce a good portion of the normal force on the vehicle for small angles of attack and that can possibly be subjected to large unsteady forces due to flow separation in the boattail region.

It is clear that the study of a configuration which does not correspond to any existing vehicle makes it difficult to compare or validate whatever results are obtained. For aeroelastic analysis the problem is compounded, because not only external geometrical similarity is necessary but also mass and stiffness similarity would be required in order to compare any results correctly. However, at this point in the course of the research, we had not found actual data for an existing vehicle in the literature. We considered that it was worthwhile to exercise the method just to show what might be possible after more realistic data could be obtained.

## 5.2 The Grid System

The computational mesh about the chosen hammerhead payload was also generated by algebraic methods. The grid has 105 points in the longitudinal direction, 66 points in the normal (actually *nearly* normal) direction, and 38 points in the circumferential direction. Once a longitudinal plane of the grid is generated, this plane is rotated through 360° to create the full three dimensional grid. The $\eta$-direction in this case is being called *nearly* normal because, in the boattail and flare regions of the grid, the $\eta$-lines do not intercept the body surface at 90° angles.

A general three dimensional view of the body and the grid is shown in Figure 5.1 . A typical longitudinal plane of the grid can be seen in Figure 5.2($a$) , and details of the forebody and flare regions are shown in Figures 5.2($b$) and ($c$) . The latter illustrates the $\eta$-lines not intercepting the body surface at right angles in the boattail and flare regions. This is not the ideal way of creating a computational mesh, since in principle we want the *normal* coordinate lines indeed coming in normal to the body. A small numerical error is expected due to the fact that this is not precisely true. However, numerical computations of boattail flowfields by Deiwert[57] indicate that this does not cause enough numerical problems to justify a more elaborate grid generation scheme, if the boattail (or flare) does not have a very steep slope. Moreover, when performing aeroelastic analyses, the grid will deform as the computation proceeds, and it can be very difficult to ensure that $\eta$ grid lines do not cross over each other if the grid generation scheme gets to be too complex.

Since true transonic solutions are attempted, it is important in this case to have a better clustering of the grid points along the body (in the longitudinal direction) in regions where high gradients are likely to occur. For this reason, one parameter hyperbolic tangent grid stretching[56] is used to cluster the grid points around the hemisphere-forebody cylinder and the flare-afterbody cylinder intersections. In order to improve the resolution on the upstream centerline region, one-parameter hyperbolic tangent grid stretching is also used to cluster grid points around the upstream centerline. To avoid *wasting* grid points on the downstream part of the

ORIGINAL PAGE IS
OF POOR QUALITY

# CHAPTER 5. A GENERAL HAMMERHEAD PAYLOAD PROBLEM

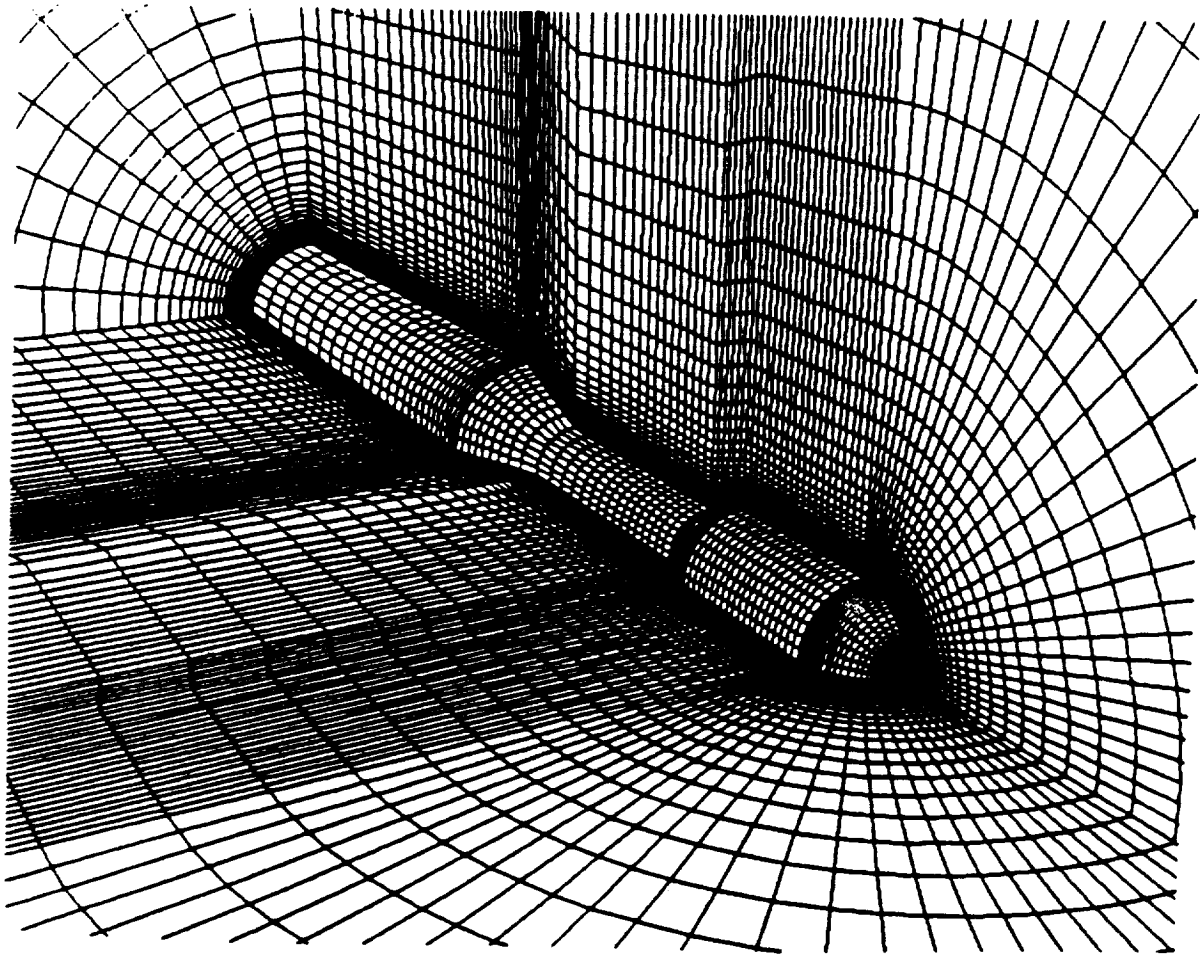

**Figure 5.1: Three dimensional view of general hammerhead payload configuration grid system.**

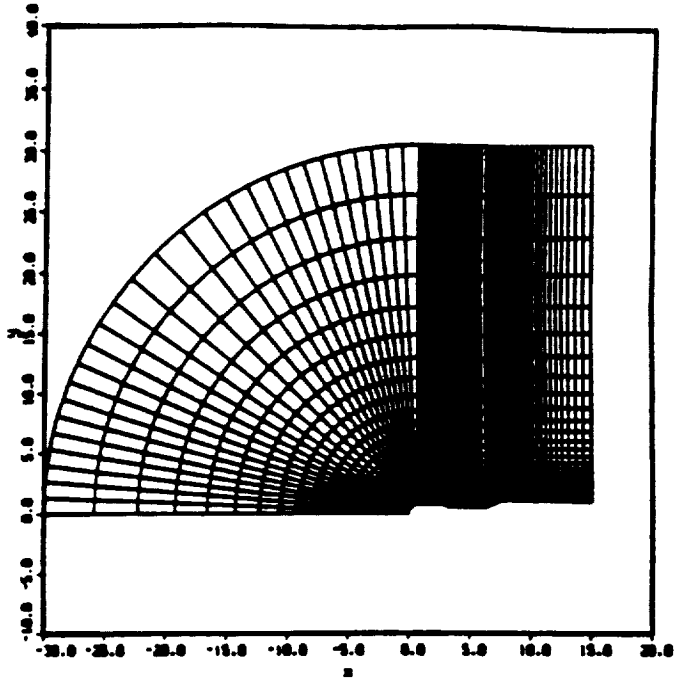

(a) Complete plane.

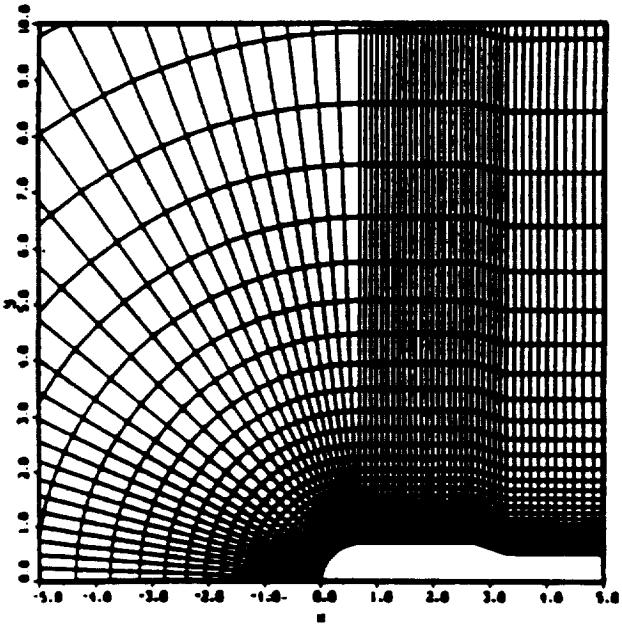

(b) Detail of forebody region.

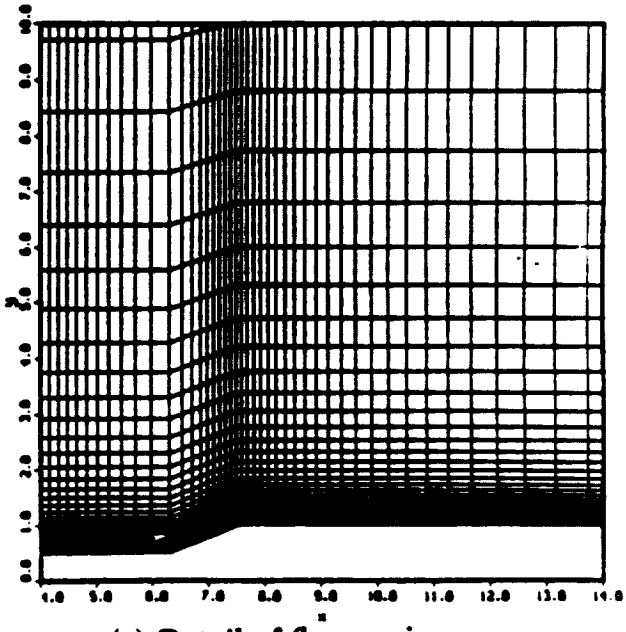

(c) Detail of flare region.

Figure 5.2: Typical longitudinal grid plane for hammerhead payload.

ORIGINAL PAGE IS
OF POOR QUALITY

afterbody cylinder, where not much is happening, a 8.5% exponential stretching is used to increase the grid spacing towards the downstream boundary. In the normal, or nearly normal, direction a 16% exponential grid stretching is used everywhere in order to cluster grid points near the body for capturing viscous effects.

## 5.3 Initial Aerodynamic Solution

As previously explained, before the structural-dynamic equations are turned on, an initial aerodynamic solution must be obtained at the desired flight condition under the assumption that the body is rigid. This is done by initializing all the flow variables with freestream conditions, imposing the appropriate boundary conditions for the problem, and then letting the aerodynamic solver march the solution in time until some steady state condition is achieved. An important caution, however, is that one should be aware that, for these transonic freestream conditions, a true *steady state* condition is not necessarily obtained. It is possible that the aerodynamic solution by itself is unsteady. In these cases what is being searched for in this initial phase is is a correct possible solution for the flowfield around the body at that particular flight condition.

For the examples considered here, however, true steady state solutions were obtained in this initial phase. The steady state flow solution was calculated over this geometry for a freestream Mach number $M_\infty = 0.85$, an angle of attack $\alpha = 6°$, and the Reynolds number $Re = 1.26 \times 10^6$ (based on the diameter). The flow, or rather the boundary layer, was considered turbulent, i. e. , the turbulence model was turned on. Pressure coefficient contours, Mach number contours and density contours for leeside and windside are shown on Figure 5.3, where essentially we are looking at a side view of the body. The expected flowfield features are reproduced by the computation. For instance, the expansion regions around the hemisphere-forebody cylinder intersection and around the flare-afterbody cylinder intersection are clearly shown on the figures. A mild expansion around the forebody cylinder-boattail intersection can be seen, and the compression region on the face of the flare, mainly on the windside, is also very well defined.

ORIGINAL PAGE IS
OF POOR QUALITY



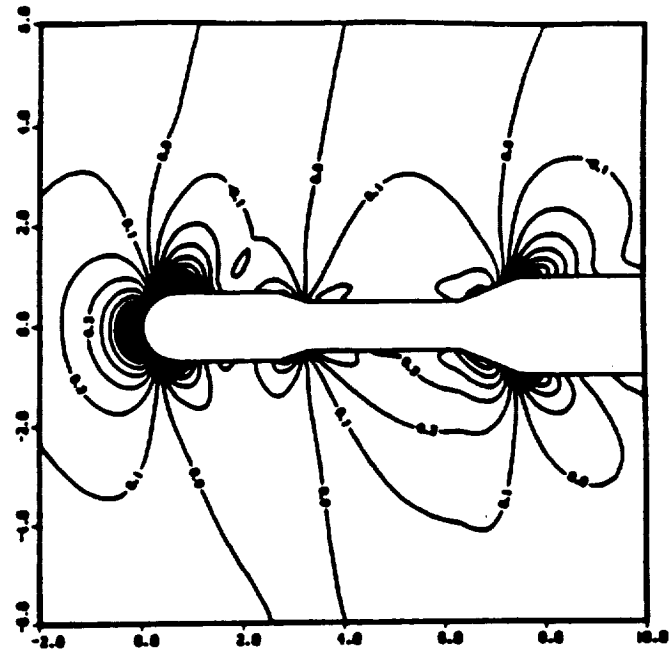

(*a*) Pressure coefficient contours.

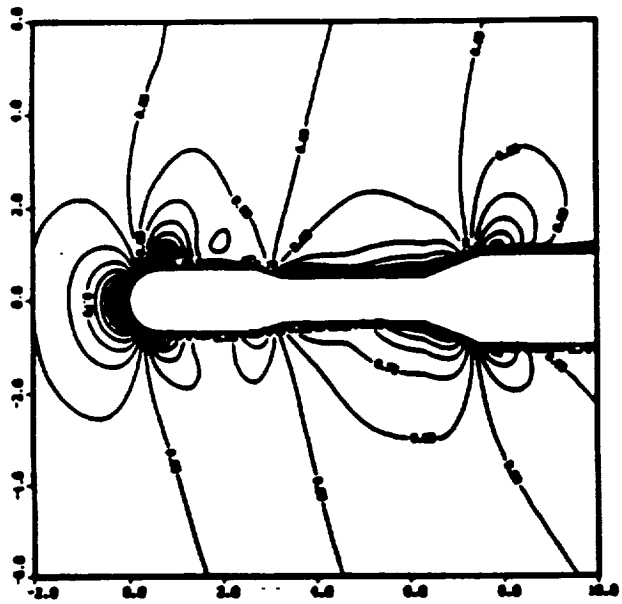

(*b*) Mach number contours.

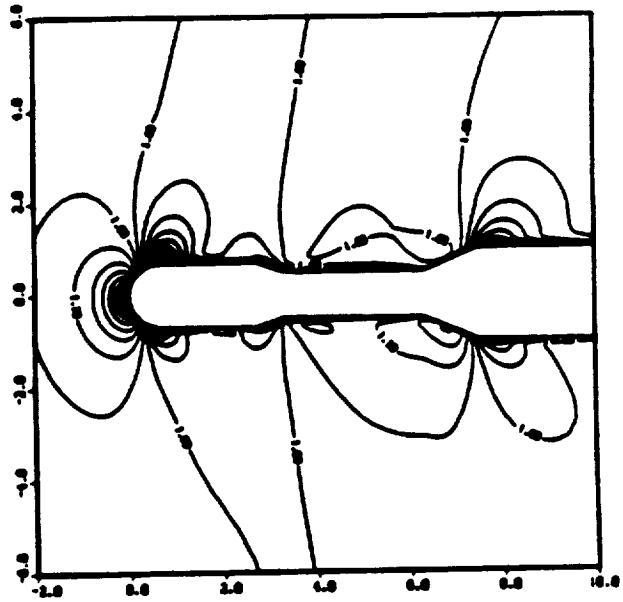

(*c*) Density contours.

Figure 5.3: Flow solution about a hammerhead geometry at $M_\infty = 0.85$ , constant $\alpha = 6°$ and $Re_D = 1.26 \times 10^6$ (side view).

All these features are even more apparent from Figure 5.4 , which shows leeside and windside pressure coefficient distributions on the body. As mentioned, these pressure distributions seem to have all the characteristics that would be expected, except that a more clearly defined shock was expected to be seen on the leeside of the forebody. Although we do not have experimental data with which to compare these pressure coefficient distributions, it is worth noting that the magnitudes of the negative peak $Cp$ on the hemisphere-forebody cylinder intersection are in the correct range for this flight condition.

An interesting point that was discussed previously concerning the downstream boundary conditions can be clearly understood from Figure 5.4 . One can see that, on the afterbody cylinder, the pressure coefficient has a constant value different from zero for a good portion of this body section; it then smoothly drops to zero at the downstream boundary. Of course, there is no surprise that $Cp$ is zero at the downstream boundary, because we are enforcing that as boundary condition. However, the existence of a flat region in the $Cp$ distribution ahead of the downstream boundary evidences that there is an error in the boundary condition. If the computational domain is extended further downstream, perhaps with the inclusion of a body base, the flow would converge to a nonzero value of pressure coefficient at the body location where the boundary condition is currently being enforced. On the other hand, the existence of this flat region is also an assurance that whatever errors are being produced at the downstream boundary are not propagating far enough upstream in order to influence the region of real interest in this case, which is mainly the forebody.

It should be clear that the amount of data generated in these three dimensional computational solutions is very large. The study of scalar flow variable contours may prove inadequate to understand what is really happening. To this end, particle traces are very useful. In particular, particle traces restricted to the first computational $\eta$-plane away from the body amount to computer generated *oil-flow* pictures and are almost indispensable to understand the topology of the flow. It should be pointed out that the latter can also be interpreted as plots of the skin-friction lines on the body. We shall not go into any detailed discussion of these flow topologies,

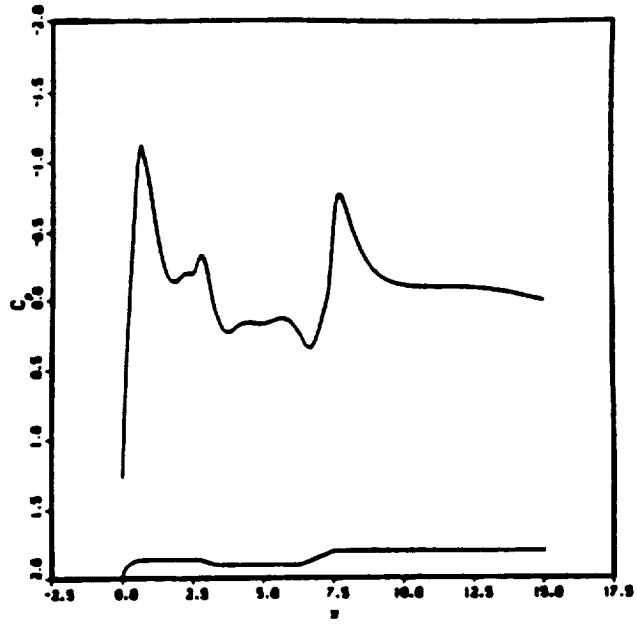

(a) Leeside.

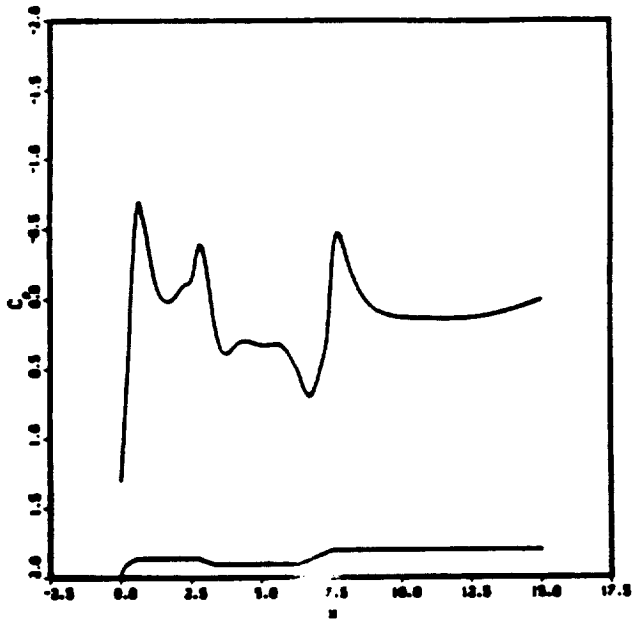

(b) Windside.

Figure 5.4: Pressure coefficient distribution along the body for a hammerhead payload at $M_\infty = 0.85$ , $\alpha = 6°$ , and $Re_D = 1.26 \times 10^6$ .

ORIGINAL PAGE IS
OF POOR QUALITY

except to point out lines of separation and/or reattachment which will help us understand the solutions that are being obtained. The reader interested in detailed discussions of topological flow structures is refered, for example, to the works of Dallmann[71, 72], Kaynak, Holst and Cantwell[73], and Deiwert[74] .

Figure 5.5 shows these computer generated oil-flow pictures for this configuration at the converged steady state solution. One can clearly identify a separation region on the cylindrical forebody right after the hemisphere-cylinder intersection, and a node of separation can be seen on the lee generator just behind this intersection. There is another separation line on the boattail, which indicates that even the windside experiences some flow separation in that region. The line of reattachment aft of the boattail is also clearly defined in the figures. All those cases can be considered mild separations, in the sense that the regions of reversed flow are rather limited. Figures 5.6($a$) and 5.6($b$) show velocity profiles for the leeside in the regions of separation on the forebody cylinder and boattail, respectively. The reversed flow directions are apparent, indicating the backflow condition in the separation regions.

The convergence to steady state was rather slow, which is expected for a transonic flow condition. To achieve convergence, 4000 time steps (iterations) were needed. It should be mentioned that, for the $105 \times 66 \times 38$ grid being used, each iteration takes approximately 10 CPU seconds in a CDC Cyber 205 computer. The overall system time, however, is a little higher than what would be estimated from this figure, because the database is not core contained. Data must be shifted back and forth from disk. As explained before, the database is structured in a pencil format, and the metrics of the transformation are what is kept in outside disk files. When operating in a particular direction, the metrics for that direction must be read in from those files. Due to the use of asynchronous I/O, this can be done without degrading very much the performance of the code for steady state problems. In the present example, the CPU time represented approximately 60% of the overall system time.

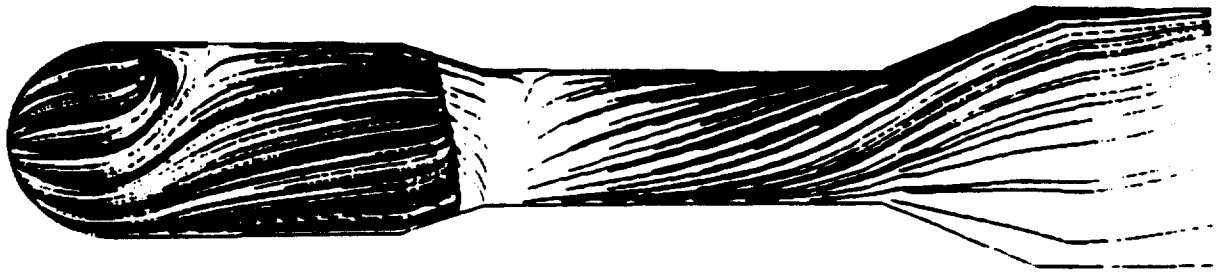

(*a*) Side view.

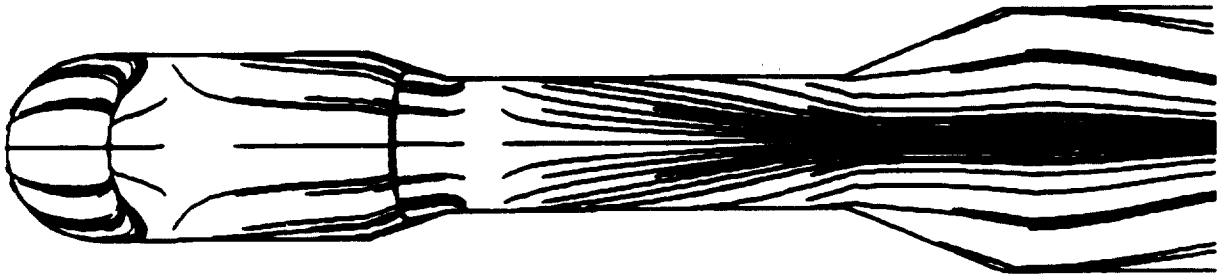

(*b*) Top view.

Figure 5.5: Computer generated oil-flow lines for general hammerhead payload at $M_\infty = 0.85$ and $\alpha = 6°$ .

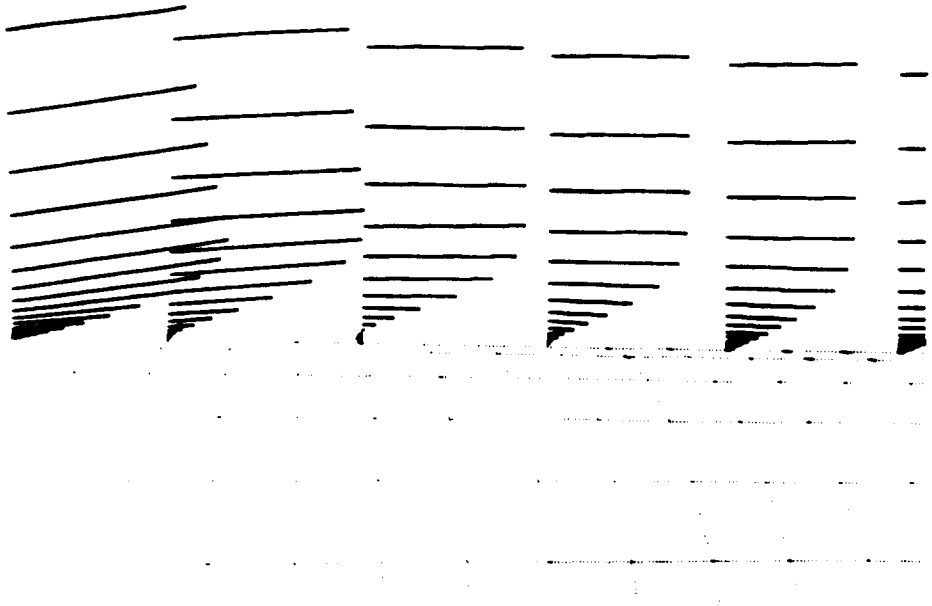

(a) Forebody cylinder region.

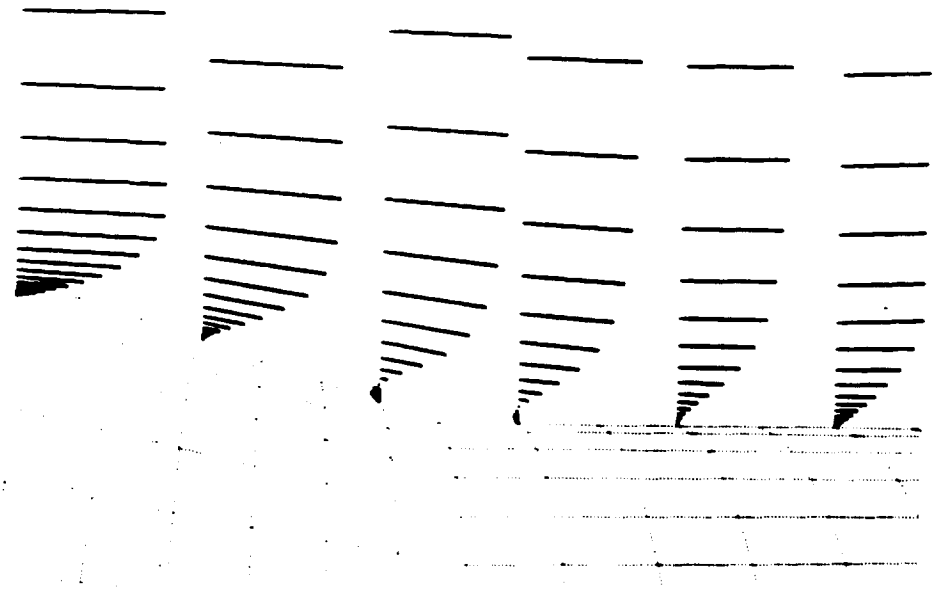

(b) Boattail region.

Figure 5.6: Velocity profiles on the leeside in the regions of flow separation (side view).

## 5.4 Aeroelastic Analysis

The steady state aerodynamic solution described in Section 5.3 will be used as the starting flow for the aeroelastic cases studied here. Since this solution was calculated for a rigid vehicle, the airloads are not the correct actual loads at a deformed equilibrium position for the elastic vehicle. This fact provides a way of introducing the *initial perturbation* to start the oscillation, which will be adopted in the present work for all cases where the freestream angle of attack is different from zero.

The structural information necessary for the present analysis consists of some normal mode shapes and their corresponding natural frequencies, the structural damping coefficients associated with each mode, and the vehicle mass distribution or the generalized masses associated with each mode. As previously discussed, we have no actual data for an existing vehicle that matches this configuration. Therefore, the approach followed consisted of estimating the necessary properties from what could be gathered from the literature. For instance, three structural modes were employed in this case, and the chosen mode shapes resemble those presented by Woods and Ericsson [4] .

The theoretical analysis of the numerical stability of the scheme selected for the solution of the aeroelastic equations showed that the scheme is numerically nondissipative. This is a very important issue, because we want to make sure that the numerical scheme is not *stabilizing* physically unstable aeroelastic solutions due to numerical dissipation introduced by the method. The first example here undertakes to address this problem. Essentially, we want to demonstrate numerically what the linear stability analysis already predicted, i. e. , that the numerical method is not introducing any numerical dissipation (or instability) and that a pure sinusoidal response can be captured. In this first case run, therefore, all the structural damping coefficients were set to zero, and a very small value of dynamic pressure was considered. The small dynamic pressure is chosen so as to minimize the damping effect of the airstream. The response, in terms of the generalized modal displacements in the second and third modes, is shown in Figure 5.7 . The results indeed confirm

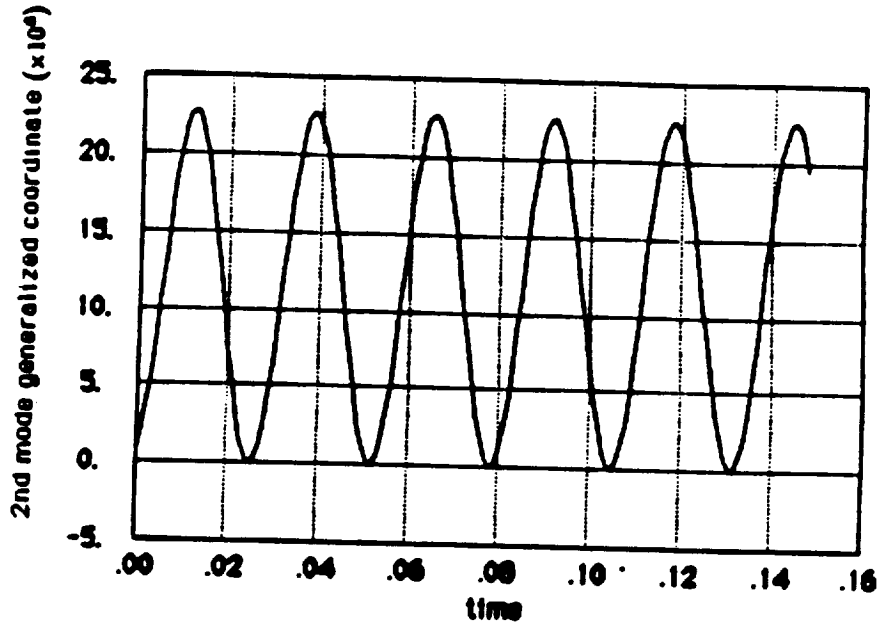


(*a*) 2nd mode response.

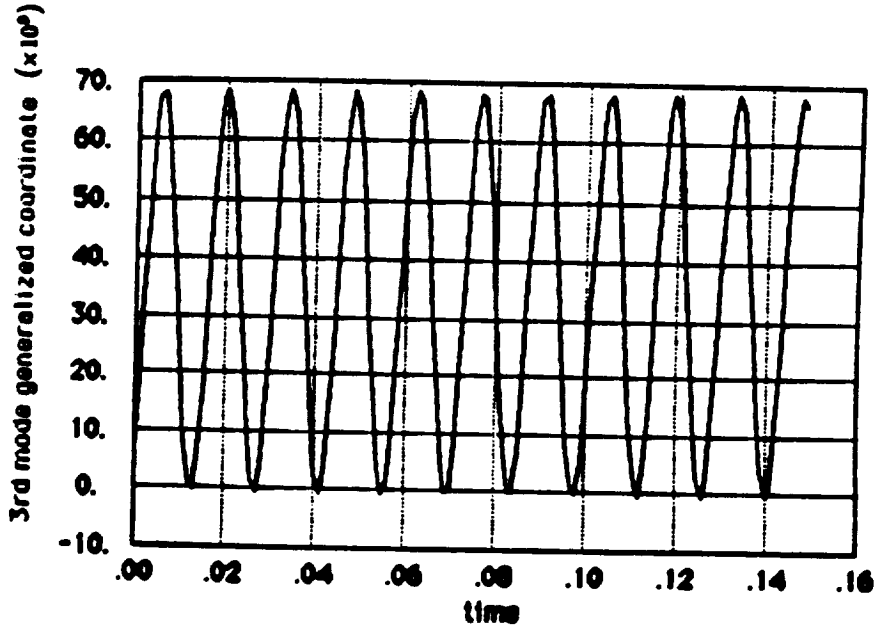


(*b*) 3rd mode response.

Figure 5.7: Response for zero structural damping and very low flight dynamic pressure.

what was expected, since an undamped response is obtained. Although this was the anticipated result, it is important to see that all the complex algorithms developed are able to reproduce such a simple phenomenon.

The other cases analyzed considered more realistic values of dynamic pressure and also some nonzero values of the structural damping coefficients. The procedure followed was to keep the flight Mach number and the angle of attack constants, and vary the dynamic pressure. The structural parameters were, of course, kept constant. For instance the values of structural damping coefficient used were $\zeta_1 = 0.0010$ , $\zeta_2 = 0.0018$ and $\zeta_3 = 0.0036$ , for the first, second and third modes, respectively. A typical vehicle response for an intermediate value of dynamic pressure can be seen in Figure 5.8 , which shows the response in each of the three generalized coordinates. By comparing the magnitudes of the responses for the three modes, it is clear that the overall vehicle response is dominated by the first mode displacements. Figure 5.9 makes this point even more clearly by showing the total deflection at the nose of the vehicle, which can be seen to be composed of the first mode deflection plus a small higher frequency influence.

The usual way in which the influence of the airstream is determined consists of calculating the damping coefficient for the run with the "air on," in other words, for dynamic pressure different from zero, and comparing the rate of decay of the motion with the pure structural damping coefficient. If the former is smaller than the latter, we have a situation where the presence of the flow is destabilizing. Of course, in order to obtain an unstable condition this influence must be large enough to overpower the structural damping and cause the amplification of initial perturbations. As one can see from Figure 5.8, the response in all three modes is damped in this case. The response on the first mode is only slightly damped, the second mode shows a little faster decay, and the third mode decays the fastest. A closer analysis of the damping coefficient reveals that, in this example, the first and second modes are rendered even more stable by the airstream. On the other hand, the damping coefficient for the third mode, at the present dynamic pressure level, is a bit smaller than the structural damping $\zeta_3 = 0.0036$ . One therefore cncludes that the freestream is feeding energy into that mode's oscillation.

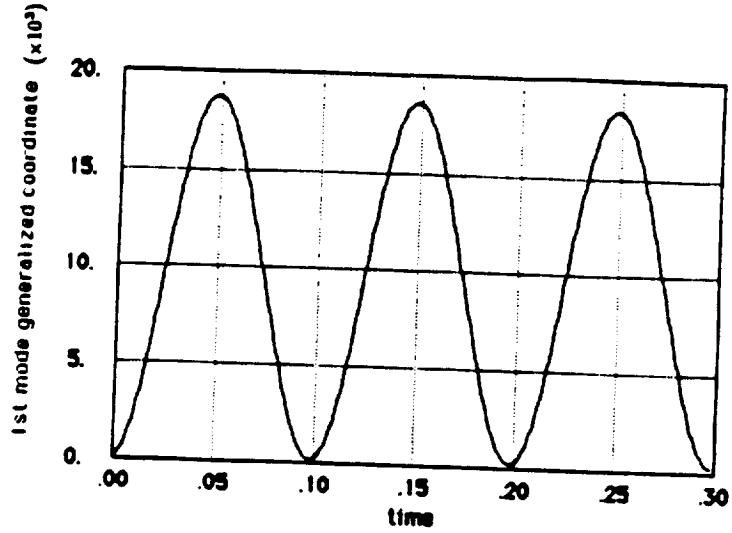


(a) 1st mode response.

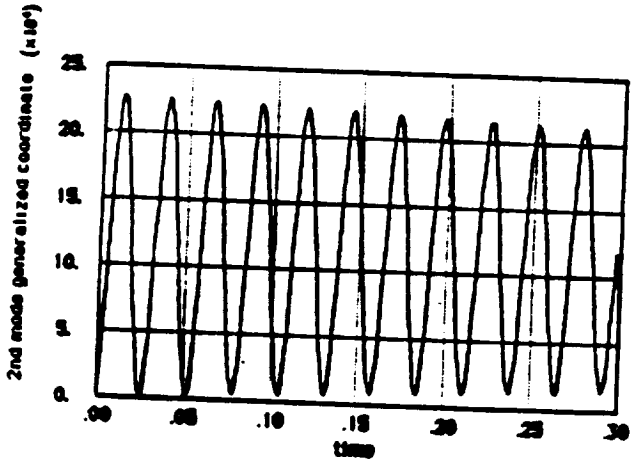


(b) 2nd mode response.

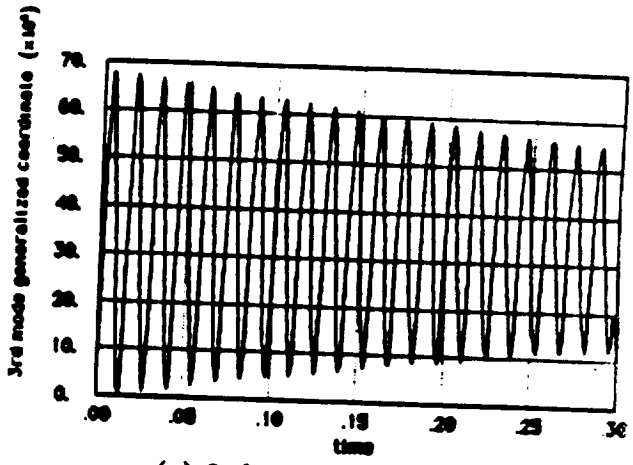


(c) 3rd mode response.

Figure 5.8: Modal response of a general hammerhead configuration at $M_\infty = 0.85$ , $\alpha = 6°$ , and intermediate value of dynamic pressure.

ORIGINAL PAGE IS
OF POOR QUALITY

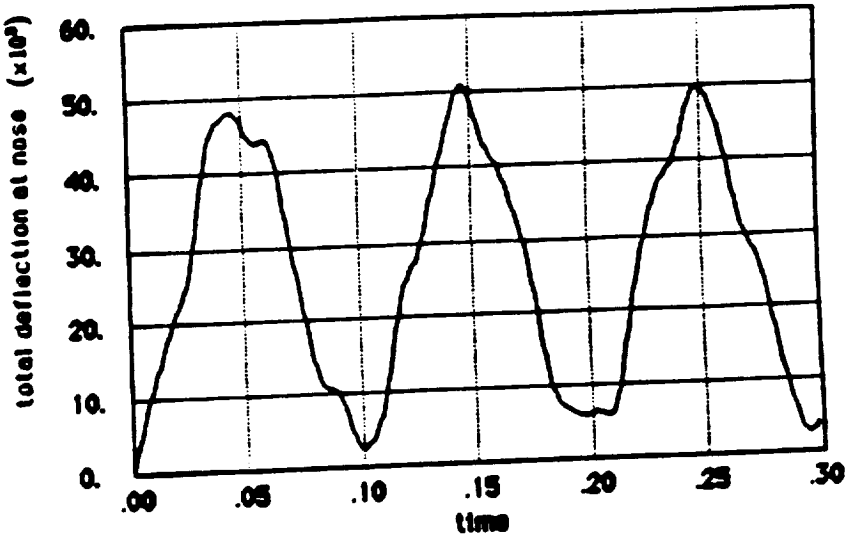


Figure 5.9: Total elastic deflection at the vehicle nose.

Despite the fact that these are time domain analyses, the results are best summarized by a root locus plot, which is shown in Figure 5.10 . In this plot the arrows indicate the direction of increasing dynamic pressure, which was the parameter varied in the analysis. The abscissa is the real part of the aeroelastic root, which is a measure of the rate of the decay of the oscillation in each mode, formed by the product of the damping coefficient at that particular dynamic pressure times the natural frequency for that mode. The ordinate is the imaginary part of the aeroelastic root, which is the frequency of the response of that mode at the dynamic pressure considered. Although one should note that the scales on the two axes are very different, it can be seen from the plot that the frequencies remain approximately unchanged throughout the whole range of dynamic pressures considered.

All the cases analyzed for this hammerhead shape were aeroelastically stable, although all the modes showed an initial tendency of going towards the unstable side for very small values of dynamic pressure. This tendency was quickly reversed as the dynamic pressure was increased further, such that it was hard to detect any of this behavior from the time plot for the first and second modes. For the third mode, however, the reversal of damping at low freestream dynamic pressure

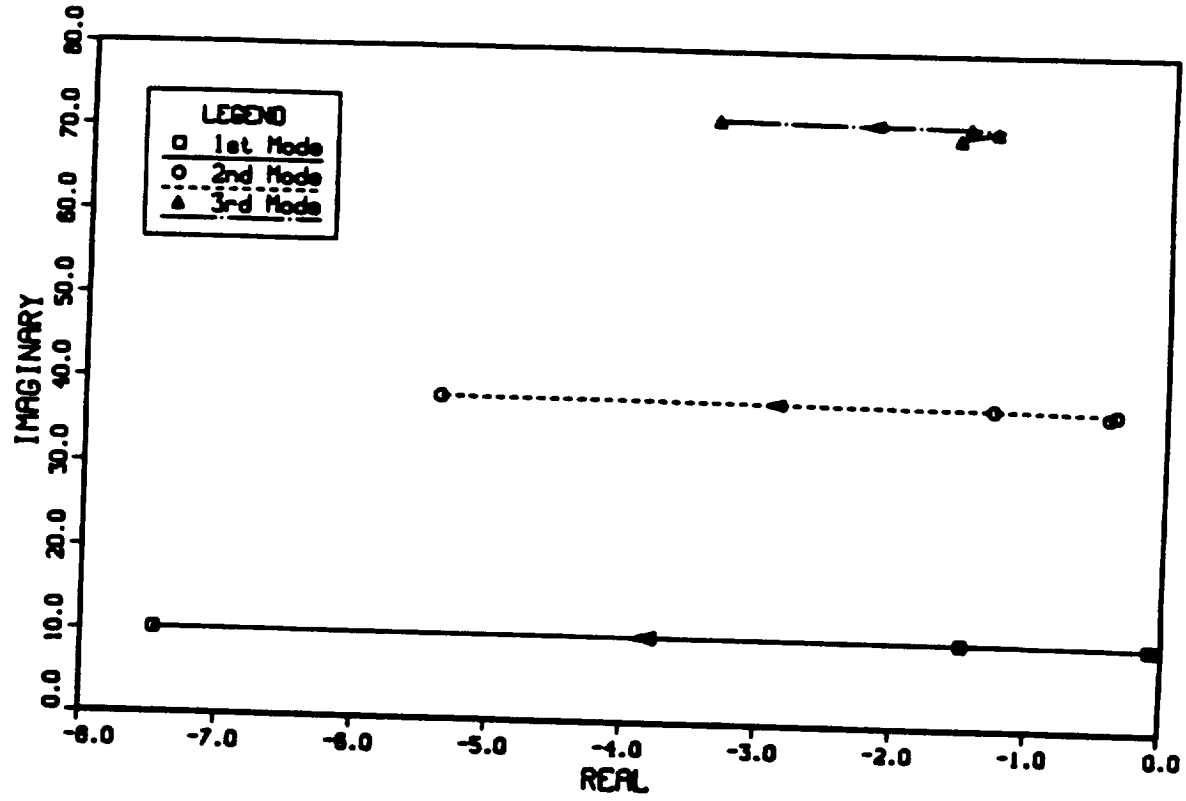


Figure 5.10: Aeroelastic root loci for general hammerhead configuration at $M_\infty = 0.85$ and $\alpha = 6°$ . The parameter varied is flight dynamic pressure.

is clearly visible from Figure 5.10 . After this initial trend was passed, what we will call a *pure damping* behavior, for the lack of a better description, was observed. It is characterized by a simple increase of the damping in each mode as the flight dynamic pressure is raised. The frequencies remain approximately unchanged. This is not typical aeroelastic behavior for conventional flight vehicle configurations with wings and tails. However, it should be noted that the natural frequencies considered for this analysis are quite high, which means that we are probably assigning stiffness values that are higher than they should be and explains why no flutter is observed. Moreover, as already mentioned, this configuration does not correspond to any existing vehicle. It is, therefore, very difficult to try to correlate these results with some expected behavior.

Finally, the issue of the computational costs of these aeroelastic solutions should be considered. For the $105 \times 66 \times 38$ grid which was used here, each aeroelastic iteration takes about 12 CPU seconds in a CDC Cyber 205. This represents an increase of 20% over the CPU time per iteration for steady state aerodynamic calculations. Almost all the additional time is spent in regenerating the computational grid once a new body deflected position is determined from the solution of the structural-dynamic equations.

One does not necessarily have to regenerate the complete grid at every time step, but some form of reshaping is required in order to account for the deformation of the body. Some authors, see for instance Steger and Bailey [31], prefer to use some form of shearing transformations to account for the grid deformation, and avoid solving the grid generation equations at every time step. In the present approach, since an algebraic grid generation scheme is being used, we regenerate the whole grid. The grid points on the body surface keep their relative position with respect to the body centerline at every axial station, and the far field boundary is kept fixed. The remainder of the grid, which is all the interior part of the grid, is interpolated between those ends using the same algorithm that initially created the whole grid. Note that the structural-dynamic equations are solving for the deformation of the body centerline, which means that most of the grid displacement is going to occur close to the body. This is consistent with what is physically happening, in the sense

that the body motion should cause perturbations close to itself and the far field should remain undisturbed.

The amount of time consumed by the solution of the structural-dynamic equations is truly negligible when compared to the overall CPU time. The point that should be considered, though, is that modal analysis is being used. As previously mentioned, this is a very powerful technique since a whole range of effects can be considered. However, one may want to replace the modal superposition approach by, for example, a finite element representation of the vehicle. In such a case, the amount of time required for the structural-dynamic solution is bound to increase considerably.

The overall system time per iteration for aeroelastic analysis, however, suffers much more than the CPU time when compared to a pure steady state aerodynamic solution. As discussed in the previous section, the major difficulty arises from the fact that the database is not core contained. In this case, since the grid is recalculated at every iteration, so are the metrics of the transformation. Essentially we are doubling the amount of I/O per iteration, since now we have to output the metrics as they are calculated and then read them back as we operate in each direction. Although asynchronous I/O is still being used, the performance of the code is lowered, and in this case the ratio of CPU time to overall system time is only around 30%. This means that, 70% of the time the job is running, it is simply doing input/output. Of course, those kinds of statistics are very machine dependent, and all of this is true for the CDC Cyber 205 . Ideally, one would like to avoid all this I/O. For the size of problem we are dealing with here this could certainly be accomplished by using a computer such as the Cray 2 . Nevertheless, all the effort spent in making the algorithm suitable even for "smaller" computers is important, because shows that the method could be used even by those without access to a system of the size of the Cray 2.

# Chapter 6

# Analysis of an Atlas-Able IV Configuration

## 6.1 Initial Considerations

As previously mentioned, in the early 1960's some aeroelastic problems were observed on launch vehicles with hammerhead payload configurations when passing through the transonic regime. One of those configurations was the Atlas-Able IV, in which case the problems observed in flight were later traced back to something resembling flutter. The mechanism driving the instability was associated with the lags in the aerodynamic forces caused by phenomena induced by the hammerhead, which would cause the airstream to do positive work on the oscillating vehicle.

The ideal case to study here would be one where both steady aerodynamic data and detailed aeroelastic results were available. Unfortunately, this is certainly a difficult combination to find in the literature. At the time, the Atlas-Able IV configuration represented the best test case we could find, despite the fact that aeroelastic information is somewhat limited. Geometrical data for this configuration are available, at least in nondimensional form*, and steady aerodynamic pressure distributions from wind tunnel tests are also published[75]. The structural data, however, are rather sketchy because part of this information is still classified*.

* Ericsson, L.E., personal communication, April 1987.

For instance, exact values for frequencies, structural damping coefficients, and vehicle mass distribution were not accessible from the same sources that provided geometrical and steady aerodynamic data.

In the present work, the approximate range of frequencies to be considered, the approximate form of mode shapes, and an estimate of reasonable structural damping coefficients were obtained from Woods and Ericsson [4], and Ericsson *. The mass distribution was estimated from data available for Atlas boosters and provided by Gen. Dynamics. Steady aerodynamic wind tunnel data, which was used to validate the initial aerodynamic solution, was available from Graham and Butler[75] .

Other steady and unsteady aerodynamic data were found in the literature for similar hammerhead configurations. For instance, Coe[76] presents the steady and unsteady aerodynamic pressures on an Able V payload model, and Robinson *et al.*[77] study the dynamic response of some hammerhead models to unsteady aerodynamic loading. However, the Atlas-Able IV data still constitute the best information and allow for a better comparison of results. Finally, it should be mentioned that a very complete set of structural and aeroelastic parameters on two Titan/Centaur models was made available to the author by Henning +. Unfortunately, because of time limitations and the high computational costs of these aeroelastic solutions, it was not possible to perform aeroelastic simulations for these cases.

As we have done in the previous cases studied in this work, the computational grid for the Atlas-Able IV configuration was generated using algebraic methods. A three dimensional view of the body and grid in this case can be seen in Figure 6.1 . The grid has 105 points in the longitudinal direction, 66 points in the normal direction, and 38 points in the circumferential direction which again is a periodic type mesh going 360° around the body. In this case, the body is composed of a ellipsoidal nose, a cylindrical forebody section, a boattail, and the cylindrical afterbody section. The ratio between minor and major axes of the ellipse is approximately 0.605 . The reference length adopted in this case is the diameter of the cylindrical afterbody section, and the diameter of the cylindrical forebody section is 1.5 reference lengths.

A typical complete longitudinal plane of the grid is shown in Figure 6.2($a$) , and

* Ericsson, L.E., personal communication, April 1987.

\+ Henning, T., personal communication, May 1987.

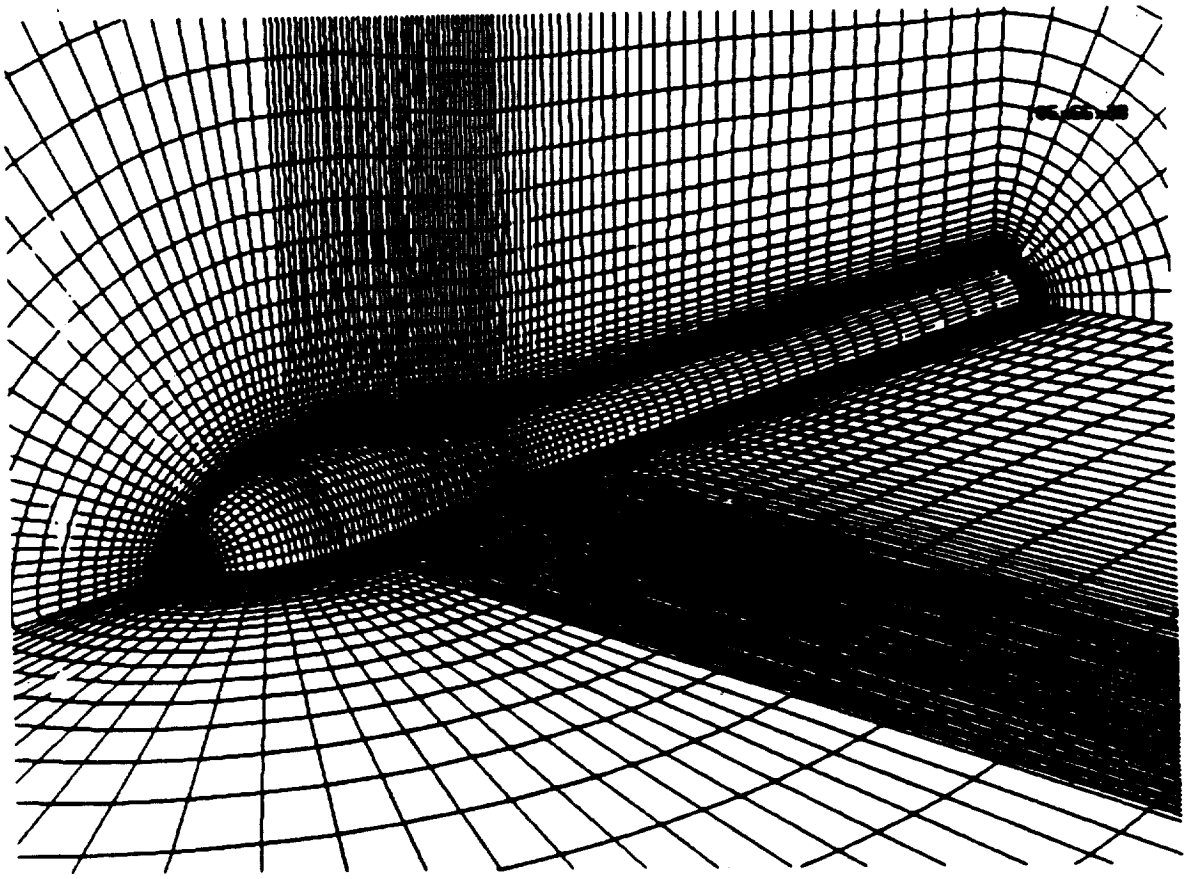

Figure 6.1: Three dimensional view of Atlas-Able IV configuration grid system.

details of the nose and the boattail regions can be seen in Figures 6.2($b$) and ($c$) , respectively. In the longitudinal direction, 29 points are used in the nose region, 12 in the cylindrical forebody region, 27 in the boattail, and 37 in the cylindrical afterbody region. One parameter hyperbolic grid stretching[56] techniques are used in the ellipsoidal nose region to cluster grid points towards the upstream centerline and towards the ellipsoid-cylinder intersection. An equally spaced grid is used over both the forebody cylinder and boattail sections, and a 6.98% exponential grid stretching is used in the cylindrical forebody section in order to gradually coarsen the grid as we move towards the downstream boundary.

The normal direction (or $\eta$-direction) would again be more properly called a nearly normal direction, since $\eta$-lines do not intersect the body surface at exactly right angles on the nose and boattail regions. Since these lines meet the body at angles that are very close to 90° , we will accept the small error being introduced by this simplification, as already discussed in the previous chapter. To ensure proper capturing of viscous effects in the normal direction, a 16% exponential grid stretching was used everywhere in this direction in order to cluster grid points close to the body.

## 6.2 Configuration at Angle of Attack: Steady State Results

The initial aerodynamic solution involving the Atlas-Able IV was calculated for a $M_\infty = 0.85$ and $\alpha = 6°$ flight condition. The Reynolds number considered was $Re = 1.2637 \times 10^6$ , based in the reference diameter. It should be mentioned that this number was chosen to match Graham and Butler's experimental conditions[75] . The boundary layer was considered turbulent for most of the calculations performed here. Starting from freestream everywhere and imposing the appropriate boundary conditions, we allow the flow to evolve to a converged solution.

A side view of the pressure coefficient, Mach number, and density contour plots around the body for the converged solution can be seen in Figure 6.3 . These plots

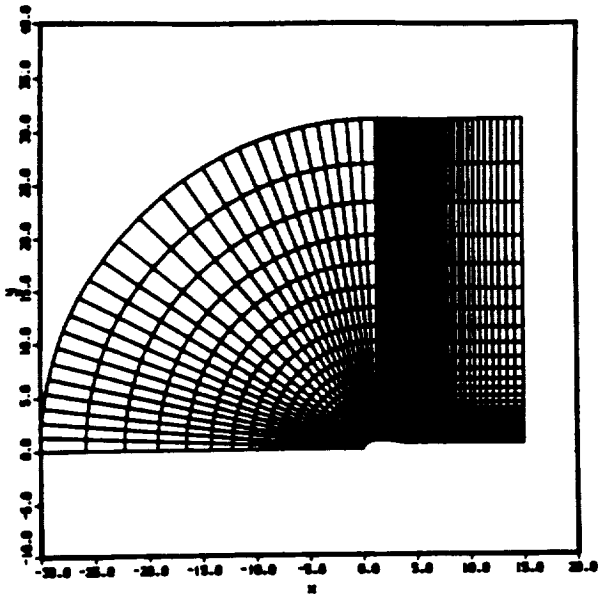

(*a*) Complete plane.

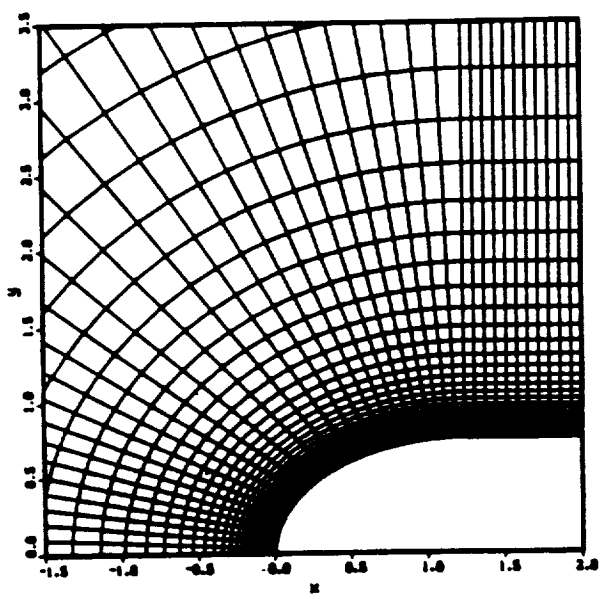

(*b*) Detail of nose region.

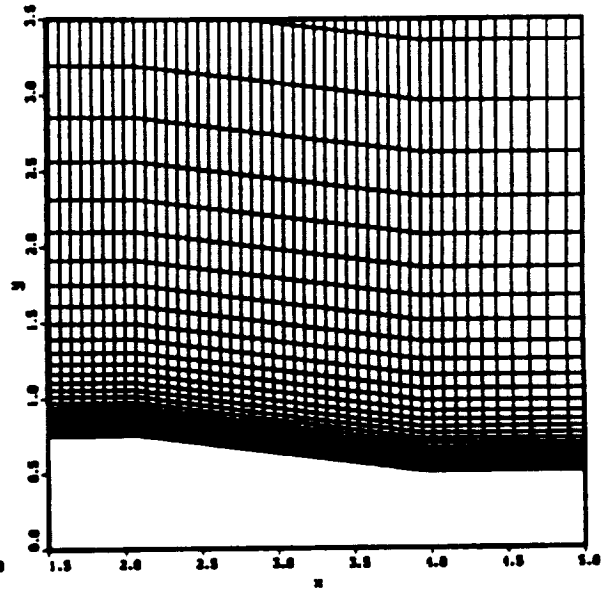

(*c*) Detail of boattail region.

Figure 6.2: Typical longitudinal grid plane for Atlas-Able IV configuration.

ORIGINAL PAGE IS
OF POOR QUALITY

ORIGINAL PAGE IS
OF POOR QUALITY



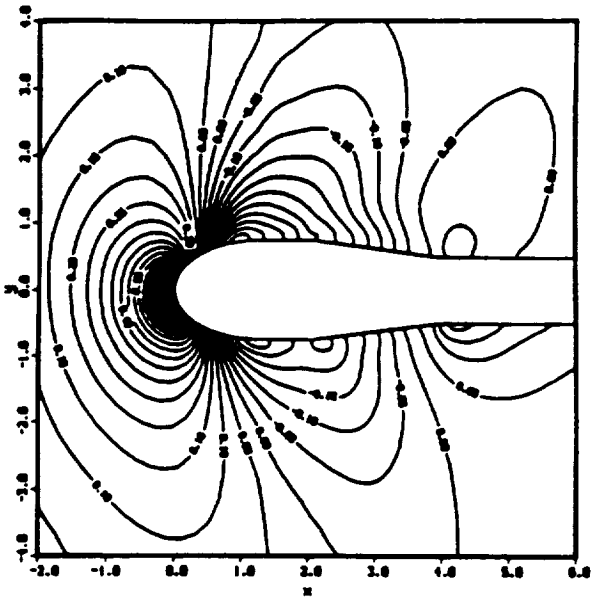

(a) Pressure coefficient contours.

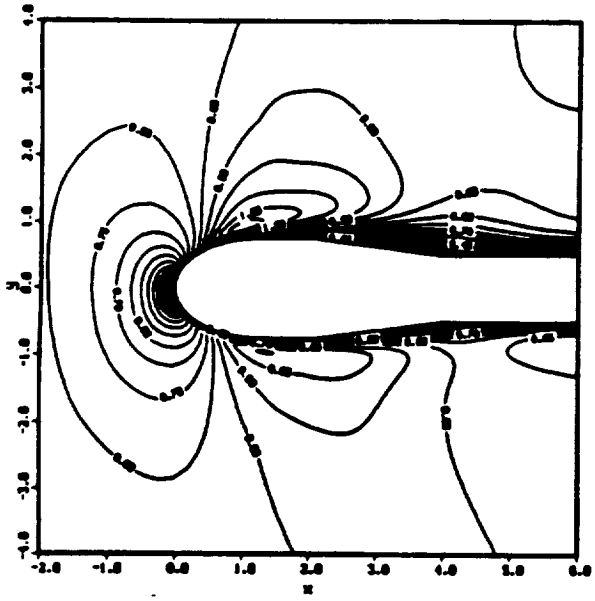

(b) Mach number contours.

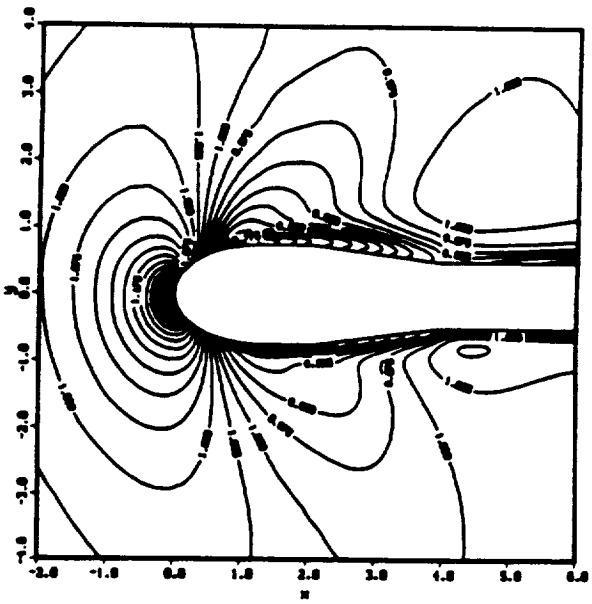

(c) Density contours.

Figure 6.3: Flow solution about an Atlas-Able IV configuration at $M_\infty = 0.85$ and $\alpha = 6°$ (side view).

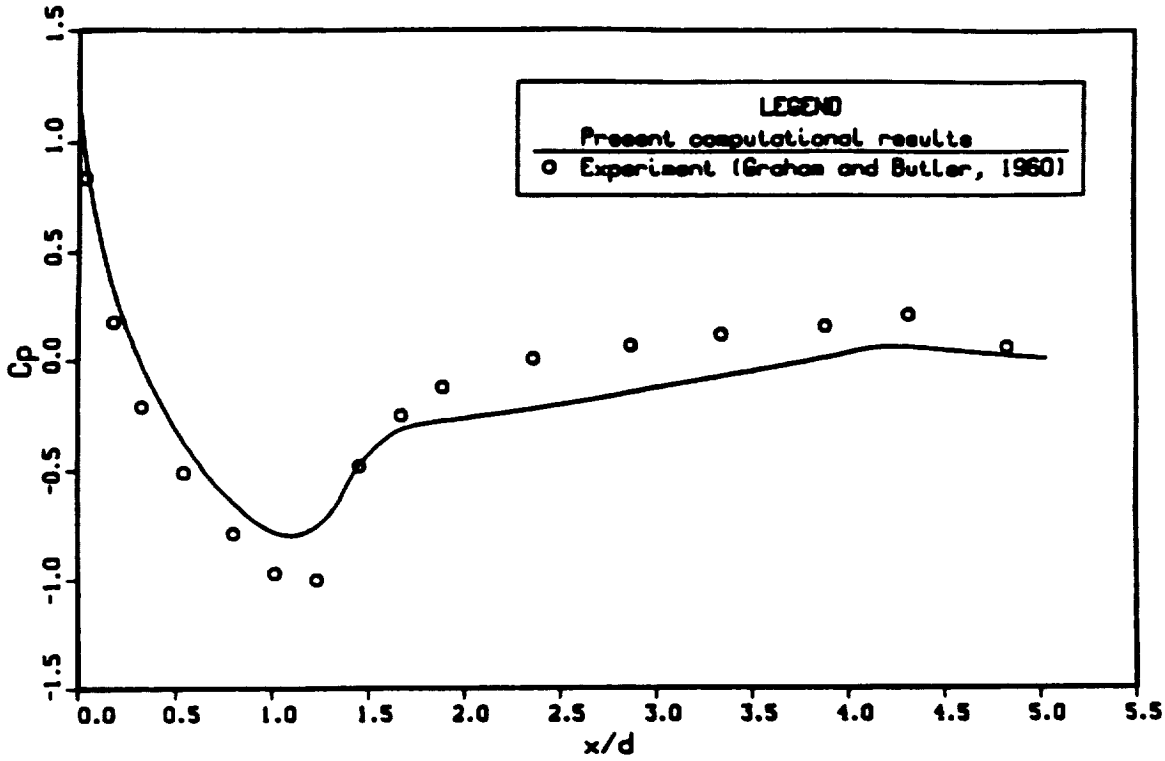


Figure 6.4: Pressure coefficient distribution on the leeside of an Atlas-Able IV payload ($M_\infty = 0.85$ , $\alpha = 6°$).

give a good idea of the overall flowfield appearance, despite the fact that we are only seeing leeward and windward planes. The Mach number contours seem to indicate a sizable separated region on the leeside, which is evidenced by the *bubble* sort of behavior of the contours over the forebody cylinder and boattail regions, where the local velocity magnitude (or Mach number) increases, then decreases back to zero, and finally increases again up to the freestream condition as we move outwards from the body towards the farfield. This is very typical of reversed flow regions, and it will be investigated in more detail later when discussing particle trace results.

Taking advantage of the fact that for this configuration there are experimental results available, Figure 6.4 shows a comparison of the computed pressure coefficient distribution on the leeside of the body with wind-tunnel measurements by Graham and Butler[75]. It can be seen that the calculated $Cp$ distribution follows the trend

of the experimental results well, but the strength of the shock is not being accurately captured by the computation. The location of the shock seems to be correct, but apparently the flow does not expand as much as the experiment indicates it should. The result is a weaker shock. It is clear that the computational shock is spread over a few grid points, which is typical of centrally differenced finite difference schemes.

The computations indicate that the flow separates right after the shock, which is also in agreement with the Schlieren photographs available from Reference[75] for this flight condition. As for the pressure coefficient distributions, the separated region is evidenced by the somewhat flat $Cp$ distribution. The success of the present computation of numerical values of $Cp$ over the separated region is also less than perfect, although the computations capture the correct trends in the $Cp$ distribution. It must be pointed out that there is a small difference in the length of the boattail region between the geometry provided by Ericsson [4] * and the one provided by Graham and Butler [75] . The latter has a slightly shorter forebody cylinder section and, consequently, a slightly longer boattail section such that the overall payload length is the same. This makes the $Cp$ comparisons over the boattail section less reliable, but due to the problems regarding the shock strength it would be difficult, in any event, to compare results downstream of the shock. The problem is compounded by the fact that in the separated region the uncertainty about turbulence modelling becomes even more important, and this may be affecting the results.

A comparison of the pressure coefficient distributions on the body for other longitudinal planes can be seen in Figure 6.5 , which shows $Cp$ values over the lateral and windside planes. Essentially, the same observations made with respect to the leeside results are true for these other planes too. The computed pressure coefficients follow the trend of the experimental results, but they are slightly underexpanded over the ellipsoidal nose-forebody cylinder intersection. A new feature that can be observed on these latter results is that there is a noticeable tendency of forming a second dip on the $Cp$ curves around the forebody cylinder-boattail intersection. The reason for that is quite clear, since it is reasonable to expect the separation to be less severe on the side of the vehicle, or on its windside, than it is on the leeside.

* Ericsson, L.E., personal communication, April 1987.

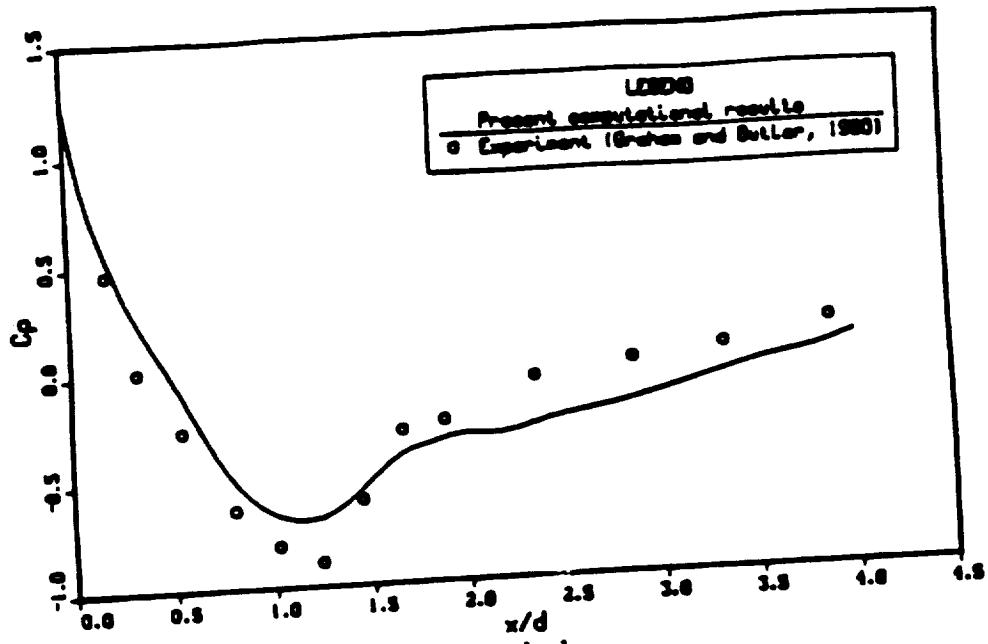


(a) Lateral plane.

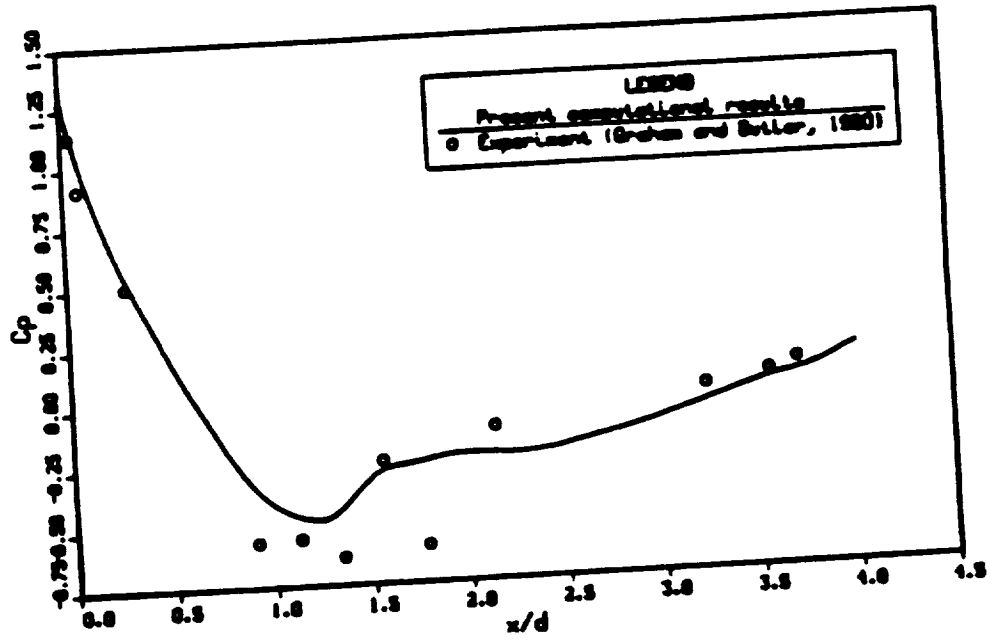


(b) Windside.

Figure 6.5: Pressure coefficient distributions for an Atlas-Able IV configuration ($M_\infty = 0.85$ , $\alpha = 6°$).

ORIGINAL PAGE IS
OF POOR QUALITY

This second dip is merely a result of the flow reaction due to the expansion corner over the forebody cylinder-boattail intersection. The experimental results for the windward plane exhibit what seems to be some data scatter, as one can see from Figure 6.5($b$) . Reference[75] offers no explanation for its existence. Our calculations do not reproduce any of this behavior, and the calculated $Cp$ distribution follows the experimental curve that would be obtained if the scattered points were neglected.

Finally, it is important to stress that the comparisons were made between the computational results and the experimental ones at the same nominal tunnel Mach number. In other words, there was no attempt to try to correct for the tunnel blockage effect, which cause the effective Mach number in the tunnel to be different from the nominal one. Usually one tries to match the vehicle lift coefficient instead of matching the nominal tunnel parameters. This was not done in this case, and it may be one of the causes of the discrepancies observed in the $Cp$ results. There were some numerical difficulties, mainly associated with artificial dissipation parameters, which can also explain part of the discrepancies observed in the results. We would prefer, though, to postpone the discussion of these purely numerical problems until the next section.

A good pictorial description of the flow topology can be seen from Figure 6.6 , which shows side and top views of oil-flow lines for the Atlas-Able IV configuration at this flight condition. One can see that the flow separates almost at the ellipsoidal nose-forebody cylinder intersection on the leeside. The line of separation extends all the way down to the windside where the flow separates somewhere just downstream of the forebody cylinder-boattail intersection. In order to help the understanding of these figures, it is worth mentioning that, since oil-flow lines are generated by restricting particle traces to the second plane above the body surface, lines of separation are evidenced by thicker lines where particle traces converge to it. On the other hand, lines of reattachment are shown by *empty spaces*, where all traces go away from it. The figure also shows that the boattail is completely immersed in a region of reversed flow, and that the flow reattaches somewhere downstream of the boattail.

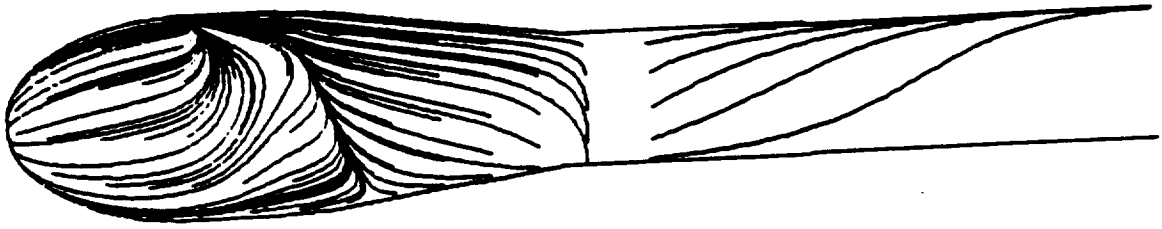

(*a*) Side view.

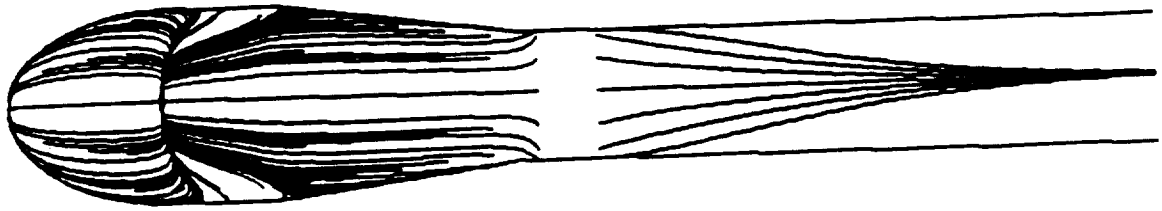

(*b*) Top view.

Figure 6.6: Oil-flow lines for Atlas-Able IV configuration at $M_\infty = 0.85$ and $\alpha = 6°$.

Unrestricted particle traces are shown in Figure 6.7 for some different viewpoints, which help visualize and understand the overall flow topology in this example. Figure 6.8 shows an expanded view of the particles *taking off* from the body surface around the lee generator region. It is clear from these figures that in this case we have a very extensive region of reversed flow, and of course flow separation. Figure 6.9 complements this picture by showing velocity profiles on the lee and windsides over the regions of reversed flow on the body, where we can see how far the reversed velocities penetrate into the flowfield. This information reassures us of our interpretation of the Mach number contours presented in Figure 6.3 , which have been previously discussed. It also makes it evident that even on the windside there is a region of separated flow for this flight condition. Finally, Figure 6.10 shows a front view of the vehicle, with particle traces indicating that the solution is indeed symmetric with respect to the pitch plane in this case, which confirms statements previously made.

It is very important to realize the difference between the flow solution obtained for the present configuration and the one for the configuration studied in Chapter 5 . Although the present configuration is a somewhat more slender one, the extent of the flow separation region in the present case is much larger than on the previous case. It is the author's belief that such behavior is mainly associated with the length of the forebody cylinder region. This region is short in the present configuration, which allows for the merging of the distinct separation regions observed in the configuration of the previous chapter. In other words, the separation caused by the shock, which usually is located right after the nose region at least on the leeside, merges with the flow separation due to the adverse pressure gradients on the boattail. This creates a very extensive separated region, which explains the kind of flow topology observed in this case. Moreover, the shorter forebody also produces more severe adverse gradients, which again contribute to extend the separated region. The existence of such extensive flow separation raises questions with respect to the aeroelastic stability of the configuration, besides being a source of conce with respect to buffeting loads.

Since the grid size used in the present investigation is the same as in the case

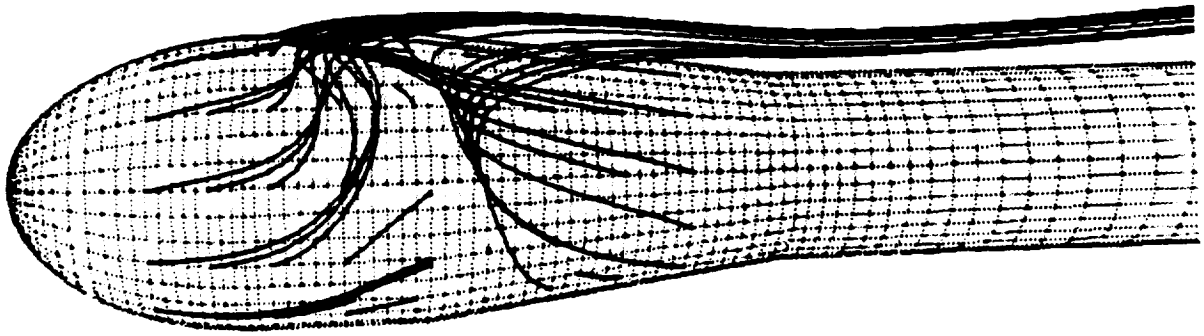

(*a*) Side view.

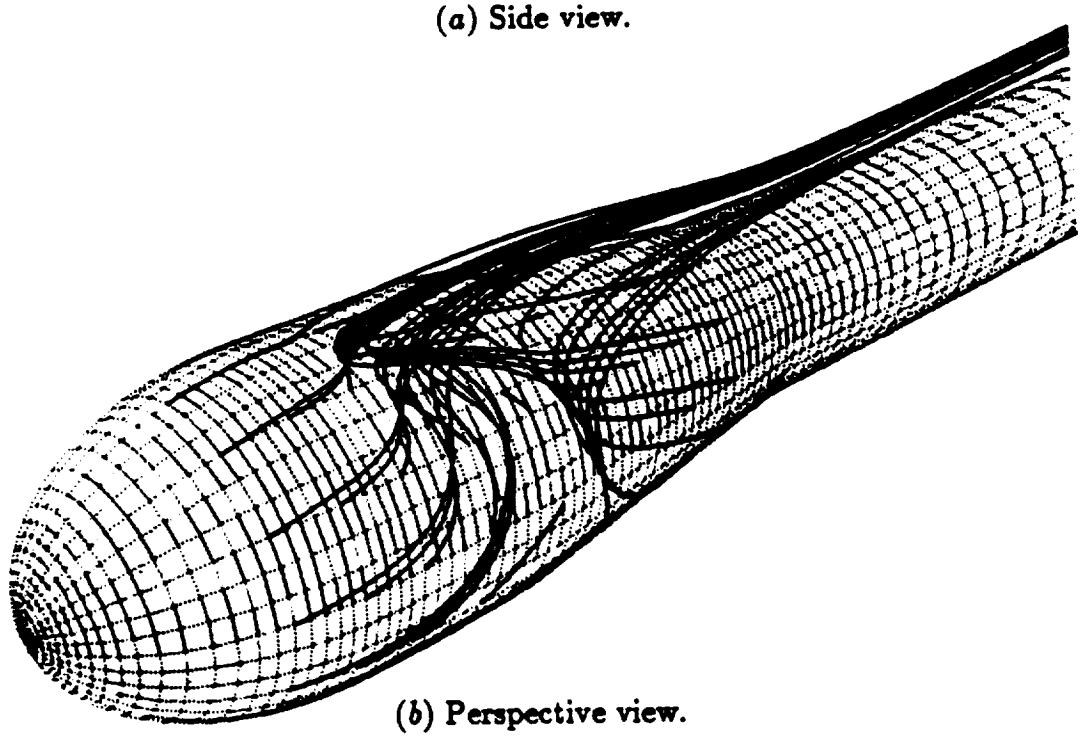

(*b*) Perspective view.

Figure 6.7: Particle traces showing flow separation on the Atlas-Able IV configuration at angle of attack.

ORIGINAL PAGE IS
OF POOR QUALITY

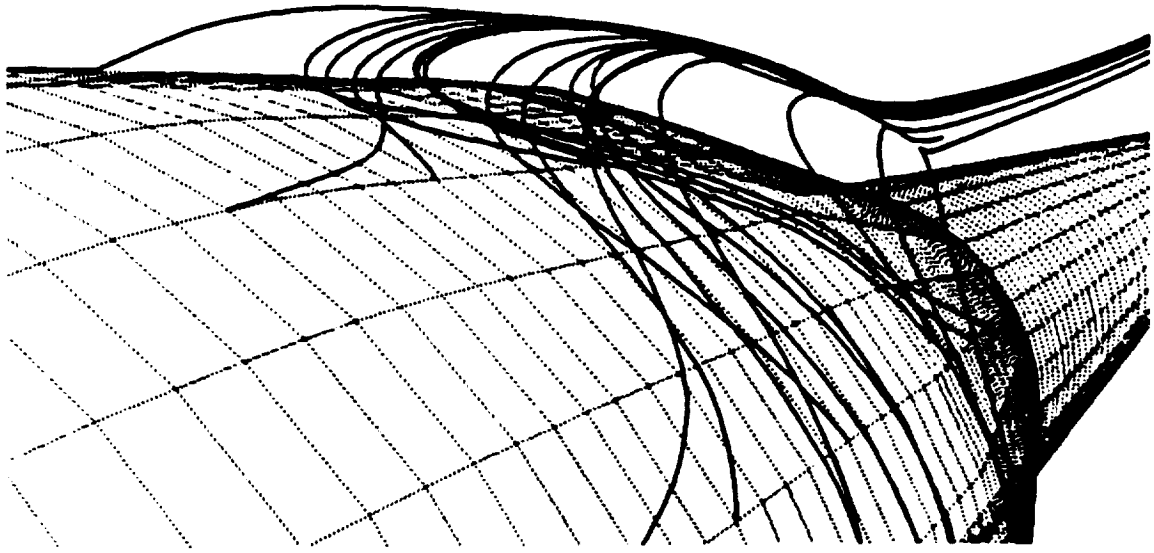

**Figure 6.8: Expanded view of flow separation close to the leeside.**

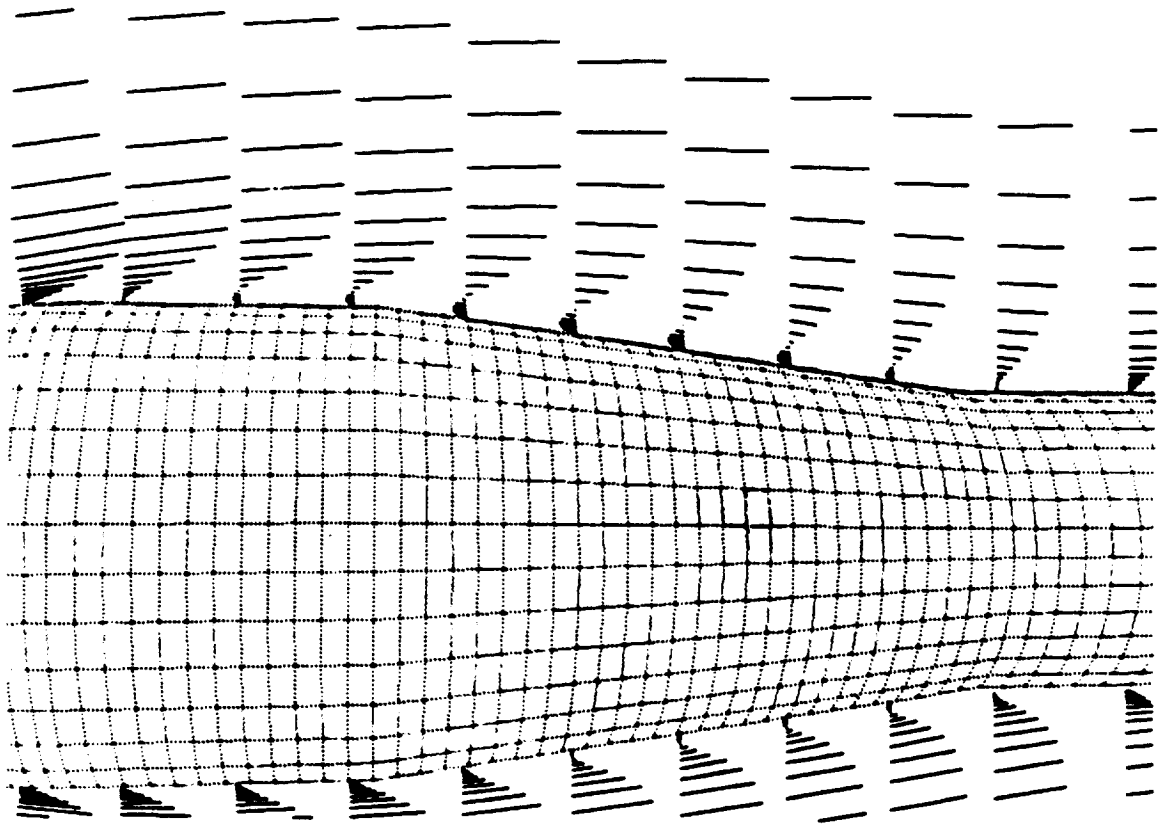

Figure 6.9: Velocity profiles on Atlas-Able IV configuration at $M_\infty = 0.85$ and $\alpha = 6°$ (side view).

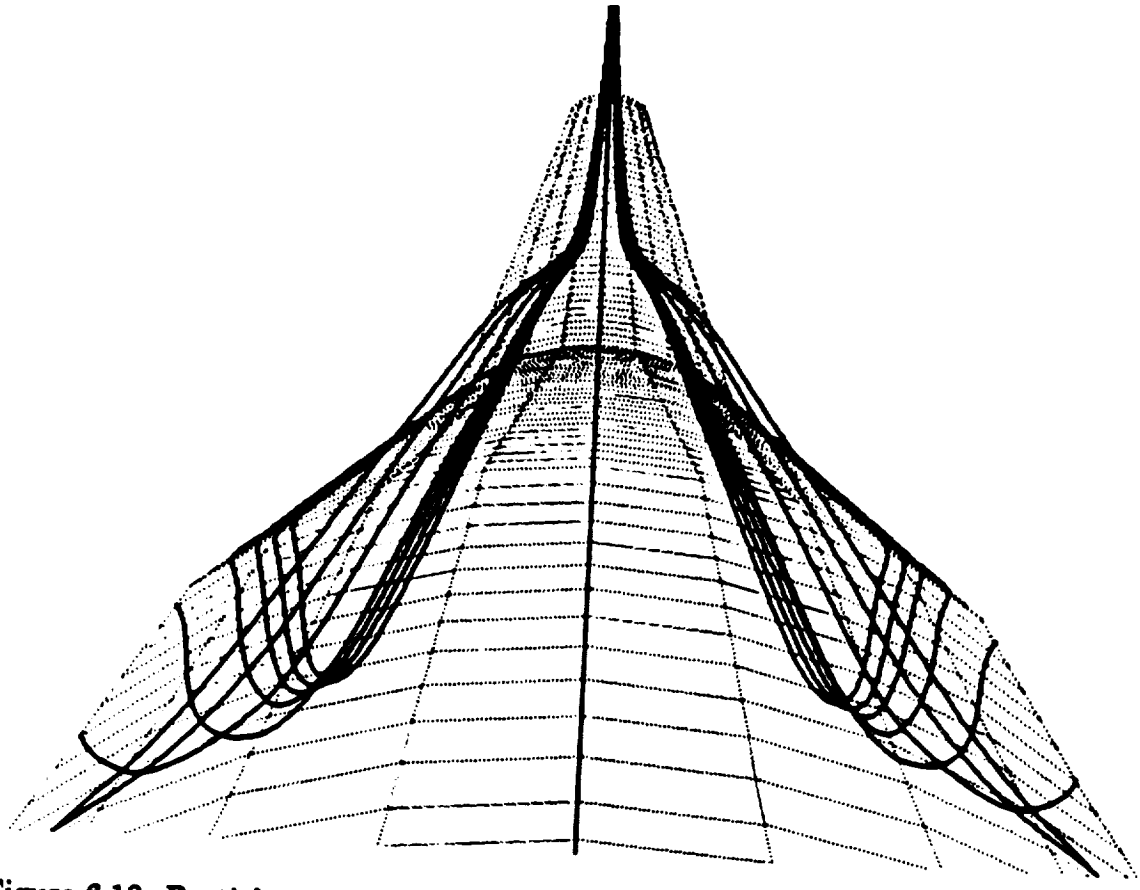

Figure 6.10: Particle traces seen from the front of the vehicle showing symmetry of the solution with respect to the pitch plane.

studied in the previous chapter, i. e. , a $105 \times 66 \times 38$ point grid, the computational statistics are essentially the same as on the previous case at least as far as steady state calculations are concerned. For a CDC Cyber 205 computer, each iteration takes approximately 10 CPU seconds, and somewhere around 3500 to 4000 time steps (iterations) are required to achieve a converged solution. The CPU time represents approximately 60% of the overall system time, and the remainder of the time is spent in I/O because the database is not core contained.

## 6.3 Some Computational Difficulties

This section discusses some of the difficulties encountered in the computation of the aerodynamic flows studied here. It should be noted that we will be talking about steady state calculations in the present section, since most of the validation of the purely aerodynamic computational method was done for steady state cases. It is also important to realize that, since the use of superposition in a modal form has been certainly proved for aeroelastic analysis, the major concern in the present work is to show that the computational techniques proposed here are capable of reproducing the correct aerodynamic phenomena necessary for the aeroelastic analysis. For this reason, it is very important to study these initial aerodynamic solutions, or steady state solutions, to ensure that the physical flow phenomena are being adequately captured.

We have seen in the previous section that the code is doing a less than perfect job in terms of capturing the shock strength. One of the possible explanations for this kind of difficulty is associated with the amount of artificial dissipation being used in the calculation. As discussed before, for central difference schemes it is necessary to introduce some form of numerical dissipation in order to control the nonlinear instabilities associated with the aliasing back into the lower frequency range of the high frequency phenomena that is not supported by the mesh. The question is, then, how much artificial dissipation should be added.

The approach followed in this work consisted of adding the minimum amount of artificial dissipation that would still ensure numerical stability of the solution

process. This *minimum amount* was determined by numerical experiments. When one starts from freestream and tries to march the solution in time up to a steady state condition, the time steps that have to be taken in the beginning of this process are very small. One way to speed up the convergence to steady state is to take larger time steps and simultaneously use unrealistically high values of artificial dissipation in order to keep the solution numerically stable. As the flow solution approaches the correct steady state condition, the numerical dissipation can be reduced to more appropriate levels where it should not interfere with the physics of the computation.

The problem observed in the present work was that the amounts of artificial dissipation necessary to keep the numerical stability of the solution process were almost one order of magnitude higher than what is recognized in the literature * as the appropriate level for these computations. One possible consequence of this use of excessive amounts of artificial dissipation is that the shock might have been *dissipated* by them. This can be another factor explaining the features observed in our computational results with regard to the transonic shock capturing, where the flow does not expand as much as the experimental results indicate it should, and consequently the shock strength is not correct.

It should be mentioned that the artificial dissipation scheme implemented in the present code is what can be called a *constant coefficient* artificial dissipation algorithm. This means that a constant value of artificial dissipation coefficient is used throughout the computational domain. More recent flow solver algorithms, still using central differences, have more elaborate artificial dissipation algorithms, usually weighting the artificial dissipation coefficient with the local norm of the residue. The latter seems to produce better results, but unfortunately we did not have the opportunity to implement it in the calculations performed here.

Another subject that presented considerable concern in the present work was the issue of turbulence modelling. It is understandable that this should be true, since the models are of an empirical nature. As we have mentioned before, the two layer Baldwin and Lomax[46] algebraic eddy viscosity model was used for the present computations. This model was originally derived for attached or mildly separated boundary layers. The results in the previous section indicate that a rather massive

* Pulliam, T.H., personal communication, October 1987.

flow separation condition is being observed in this case.

Actually, the problem becomes more complex by the fact that some small variations in the model computational parameters can cause dramatic changes in the flow topology. The parameter varied in the present work was the distance, in terms of computational grid points, from the body wall that we search for the maximum velocity in the profile, which is an important parameter in the present model implementation. In the results presented in the previous section, this search is done up to the 25th grid point in the normal direction. This was the value of this parameter (called *edgek* in the present work) that seems to produce most realistic results in terms of the flow topology. For values of *edgek* smaller than 25, the separation region is even larger, and for values larger than 25 the flow shows a tendency to remain attached over larger portions of the body.

Figure 6.11 shows oil-flow lines for a solution obtained using *edgek* equal to 20 , i. e. , the search for the maximum velocity in the boundary layer profile is done up to the 20th grid point. The freestream parameters are the same as before, $M_\infty = 0.85$ and $\alpha = 6°$ . In this case there is a well defined *focus*[71] on the side of the body. Even ahead of the ellipsoid-cylinder intersection on the lee generator there is a saddle point of separation, whereas on the solution presented in the previous section a nodal point was observed in the corresponding position. The release of particles around the focal point, as identified from Figure 6.11 , produces the particle traces plot shown in Figure 6.12 . This figure shows how the particles are caught in the reversed flow region and convected upstream before reaching the forward flowing stream region. Details of the vortex *taking off* from the body surface can be seen in Figure 6.13 , for the same particle trace plot shown in the previous figure.

It is clear from these figures that the topological structures observed in this case are very different from those observed on the results presented in the previous section. Moreover, the region of separated flow in the present case is larger than in the previous one. Although the flow reattaches just downstream of the boattail, as before, the separation occurs further upstream when compared to the previous case. In this case not only the boattail, but also most of the forebody cylindrical section are immersed in a reversed flow condition. Finally, it should be mentioned

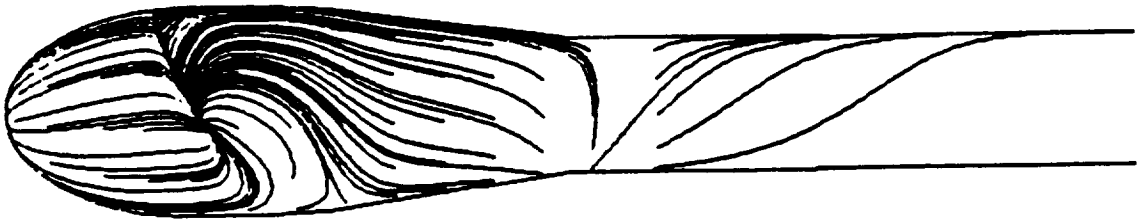

(*a*) Side view.

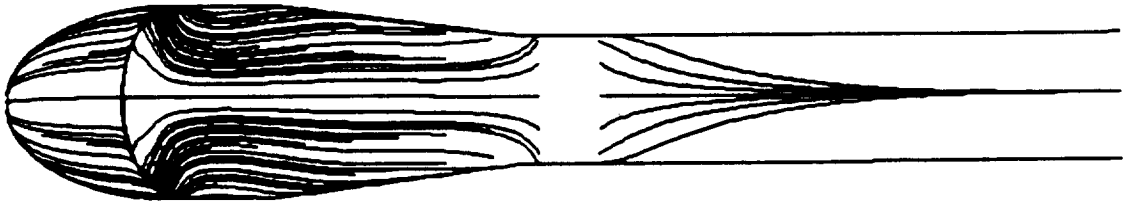

(*b*) Top view.

Figure 6.11: Oil-flow lines for computation with search up to 20th grid point.

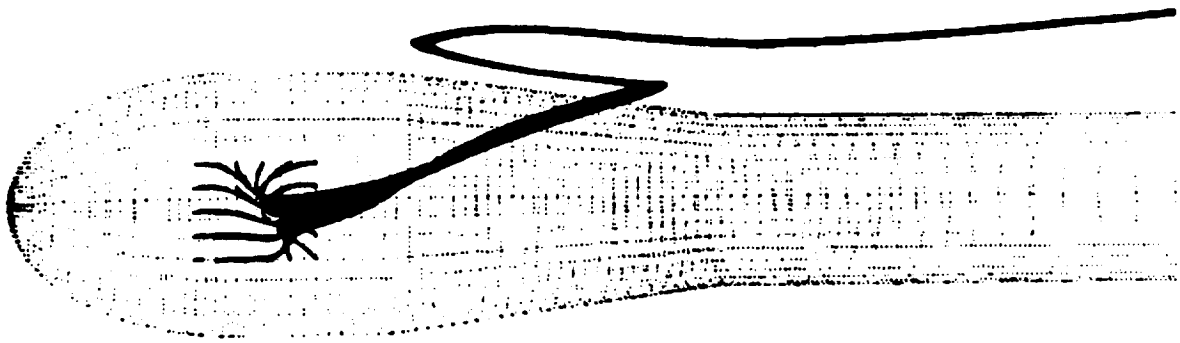

Figure 6.12: Side view of traces for particles released around the focal point on the side of the body.

that, even with such dramatic flow separation, the solution is still symmetric with respect to the pitch plane, as before.

We turn our attention to the cases when the parameter is varied in the other direction. Figure 6.14 shows a side view of the oil-flow lines for the solution obtained when the search for the maximum velocity in the boundary layer profile is performed up to the 35th grid point. The flow on the forebody cylindrical section is fully attached in this case, and the separation region is limited to the *upper* portion of the boattail region. In terms of flow separation structure, the swirling of the flow around the focal point on the boattail is evident from the figure. It is clear from this figure that the flow on the windside never really separates, which is also in contrast with the results previously shown for this configuration.

The parameter can be further increased, and when the search is performed up to the 45th grid point the solution is fully attached, as evidenced by the oil-flow lines shown on Figure 6.15 , where we are looking at a side view of the vehicle as before. At this point, further increases of the parameter will not change the topology of the

ORIGINAL PAGE IS
OF POOR QUALITY

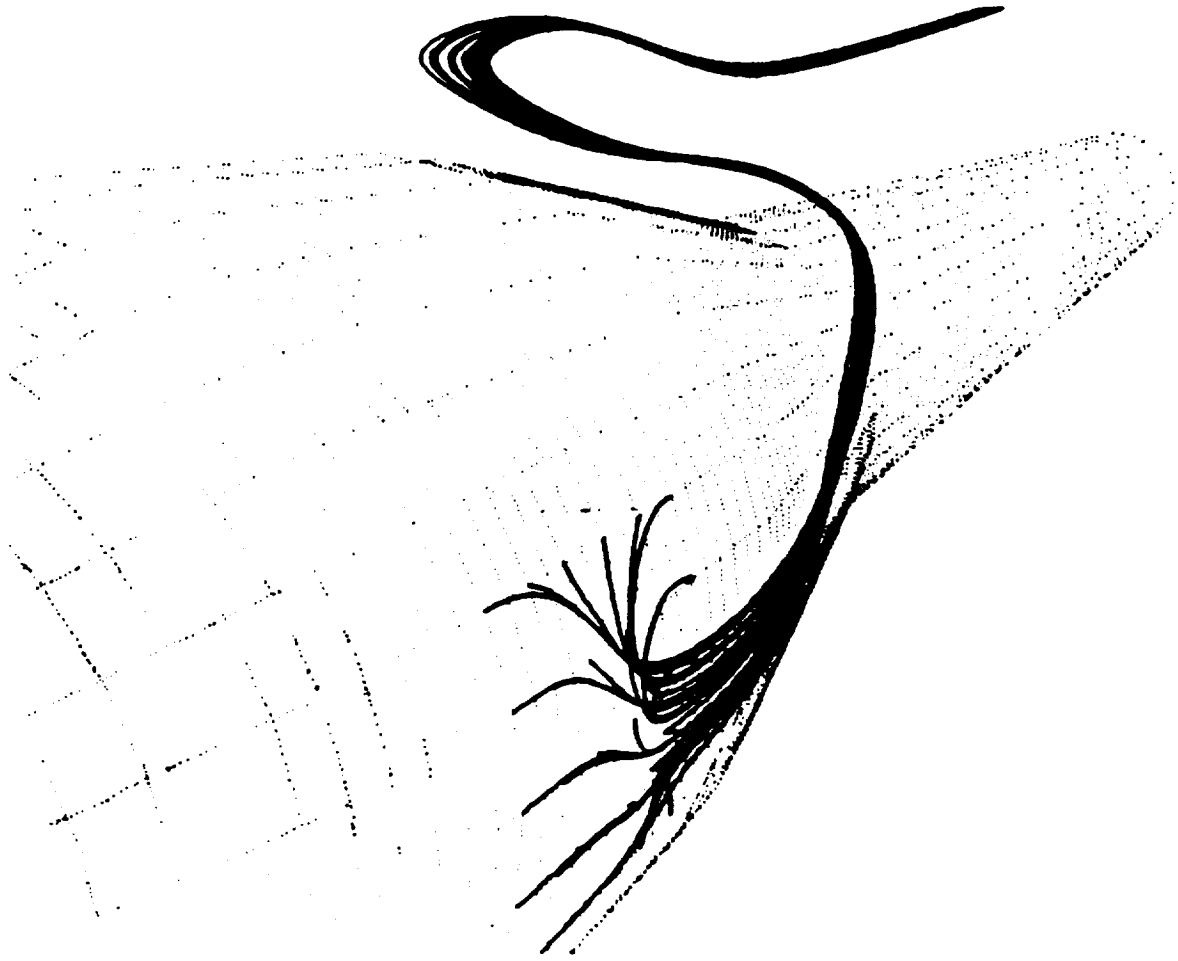

**Figure 6.13: Particle traces showing vortex leaving the body surface on the side of the vehicle.**

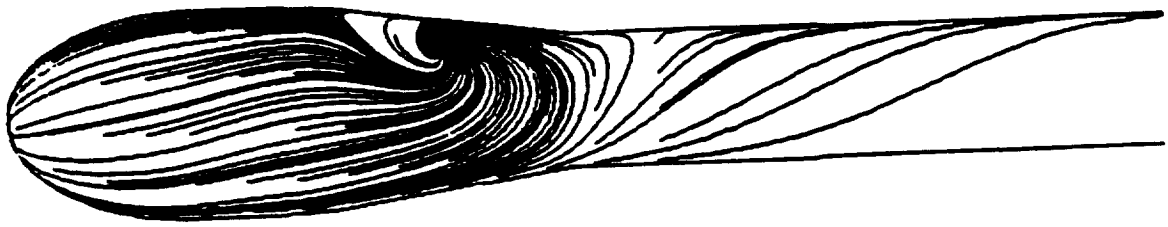

Figure 6.14: Side view of oil-flow lines for computation with search up to 35th grid point.

Figure 6.15: Side view of oil-flow lines for computation with search up to 45th grid point.

flow. However, when the search for the maximum velocity on the boundary layer velocity profile is performed up to the 55th grid point, some numerical stability problems start to be developed on the nose region. In this last case, i. e. , search up to 55th grid point, although a solution that looks very much like the one shown on Figure 6.15 can be obtained, the maximum residue could not be dropped below $10^{-3}$ and it was actually increasing at the point we stopped the computation.

Perhaps the most interesting point of all this discussion, at least as far as aeroelastic applications are concerned, is that despite the dramatic changes in flow topology the pressure coefficient distributions on the body are not much affected by all these variations on the parameters of the model. Of course, there are some alterations in the pressure coefficient distributions, but these are really minor changes considering the extreme variations in flow topology just described. It should be noted, however, that despite being a somewhat unexpected behavior at first, this actually makes some sense if one reasons in terms of boundary layer theory where the streamwise pressure variation is determined by the outside flow. It is true that this is correct only for unseparated flow, but it can still help the interpretation the results obtained. Furthermore, the same basic problems observed in the pressure coefficient distributions, and discussed earlier in this section, are still present regardless of the turbulence model parameters.

On the subject of obtaining a better pressure coefficient distribution on the body, another numerical experiment was performed. Since the data used for comparison of the steady state aerodynamic data was obtained for a 7% scale model[75] , there was the possibility that the actual flow on the experiment started laminar over the body. The experimental model had carborundum grit No. 30 applied in a circumferential band over some portion of the ellipsoidal nose region to ensure transition. An attempt was made to reproduce this situation computationally by letting the boundary layer start laminar at the nose, and then enforcing the transition at the same axial stations where the experiment had the carborundum grit.

The results obtained indicated that the laminar flow *expands faster*, and so better agreement with the experiment was obtained over the upstream portion of the nose region. However, the agreement was already very good over that portion

of the body (see, for instance, Figure 6.4). Since the experimental grit was located quite far forward on the nose, this beneficial effect of a faster expansion of the laminar boundary layer was not being felt at the location of the shock, which is where the problem was. This, however, suggested the idea of letting the boundary layer stay laminar over a larger portion of the nose, perhaps even up to the shock location or the point of separation.

Unfortunately, again, the results were not very encouraging. Although it is true that the assumption of laminar flow causes a faster expansion of the flow going over the body nose, it is also true that a laminar boundary layer separates sooner than a turbulent one. The net result was that the computational pressure coefficients would follow the experimental values better over the ellipsoidal nose, but the negative peak in $Cp$ was lower because separation would happen sooner. In other words, besides being a somewhat arbitrary procedure, this approach was causing the shock location, and the separation point, to move too far forward.

In light of all these observations, the idea was abandoned and the results presented in the previous section are for a fully turbulent flow, in the sense that the boundary layer is assumed to be turbulent since the very nose of the body. It should be mentioned, however, that it is very easy to implement these kinds of tests in the current code, since the turbulence modelling routines are probably the only portion of the code that is highly modular. Finally, it should be mentioned also that it is important for these kinds of calculation to ensure that the flow becomes turbulent at some point, at least after separation occurs. Otherwise, the separated flow usually becomes aerodynamically unsteady, if we insist in keeping the computational solution laminar. It is also unrealistic to expect that separated flow at those flight Reynolds number should remain laminar.

## 6.4 Configuration at Angle of Attack: Aeroelastic Results

Using the steady state solution described in Section 6.2 as the initial aerodynamic solution, aeroelastic analyses were performed for the Atlas-Able IV configuration by varying the dynamic pressure ($q_D$) while keeping other parameters constant. Pure aerodynamic solutions can be performed only in terms of nondimensional parameters, if one is interested only in nondimensional coefficients or quantities as result. However, when performing aeroelastic analyses, information is necessary regarding the (dimensional) freestream values and a reference length in order to consistently nondimensionalize the structural dynamic equations. For the same reason, it is important to decide whether one is considering a model or the full scale vehicle. In our case, we will consider a full scale vehicle since the natural frequency information we have in this case is for a full scale model.

Although the geometrical information about this configuration was obtained only in nondimensional form from References [4] and * , the data of Reference [75] was dimensional. Considering that the latter presented data for a 7% scale model and we wanted dimensions for a full scale vehicle, we chose the reference length $\ell_0 = 0.81280\ m$ , which in this case is the diameter of the afterbody cylinder. The freestream speed of sound was chosen to match the experimental data of Reference [81] and it was set at $a_\infty = 336.75\ m/s$ . The freestream density was calculated at every run in order to produce the desired freestream dynamic pressure. Note that by keeping the freestream Mach number and $a_\infty$ constants, the only parameter left to vary the dynamic pressure was the freestream density.

Also note that, although the speed of sound value being used would correspond to flight at approximately 1000 $m$ altitude if we consider a standard atmosphere [78] , the idea of having a constant speed of sound with a varying freestream density is realistic if we think in terms of flight in the stratosphere. In this portion of the atmosphere, the temperature is constant and therefore the speed of sound is constant, while the density varies with the altitude due to the changes in the pressure. It should be also pointed out that we do not have to keep the speed of

* Ericsson, L.E., personal communication, April 1987.

sound constant in the analysis, although we could not devise a more realistic way of varying the dynamic pressure while keeping the Mach number constant than the one described above. The reason for keeping the Mach number constant is a practical rather than a theoretical one. Essentially we want to avoid having to regenerate the initial aerodynamic solution for every aeroelastic run, because of the computational costs of so doing. The solution is to perform aeroelastic runs varying some other parameter, for instance the dynamic pressure, while keeping Mach number, angle of attack, and all the other parameters used to generate the initial aerodynamic solution constants.

Three elastic structural mode shapes were used in the present analysis, and the rigid body degrees of freedom were assumed to be constrained. The first mode natural frequency was estimated as 5 Hz , according to discussions with Ericsson * A comparison of the first and second mode responses presented by Woods and Ericsson [4] , together with some typical launch vehicle responses available from Bisplinghoff and Ashley [60] , permit the estimation of a value of 17 Hz for the second mode frequency. Finally, the third mode frequency was picked at 29 Hz .

The mode shapes were obtained by an extrapolation of the information available in Woods and Ericsson [4] , together with additional information regarding the location of the first nodal point for the first mode * . The mode shapes used are shown in Figure 6.16 . It is important to point out that all modes go to zero amplitude at the downstream boundary because this was the way chosen here to constrain the rigid body degrees of freedom. In other words, the downstream computational boundary is held fixed throughout the calculation. It must also be pointed out that, for $x/d$ greater than approximately 12.5, the mode shapes were obtained by extrapolation of the existing data using low order polynomials. More specifically, cubic polynomials were used for all three modes, and the boundary conditions enforced were that they should give the same values of deflection amplitude at the last two available experimental points, as well as giving zero deflection and slope at the downstream boundary.

A constant value of mass per unit of length was used in these calculations, which may be sort of an oversimplification. We do recommend a more careful description

* Ericsson, L.E., personal communication, April 1987.

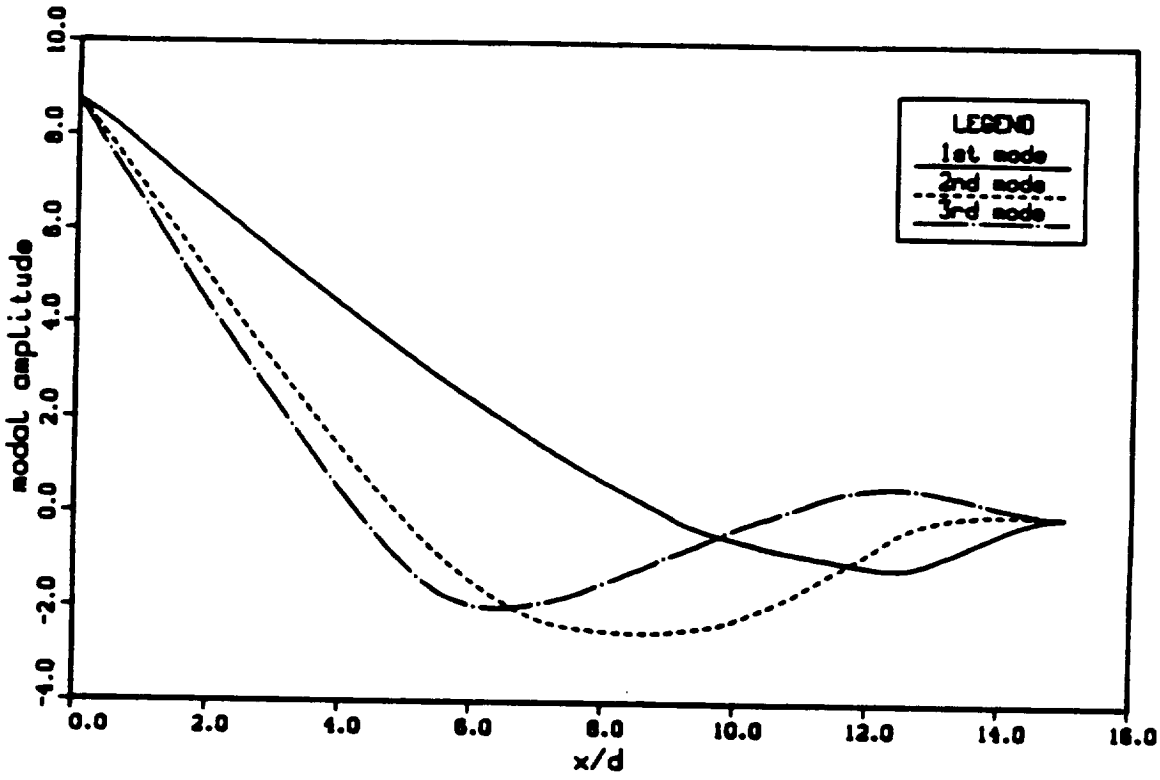


Figure 6.16: Structural mode shapes used for aeroelastic analysis of the Atlas-Able IV configuration.

of the mass properties of the vehicle if more accurate results are sought. This parameter was obtained from data available on some Atlas boosters , and a value of 2555 kg/m was used. The structural damping coefficients were estimated from data presented by Woods and Ericsson [4] , and the values used were $\zeta_1 = 0.0010$ , $\zeta_2 = 0.0018$ and $\zeta_3 = 0.0036$ , for the first, second and third modes, respectively.

The initial perturbation necessary to start the oscillation is provided, as in the cases studied in the previous chapter, by the fact that the initial aerodynamic solution is calculated for a rigid vehicle. Since the angle of attack is different from zero, there is a net aerodynamic force distribution that is not balanced yet by elastic forces due to vehicle deformation. In other words, the body deflected position is not in equilibrium with the applied force distribution.

A typical vehicle response in this case, for an intermediate value of dynamic pressure, $q_D = 400$ psf , can be seen in Figure 6.17 , where the time history of the generalized modal deflections is shown for all three modes. As it could be expected, the first mode response dominates the other modes, and so details of the response on the second and third modes are shown in Figure 6.18 . All three modes are damped in this case, which is not surprising since we did assume some small amount of structural damping and the dynamic pressure is still in the intermediate range. What is somewhat unexpected is the fact that the damping coefficient is higher than the plain structural damping coefficient for all the modes, indicating that the airstream is contributing positive damping for all the modes in this case.

This increase in damping is really not very significant for the second and third modes, being only of the order of 6% and 3% , respectively. However, the damping coefficient for the first mode is 0.0016 , which implies a 60% increase over the corresponding structural damping coefficient. It should be noted, however, that we are presenting some very small numbers. It may be questionable how far one can trust the precision of the numerical results, considering the amount of computation and possible truncation errors involved in these calculations. Nevertheless, the qualitative result leaves no margin to question. It indicates that the first mode is damped much faster than it would be the case under the structural damping alone.

It is instructive to mention that the damping coefficient is calculated from the

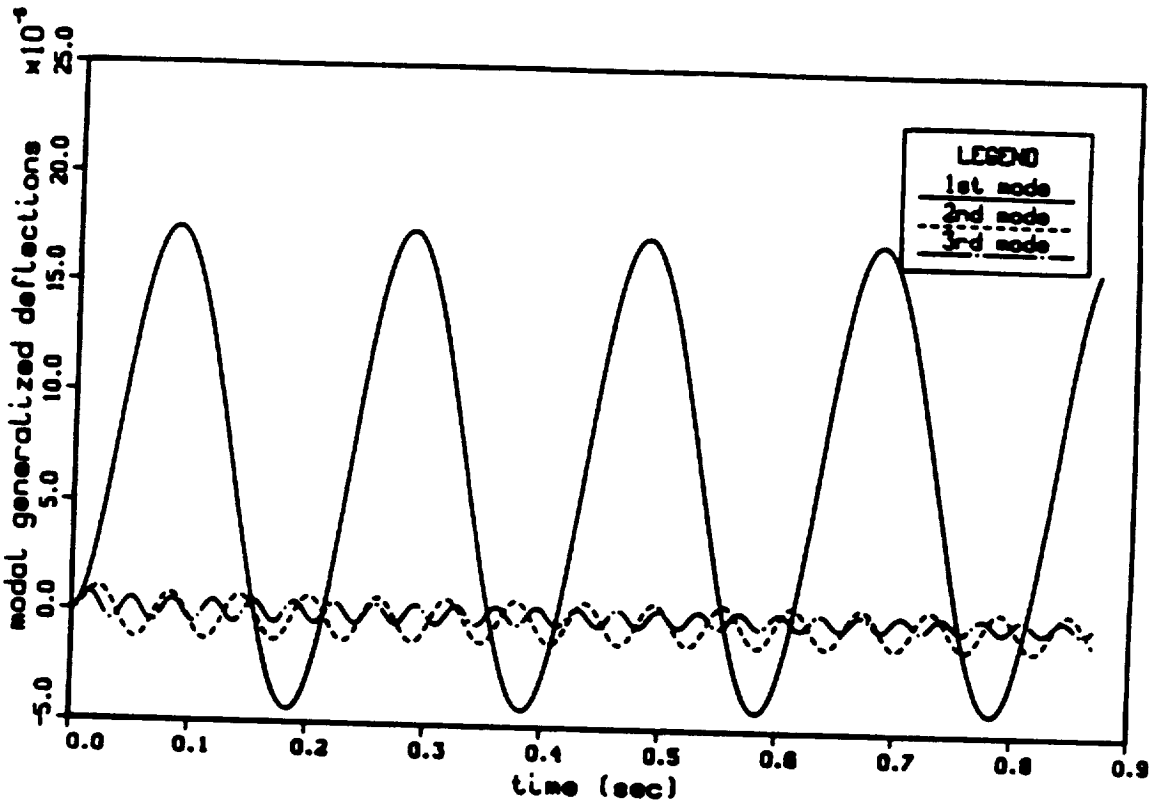


Figure 6.17: Modal response for Atlas-Able IV configuration at 400 psf dynamic pressure ($M_\infty = 0.85$ and $\alpha = 6°$).

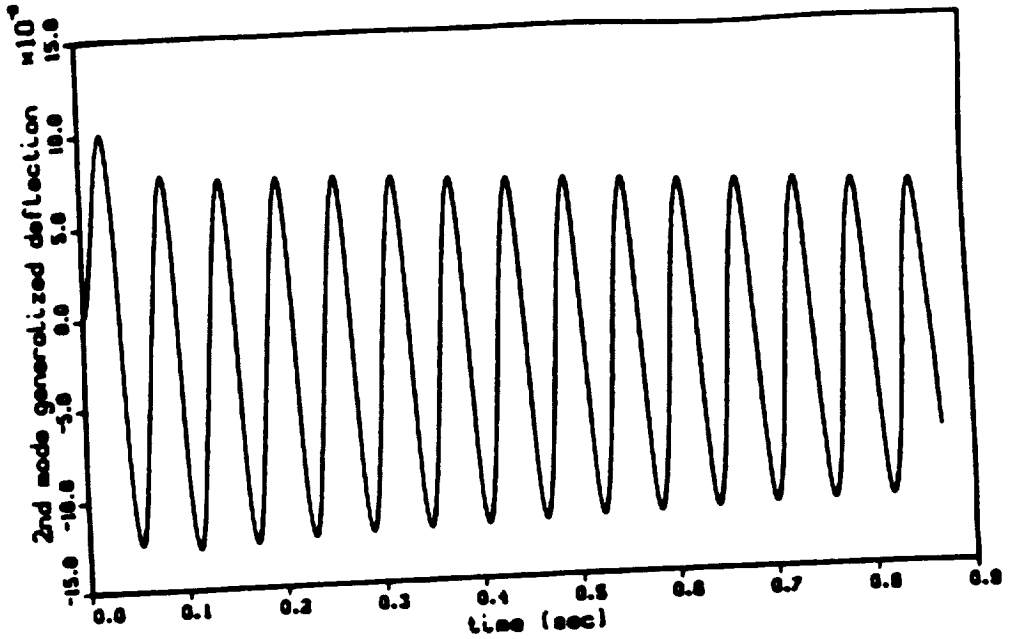


(*a*) 2nd mode response.

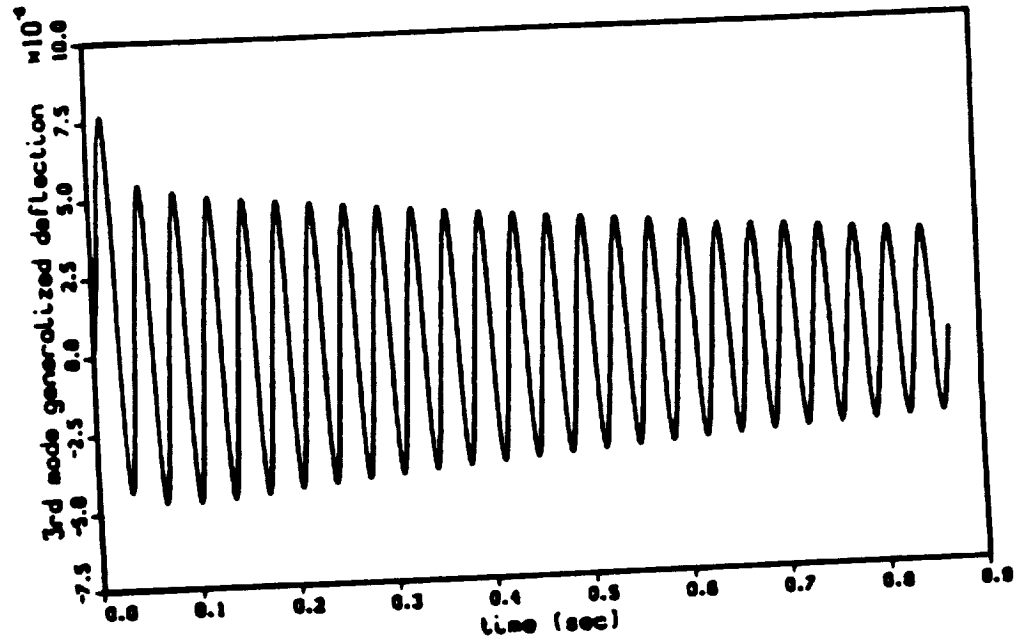


(*b*) 3rd mode response.

Figure 6.18: Detail of the response on the second and third modes at 400 psf dynamic pressure.

time histories of the response in each mode by assuming an exponential decay. The code generated for this purpose initially estimates the mean value of the oscillation. Then, using a least squares curve fitting technique, it finds the parameters for the exponential envelope of the response. The slope of the natural logarithm of this envelope curve is the product of the damping coefficient by the natural frequency of that particular mode. From the parameters of the exponetial envelope, the structural damping coefficient can be obtained.

It can also be observed from the results that the frequency of the response in each mode is very close to its natural frequency. This is in agreement with the results obtained in the previous chapter, where it was observed that the frequency of the response remains approximately unchanged regardless of the dynamic pressure. This may not seem typical for those used to aeroelastic analysis of lifting surfaces, where the mechanism of flutter is usually associated with the merging of the frequencies for two different modes. However, if an instability exists in the present case, it will probably be an one degree of freedom phenomenon, and the fact that the frequencies remain unchanged is indeed the expected result.

The response in terms of the generalized deflections for a much higher value of dynamic pressure, $q_D$ = 1174 psf , is shown in Figure 6.19 , where all three modal amplitudes are presented. As expected, the magnitude of the response in the first mode is again much larger than for the other two modes. Details of the response in the second and third modes are shown in Figure 6.20 . Except for the fact that the amplitudes are about one order of magnitude higher, these results are strikingly similar to those obtained for 400 psf dynamic pressure. This is not the anticipated behavior. For such high value of dynamic pressure, one would expect that the aeroelastic instability condition would be evident, assuming that the configuration would develop any aeroelastic problem at this flight condition. Even more interesting, however, is the fact that the damping coefficients for all three modes in this case are higher than their corresponding values at 400 psf .

This last observation raised questions about what kind of generalized aerodynamic forces were being computed by the method, since a dynamic pressure of 1174 psf is already somewhat higher than what is actually encountered at this

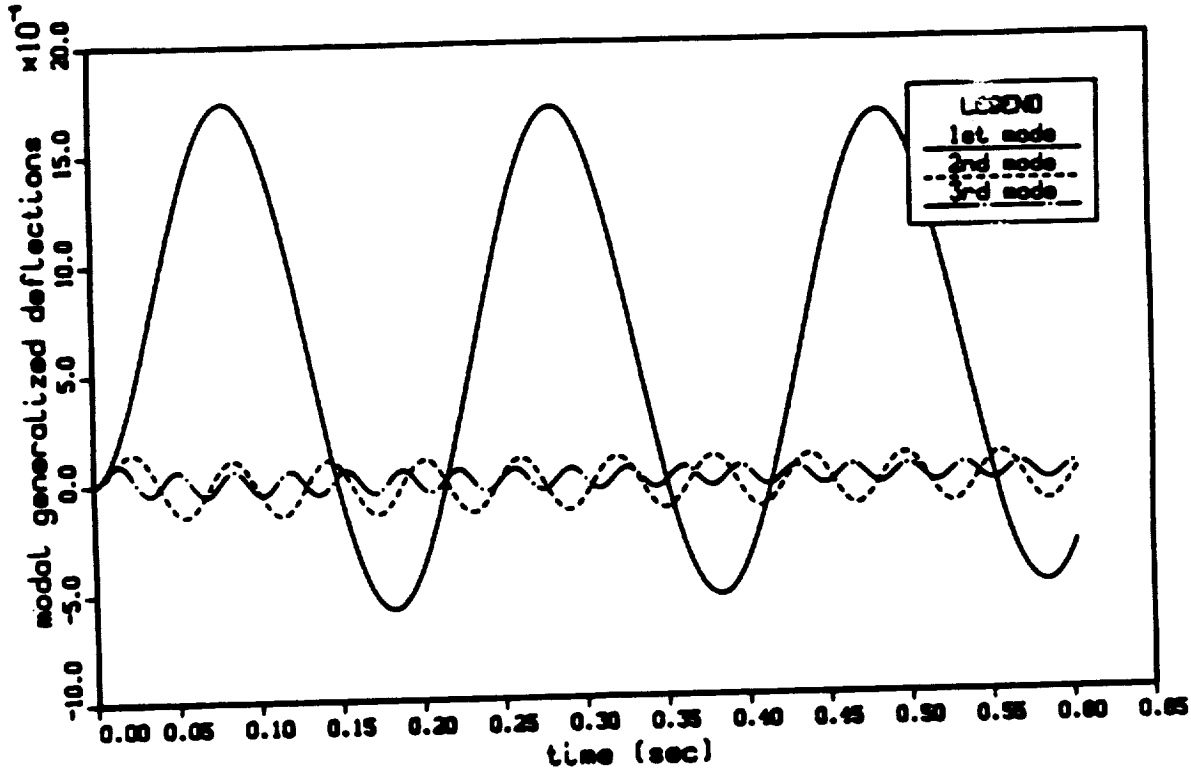


Figure 6.19: Modal response for Atlas-Able IV configuration at 1174 psf dynamic pressure ($M_{\infty}$ = 0.85 , $\alpha = 6°$).

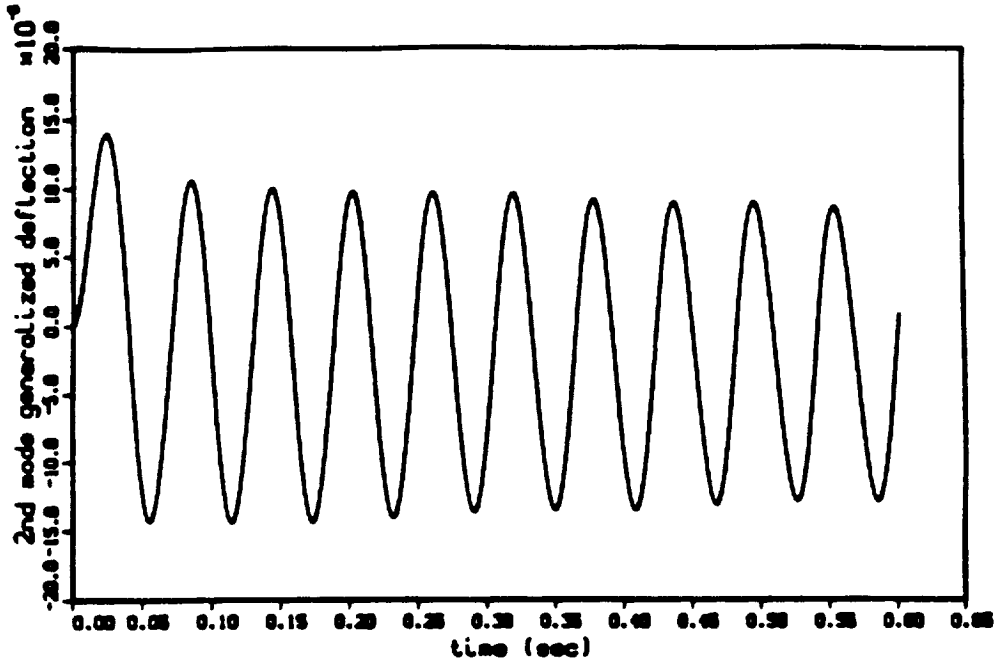


(*a*) 2nd mode.

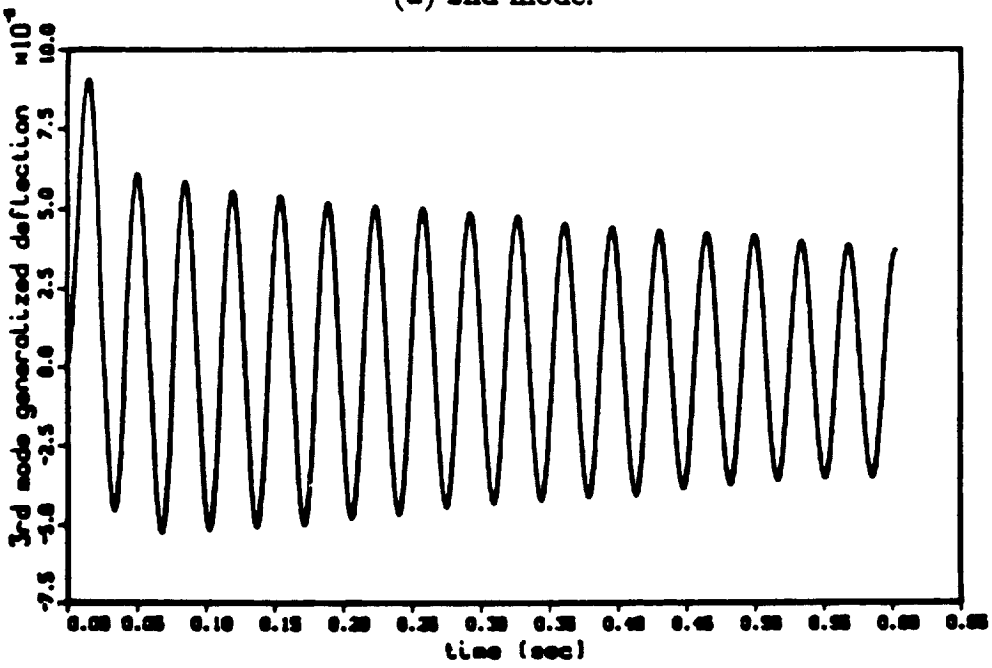


(*b*) 3rd mode.

Figure 6.20: Detail of the response on the second and third modes for 1174 psf freestream dynamic pressure.

ORIGINAL PAGE IS
OF POOR QUALITY

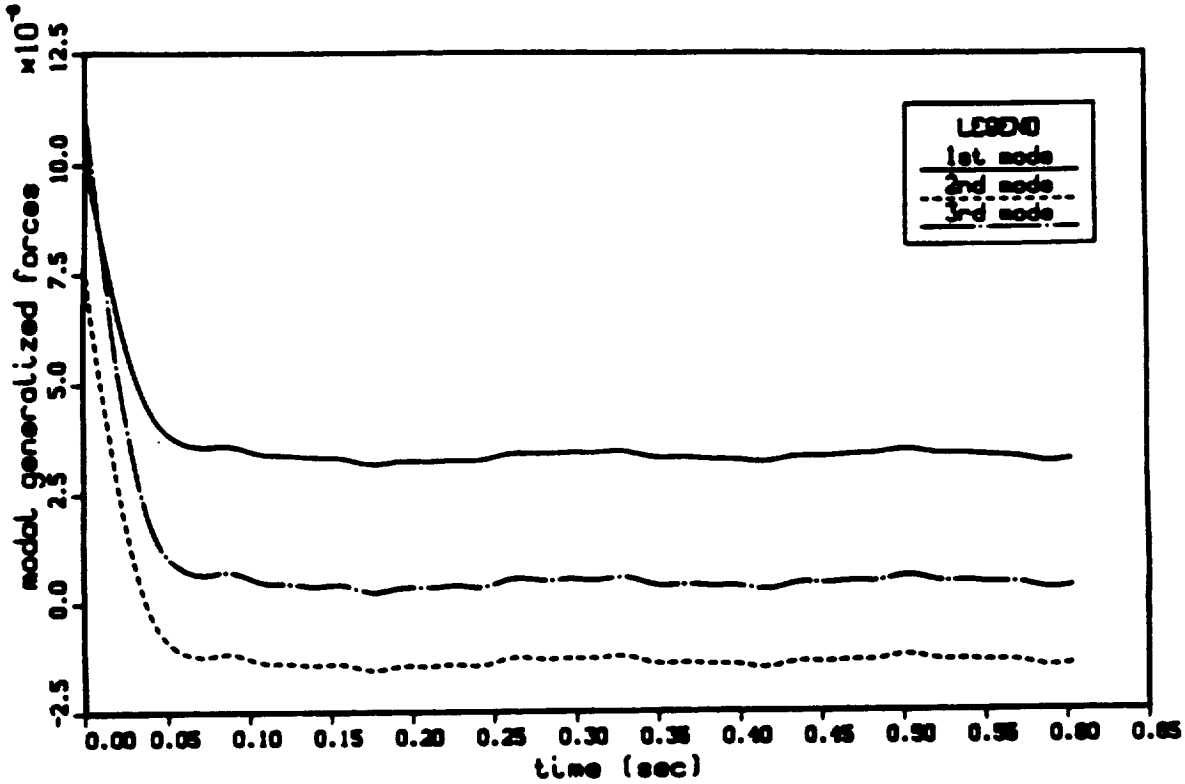


Figure 6.21: Generalized aerodynamic forces on Atlas-Able IV configuration at $M_\infty = 0.85$ , $\alpha = 6°$ and $q_D = 1174$ psf .

flight Mach number in practice. A plot of the generalized aerodynamic forces for the 1174 psf dynamic pressure case can be seen in Figure 6.21 . If we remember a previous discussion concerning how the initial perturbation is introduced to start the oscillation, the response observed in Figure 6.21 is indeed the expected result. In other words, there is a initial transient that takes into account the fact that the deflected position is not in equilibrium with the applied aerodynamic load. This is shown in the figure by the initial drop on the value of the modal generalized forces. After approximately 0.05 sec the forces settle down to some nonzero mean value together with some small oscillations around this mean. Although not completely apparent from Figure 6.21 , this behavior can easily be seen if we look at expanded views of the response in each mode after the initial transient has passed. This is done in Figure 6.22 .

ORIGINAL PAGE IS
OF POOR QUALITY

ORIGINAL PAGE IS
OF POOR QUALITY

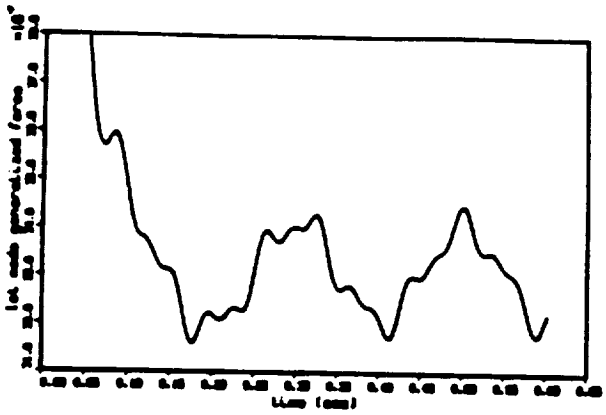

(*a*) 1st mode.

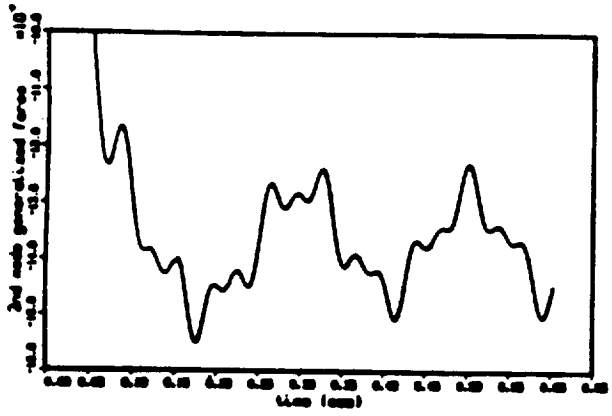

(*b*) 2nd mode.

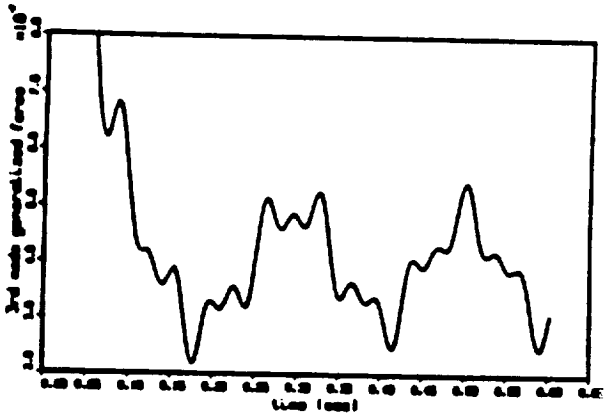

(*c*) 3rd mode.

Figure 6.22: Expanded view of the modal generalized forces showing oscillatory behavior after initial transient has passed ($q_D = 1174$ psf ).

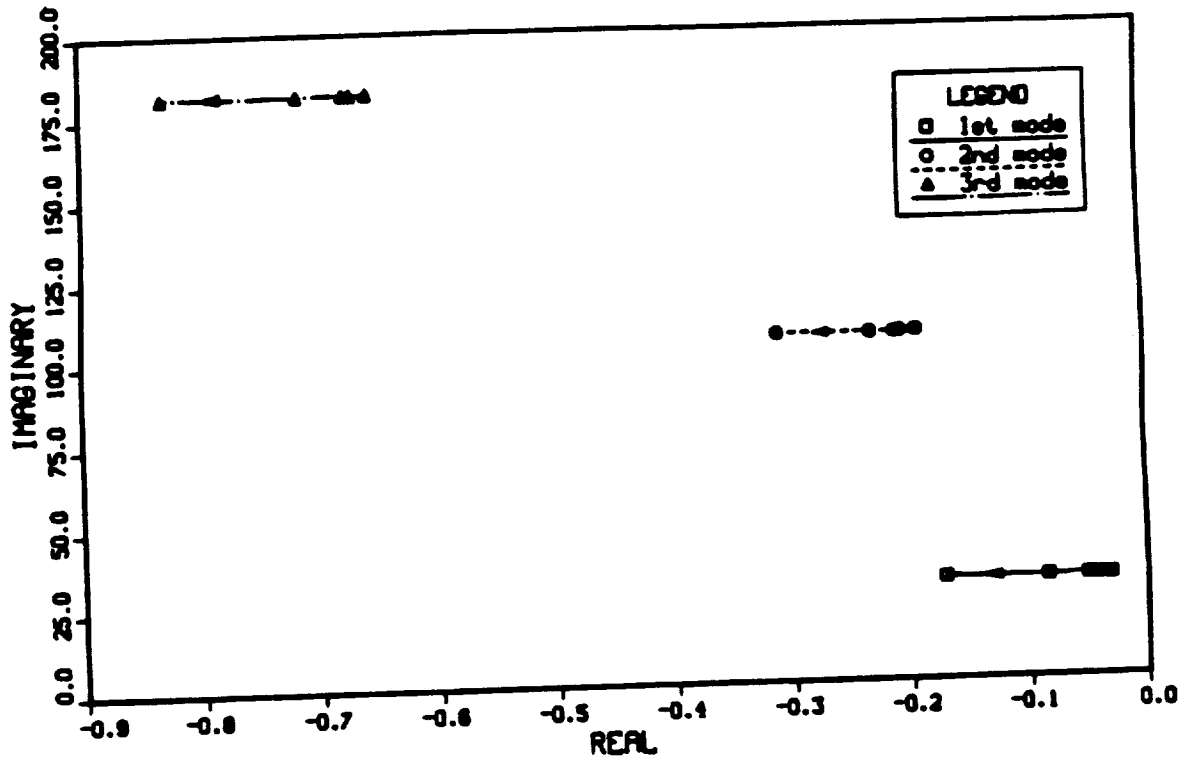


Figure 6.23: Aeroelastic root locus for Atlas-Able IV configuration at $M_\infty = 0.85$ and $\alpha = 6°$ . The parameter varied is flight dynamic pressure.

Since the magnitude of the response on the first mode is much larger than on the other modes, the overall body deflection is dominated by the first mode. There is no surprise that the generalized aerodynamic forces follow the first mode oscillation, with just some minor higher frequency influence. However, the important observation is that the forces show very little lag with respect to the deflection. This can explain why a damped behavior is being obtained even at such high dynamic pressures. A study of the modal generalized forces for the 400 psf case yielded similar conclusions.

A few other cases for different values of dynamic pressure were run, and all the results are summarized on the root locus plot shown in Figure 6.23 . As before, the free parameter of the locus is the dynamic pressure, and the arrows indicate the direction of increasing dynamic pressure. It can be noticed that the frequency

ORIGINAL PAGE IS
OF POOR QUALITY

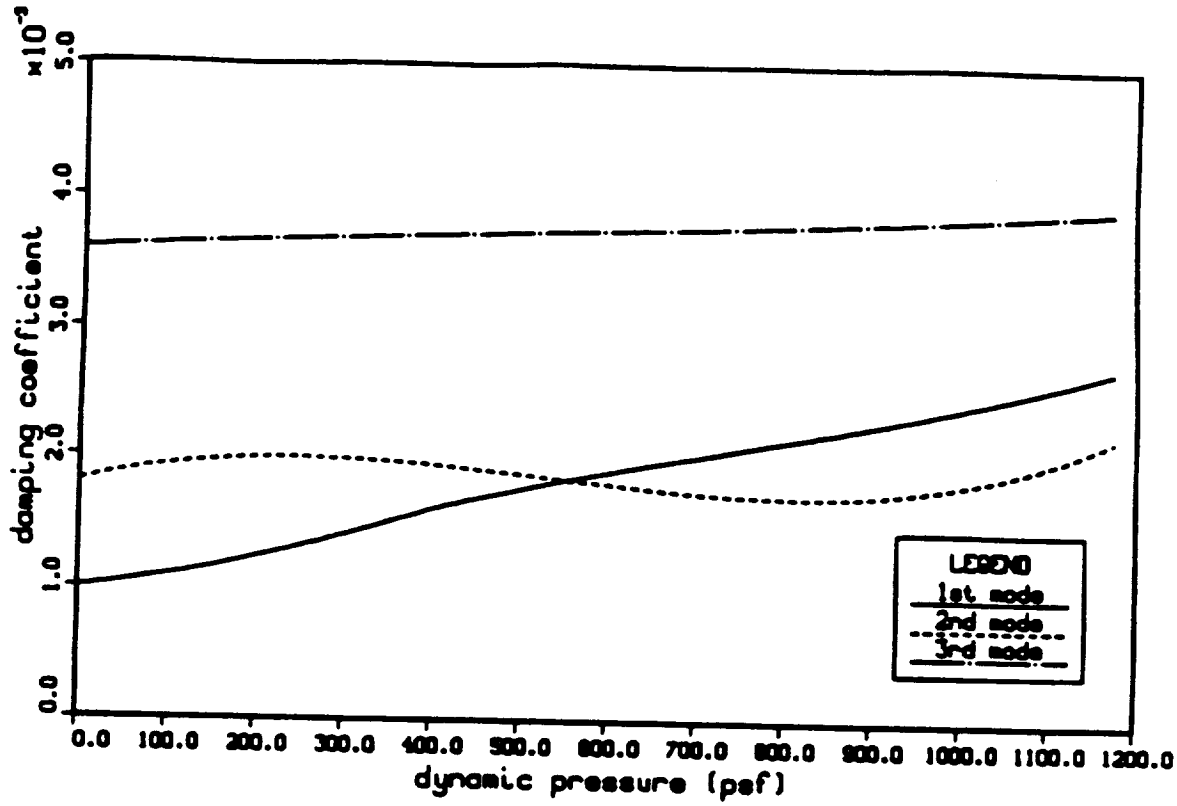


Figure 6.24: Modal damping coefficient on Atlas-Able IV configuration for flight at $M_\infty = 0.85$ and $\alpha = 6°$ .

remains approximately unchanged regardless of the value of dynamic pressure, as we have previously mentioned. It is evident that no instability is present, and higher values of dynamic pressure just seem to move the roots deeper into the left-hand plane.

It is difficult to completely see the behavior of the solution for smaller values of dynamic pressure from the root locus plot because of the small variation in the frequency. A better understanding can be obtained from a plot of the damping coefficient in each mode as a function of the dynamic pressure, which can be seen in Figure 6.24 . The first and third modes show a continuous increase in the damping as the dynamic pressure is increased. The behavior of the second mode is more interesting, showing an increase in damping in the lower range of dynamic pressures, then the damping starts to decrease as this parameter is further increased. However,

at the very high values of dynamic pressure, the damping on the second mode starts to increase again.

From a physical standpoint, the results indicate that the first and third modes show no tendency of presenting aeroelastic problems. The second mode, although it never goes unstable, indicates a tendency towards instability in the dynamic pressure range of approximately 500 to 800 psf . It is interesting that, according to the results presented by Woods and Ericsson [4] , the second mode is the one that should present flutter problems. Despite the fact that we are not capturing the expected instability, our computational results are showing some of the correct trends.

Part of the foregoing discrepancy between prediction and expectation can be explained by the structural data used, which involved some approximations due to the lack of the actual vehicle data. It is well known that mass distribution can have significant effects on flutter results and, as we have previously discussed, some rather severe assumptions were introduced here. The difficulties in getting the correct shock strength with the current aerodynamic flow solver may also have some role to play in explaning part of the difference in the results. As we have mentioned before, the shock motion and the shock-boundary layer interactions are expected to be an important feature of the mechanism that causes the instability. The capability of numerically reproducing the instability can be impaired by the lack of a better resolution of the shock region.

The computational costs of these aeroelastic solutions is not trivial, and a few comments about this issue would be important. For the grid size being used in the present investigation, each aeroelastic iteration takes approximately 12 CPU seconds in a CDC Cyber 205 computer. The calculation of the vehicle response, for each flight condition considered, involves typically somewhere around 3600 time steps due to the limitations on time step size in order to keep the time-accuracy of the solution. Of course, this is also dependent upon the range of natural frequencies considered, and the number of iterations above is correct for the frequencies used in this work. Actually, it is determined by the lowest frequency, since we must get at least a few cycles of the lowest mode in order to fully ascertain the stability of

the configuration.

The significant outcome is that something of the order of 12 CPU hours of a Cyber 205 are necessary in order to produce a vehicle response such as the one shown in Figure 6.17 . Note that this does not count the time required to generate the initial aerodynamic solution. Furthermore, this is not the overall computer time for one aeroelastic run either. As we mentioned before, due to the heavy amount of I/O required on these aeroelastic solutions (because the database is not core contained) , the CPU time represents only 30% of the overall system time.

## 6.5 Study of a Zero Angle of Attack Case

The Atlas-Able IV configuration was also studied at a zero angle of attack flight condition. Since the geometry was the same, we used the same grid system previously generated for this analysis. The structural and aerodynamic data were also the same, except that in this case the angle of attack was set to zero, and so were all the structural damping coefficients. The initial aerodynamic solution was, then, calculated for the $M_\infty = 0.85$ and $\alpha = 0°$ flight condition. The Reynolds number was the same as before, and the boundary layer was considered turbulent.

A flow visualization of the steady state solution obtained, which will be the starting solution for aeroelastic analysis, can be seen in Figure 6.25 . The figure shows pressure coefficient, Mach number and density contour plots for a side view of the body. The solution is axisymmetric, as is clear from the figure since the top and bottom contours are a mirror image of each other. Even at zero angle of attack, there is flow separation over the vehicle. This is evidenced by the reversed velocity profiles shown in Figure 6.26 for a portion of a longitudinal plane. The flow separates still over the forebody cylindrical section, and the boattail is completely immersed in the region of reversed flow. Reattachment will occur only downstream of the boattail over the afterbody cylinder region.

The computed pressure coefficient distribution over the vehicle is compared to experimental results[75] as a way of validating the steady state aerodynamic solution. This comparison can be seen in Figure 6.27 . It is not particular important

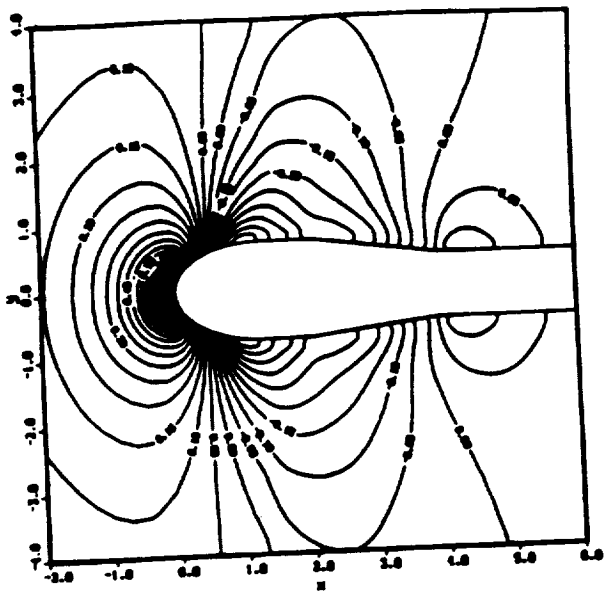

(a) Pressure coefficient contours.

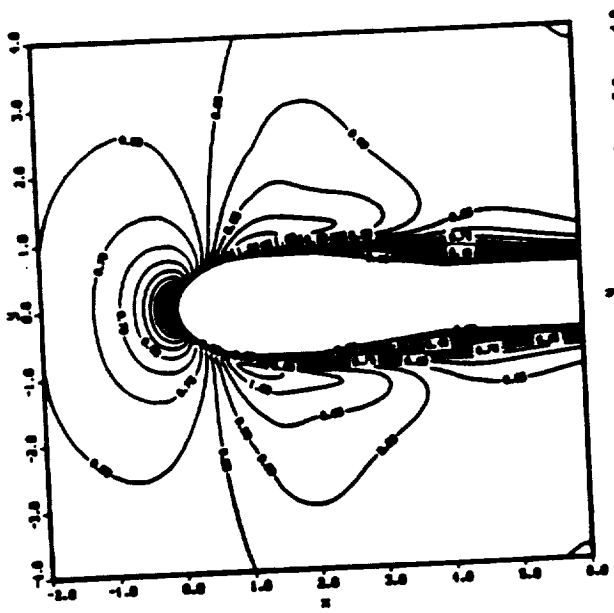

(b) Mach number contours.

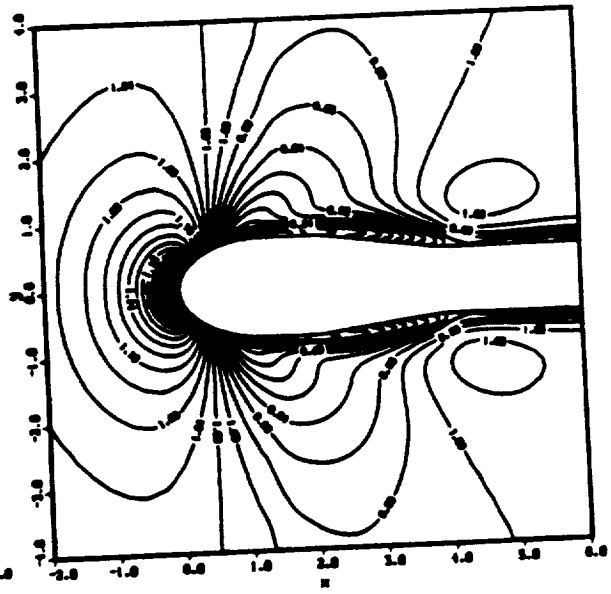

(c) Density contours.

Figure 6.25: Flow solution about an Atlas-Able IV vehicle at $M_\infty = 0.85$ and $\alpha = 0°$ (side view).

ORIGINAL PAGE IS
OF POOR QUALITY

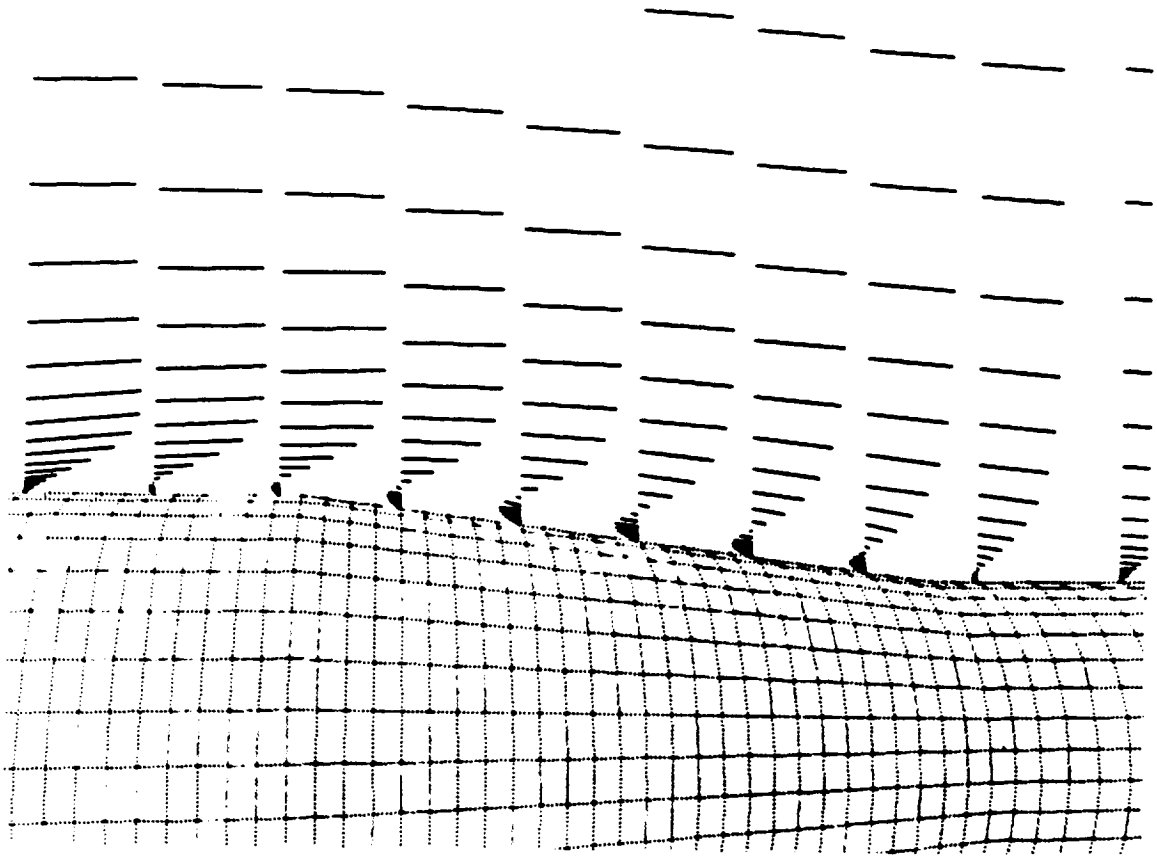

Figure 6.26: Velocity profiles for flow over an Atlas-Able IV configuration at $M_\infty = 0.85$ and $\alpha = 0°$ (side view).

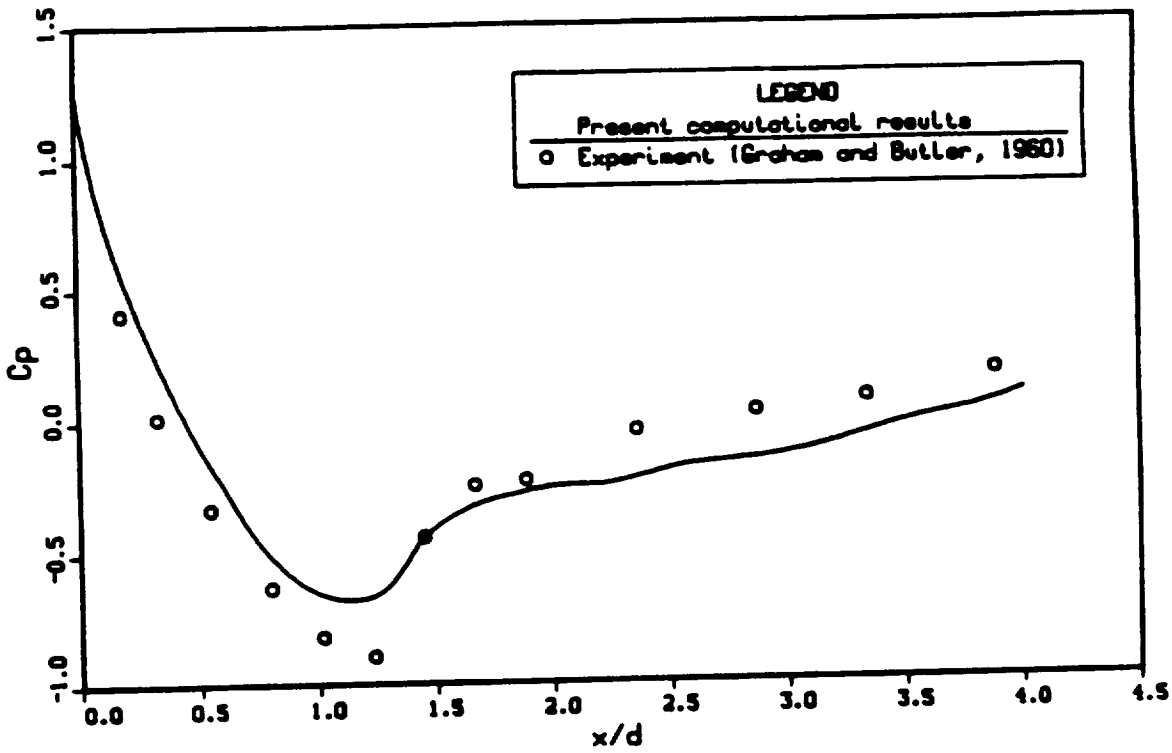


Figure 6.27: Pressure coefficient distribution over an Atlas-Able IV payload at $M_\infty = 0.85$ and $\alpha = 0°$ .

ORIGINAL PAGE IS
OF POOR QUALITY

which longitudinal plane of results was used for this comparison, because the solution is axisymmetric. However, for the sake of completeness, the plane corresponding to the leeside in case of a positive angle of attack was the one used. The results show the same features observed in the solution at angle of attack. The computational pressure coefficients follow the correct trend of the experimental results, but the shock resolution is less than perfect. As was previously discussed, problems with the numerical dissipation algorithm may be causing the discrepancies in these results.

Only one aeroelastic case was run at this flight condition because of time limitations. The dynamic pressure was set at 400 psf . The structural data used were the same considered in the cases studied in the previous section, except that the structural damping coefficients were set to zero in the present simulation. Since the angle of attack is zero, we need a different way of introducing the initial perturbation that starts the oscillation. An initial displacement of the first mode generalized coordinate, while keeping the other two modes undisturbed, was the method selected here. The magnitude of the initial deflection was selected to be of the same order of the maximum elastic displacement observed in that mode at 6° angle of attack when the same dynamic pressure was being used.

Time history of the response in terms of the generalized modal deflections is shown in Figure 6.28 . It must be emphasized that all three modes are shown on this figure. However, due to the large difference in the magnitude of the response, the second and third modes are only seen as a zero line. An expanded view of these latter modes response is presented in Figure 6.29 . Just by looking at the results, it is clear that the oscillation amplitude of the second and third modes seems to be growing. The first mode appears to be neutrally stable. Furthermore, the higher modes seem to be modulated by by the first mode response.

A more complete analysis of the first mode response can be accomplished using the same software developed for the study of the previous aeroelastic runs. The result of the analysis is that the response is at a frequency of 5 Hz , which is exactly the natural frequency for this mode, and that the damping coefficient is $\zeta_1 = -9 \times 10^{-6}$ . In a strict sense, this mode would be called unstable since the

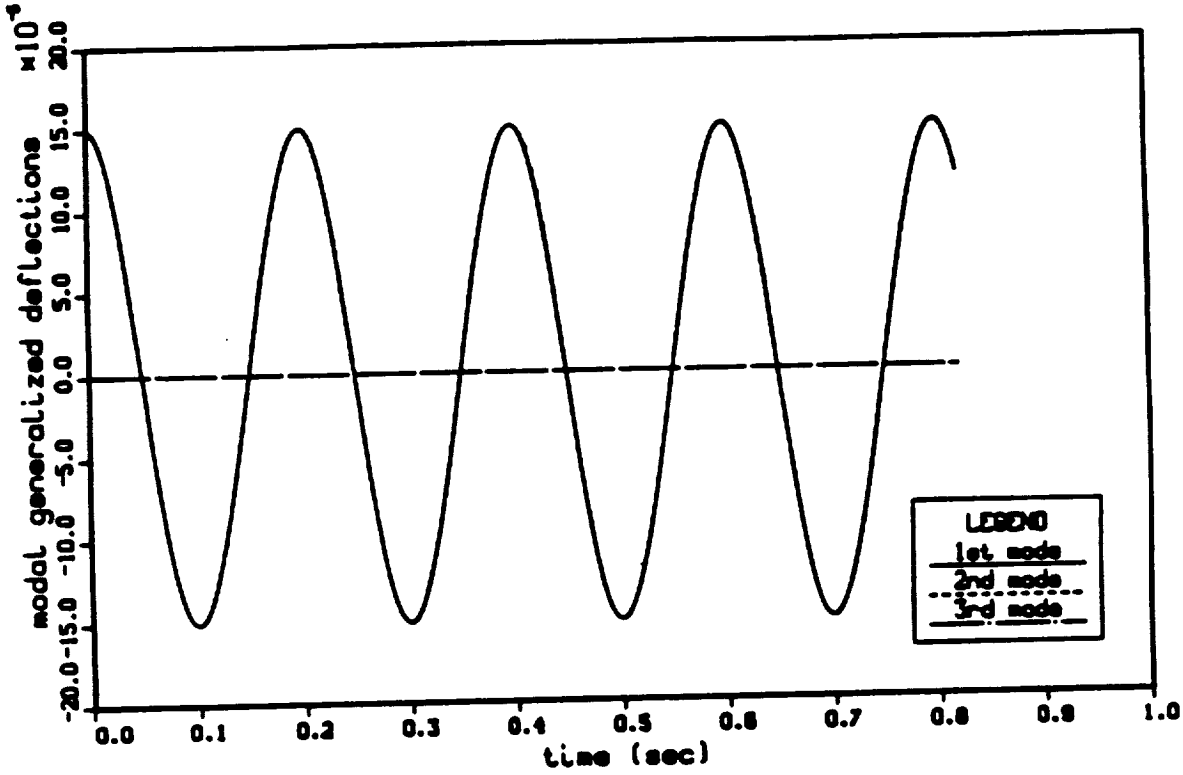


Figure 6.28: Modal response of Atlas-Able IV at $M_\infty = 0.85$ , $\alpha = 0°$ and dynamic pressure $q_D = 400$ psf .

ORIGINAL PAGE IS
OF POOR QUALITY

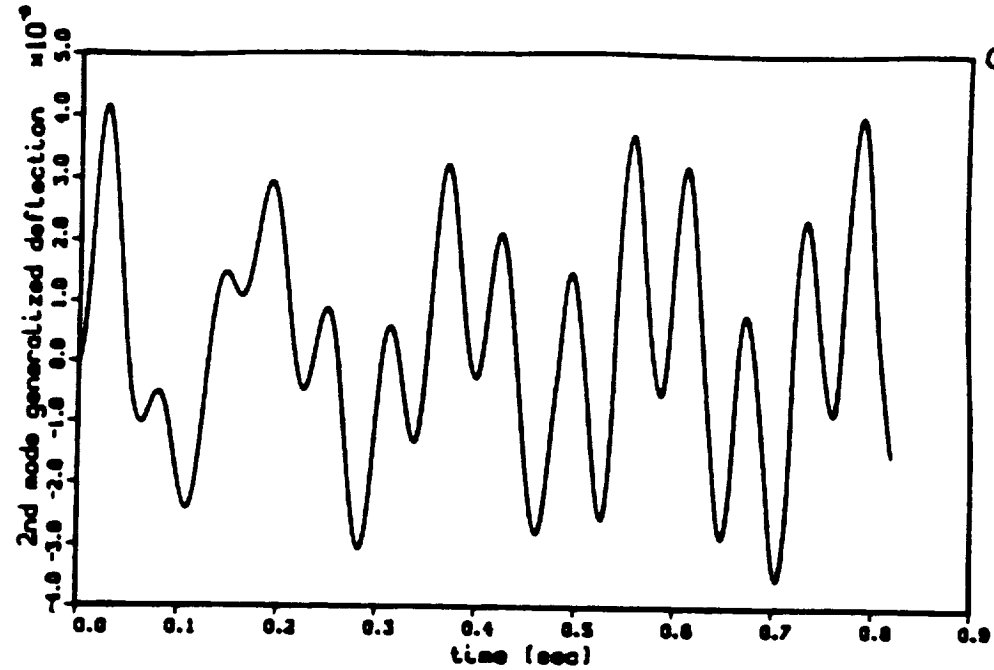


(*a*) 2nd mode.

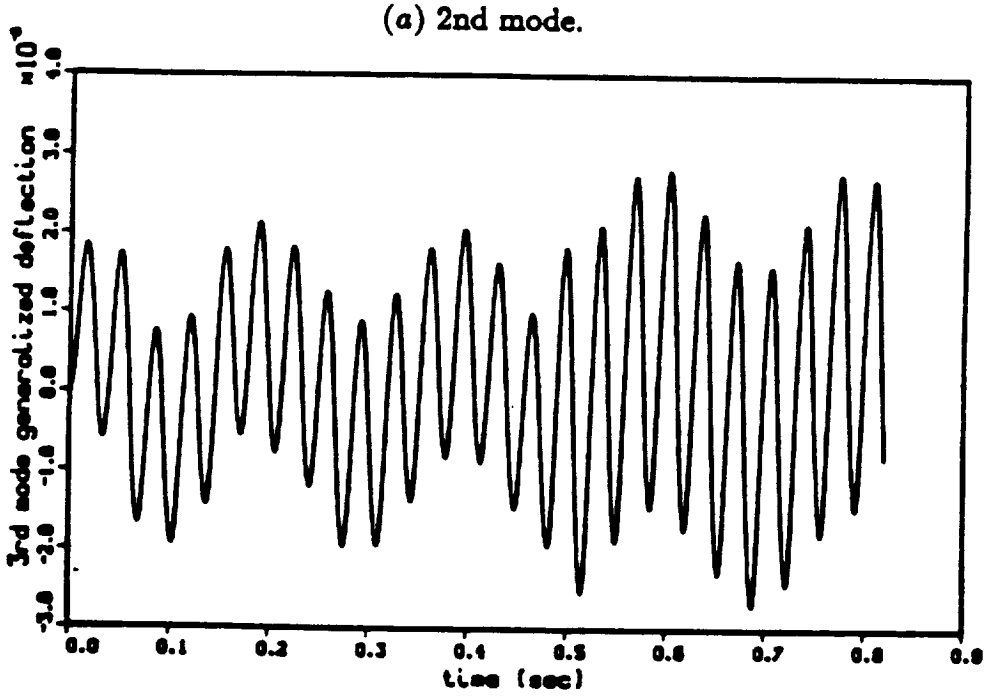


(*b*) 3rd mode.

Figure 6.29: Expanded view of response on the second and third modes at $M_\infty = 0.85$ , $\alpha = 0°$ and $q_D = 400$ psf .

damping coefficient is negative. However, considering the smallness of the value of $\zeta_1$ , it is probably more appropriate to accept the mode as neutrally stable. It is important to look at the problem from a practical point of view too. Since the vehicle will be accelerating through the transonic regime, and not flying continuously in it, such an extremely slow-growing instability would probably be of no concern.

Due to the apparent modulation of the response on the second and third modes, their study is a little more complex. We decided to study first the frequency content of the responses shown in Figure 6.29 . This can be done by taking the Fourier transform of those time traces. The result of such operation is shown in Figure 6.30 , where we are plotting the magnitude of the FFT of the response on each of those modes. The reader should note that, rigorously, the Fourier transform of a diverging signal does not exist. Here, however, we are simply taking a discrete FFT over a finite time interval. For the second mode response, the peaks at 5 and 17 Hz are evident from Figure 6.30($a$) . Similarly, for the third mode, peaks at 5 and 29 Hz can be seen in Figure 6.30($b$) .

It is interesting to note the relative magnitude of the response in each frequency. The response on the third mode seems closer to the expected result, where the spike at 29 Hz is much larger than the one at 5 Hz . The trend is reversed in the second mode response, where the 5 Hz peak has a larger magnitude than the one at 17 Hz . This explains why the third mode response is much "cleaner", in the sense that it is much easier to distinguish between the higher frequency response and the modulation itself. There seems to be more interaction of the two frequencies in the second mode response, which accounts for the more complex pattern in Figure 6.29($a$) . Moreover, with the two frequencies being closer to each other, it is understandable that the time trace should get more complex.

Although it seems clear from Figure 6.29 that the amplitude of response in those modes is increasing, we attempted to filter out the 5 Hz portion of it. This can be accomplished by eliminating the 5 Hz component of the Fourier transform of the response, and then taking the inverse transform. We were not completely successful in eliminating the modulation, and the filtered third mode response does not add much information to what can already be seen from Figure 6.29 ($b$) . For the

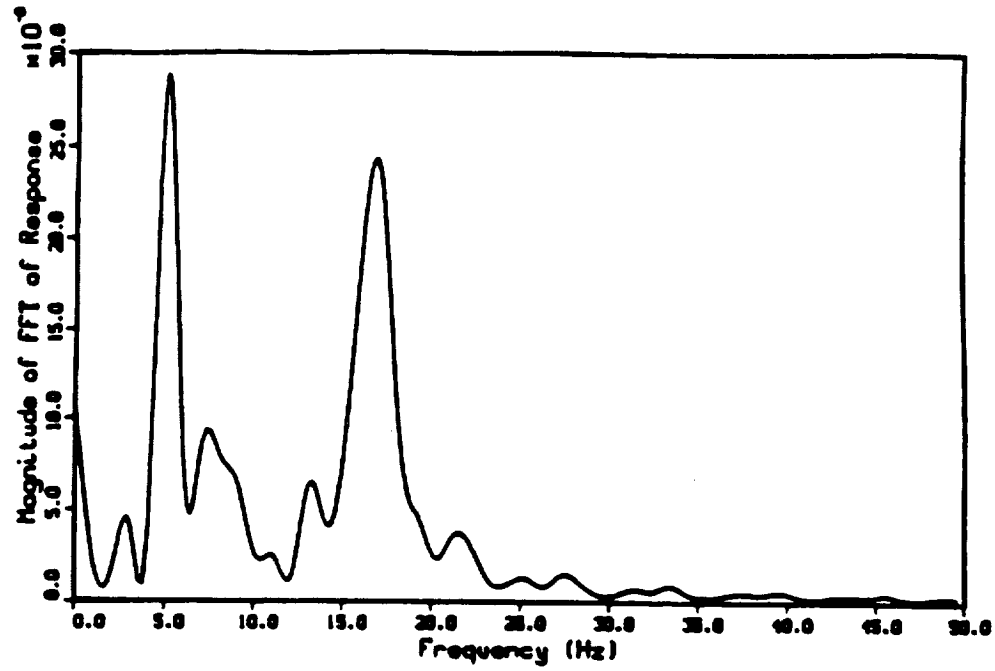


(*a*) 2nd mode.

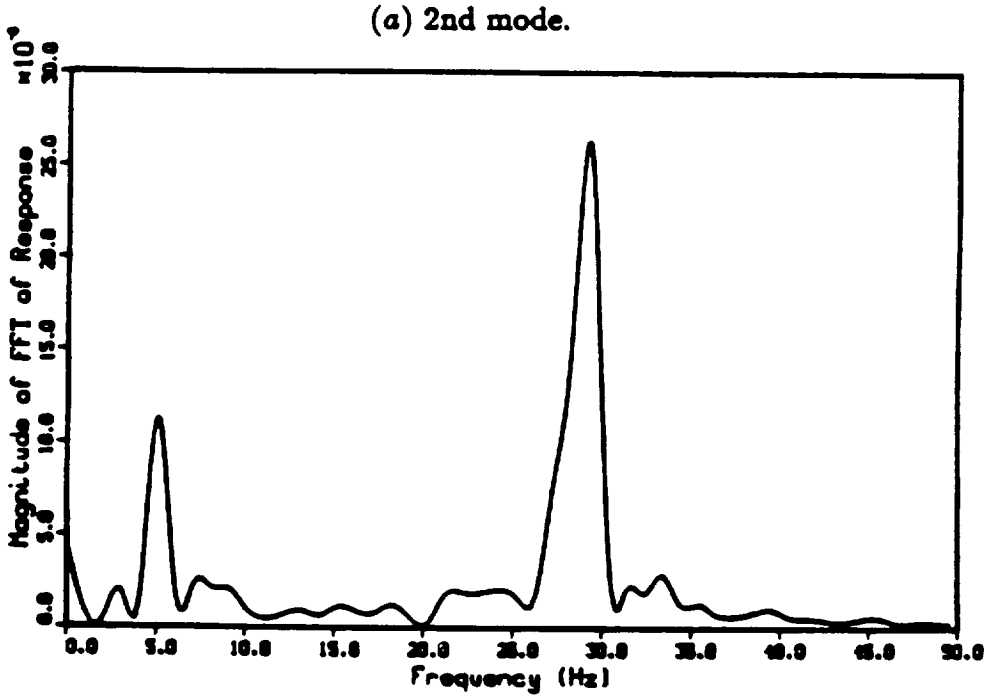


(*b*) 3rd mode.

Figure 6.30: Frequency content of the modal response of an Atlas-Able IV vehicle at dynamic pressure $q_D = 400$ psf .

ORIGINAL PAGE IS
OF POOR QUALITY

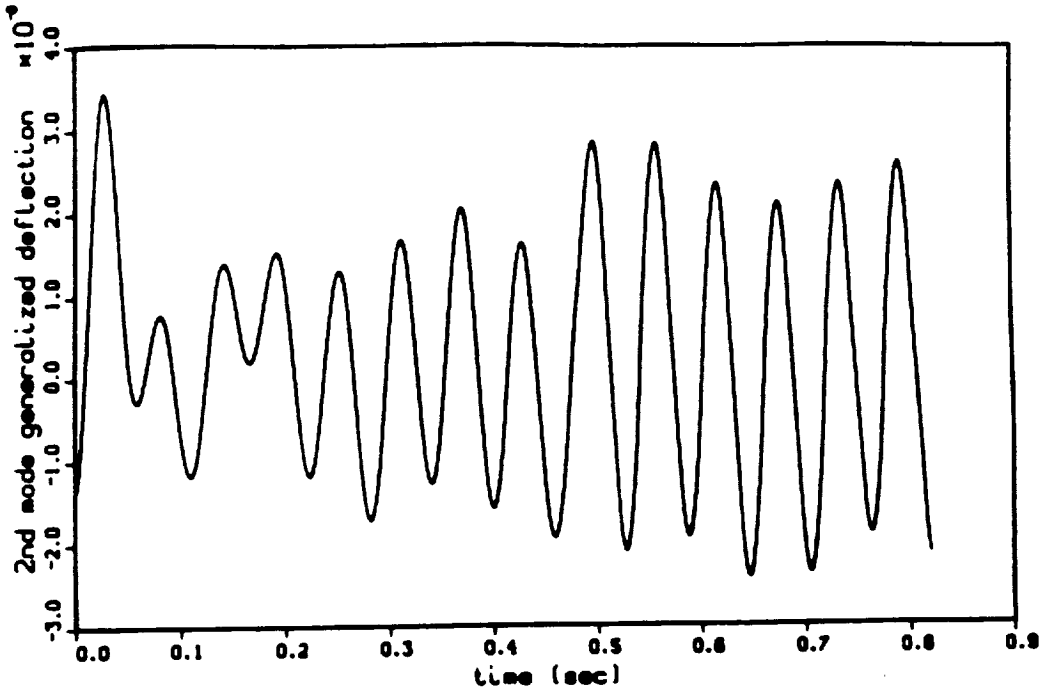


Figure 6.31: Filtered second mode response for Atlas-Able IV vehicle.

second mode, however, the filtered response clearly indicates the growing amplitude of oscillation. The latter is shown in Figure 6.31 .

As we have seen from the results of the previous section, it is also interesting to look at the modal generalized forces. These are shown in Figure 6.32 . There is no surprise that the forces follow the first mode deflection, since the overall vehicle deformation is almost completely determined by the first mode. It can be observed that there is very little phase lag between the motion and the aerodynamic forces. Figure 6.33 shows the aerodynamic load distribution along the body for several instants during the oscillation. Since, again, the first mode amplitude dominates the other ones, we used the first mode generalized coordinate as the total deflection amplitude when selecting at which instant of time we would sample the running normal force. Essentially, Figure 6.33 is showing that most of the load is located at the vehicle elliptical nose for the zero angle of attack case. This explains why the magnitudes of the generalized forces are so similar, since the mode shapes are similar to one another for that body region (see, for instance, Figure 6.16).

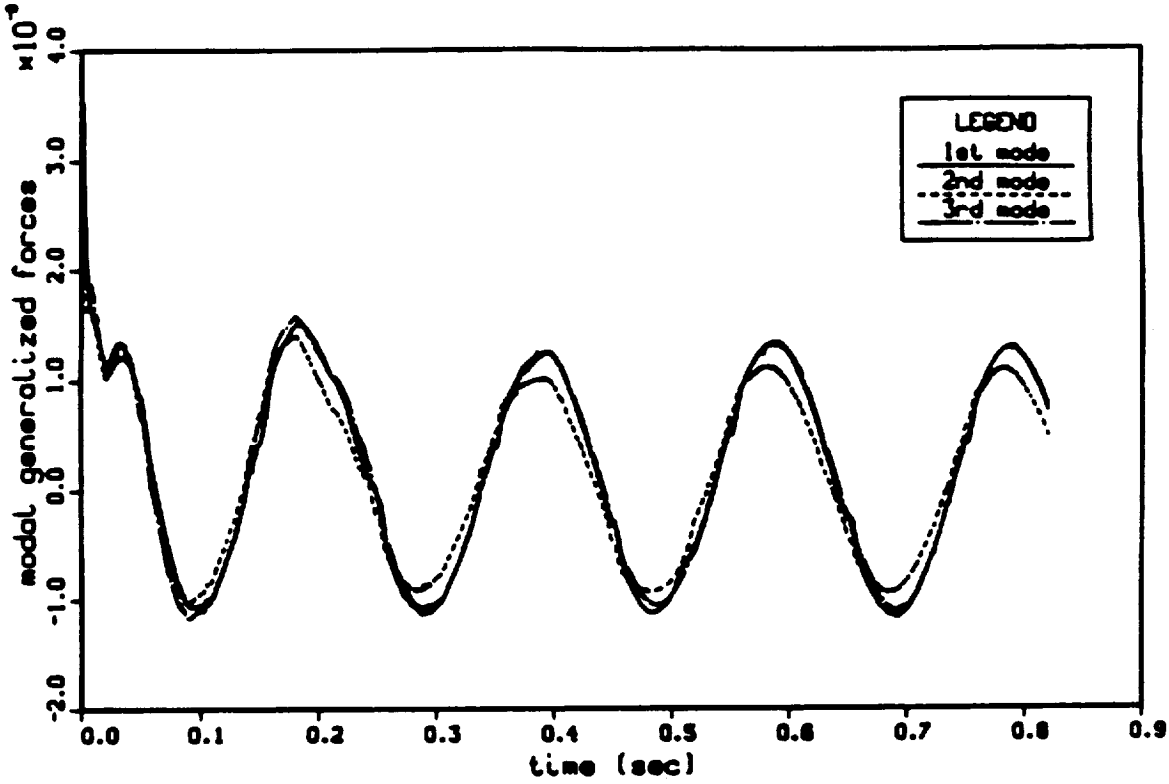


Figure 6.32: Modal generalized forces on Atlas-Able IV at $M_\infty = 0.85$ , $\alpha = 0°$ and $q_D = 400$ psf .

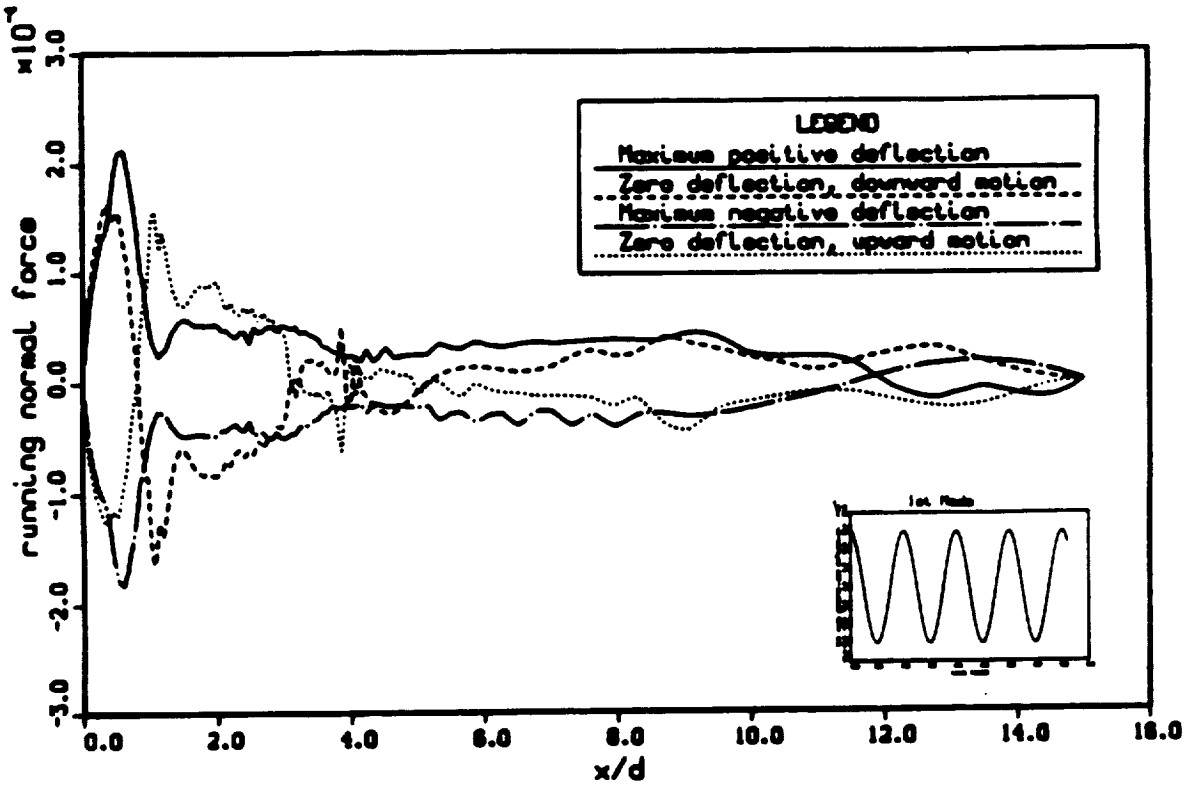


Figure 6.33: Unsteady aerodynamic load distribution on Atlas-Able IV at various points along the first mode oscillation.

ORIGINAL PAGE IS
OF POOR QUALITY

Finally, as we mentioned before, the second mode was expected to become aeroelastically unstable, according to results presented on Reference [4] . For the zero angle of attack case, our computational results are capturing the instability appropriately, as evidenced by the foregoing analysis. It is also interesting to note that our predictions regarding the proneness of the smaller angle of attack situations to aeroelastic instability were confirmed by the results. Despite the fact that our calculations at the 6° angle of attack condition assumed nonzero structural damping coefficients, we saw that at 400 psf dynamic pressure the airstream was still contributing positive damping. On the other hand, an unstable solution is obtained at zero angle of attack for the same dynamic pressure. So, at least qualitatively, our computations are predicting the correct behavior in the cases analyzed.

# Chapter 7

# Conclusions

## 7.1 Summary

The idea of using computational fluid dynamics techniques for aeroelastic analysis in the transonic regime of flight is not new. Several of the references cited throughout this text substantiate this statement. In this context, the contributions of the present work are associated with the use of the three-dimensional unsteady pressible Navier-Stokes equations for the flow simulation and aeroelastic analysis of realistic 3-D body configurations. It is a substantial departure from past investigations, where a potential formulation was commonly used to solve the aerodynamic problem or where only two-dimensional flows were considered.

The present research initially studied a hemisphere-cylinder configuration. Steady state, as well as unsteady aerodynamic, results for this geometry were presented and discussed. The steady state results showed good agreement either with existing experimental information or with data obtained from other comparable CFD codes. They provided good insight into the code's behavior for both subsonic and supersonic freestream conditions. No aeroelastic cases were investigated for the hemisphere-cylinder. On the other hand calculations for forced rigid body oscillations were performed, wi ..1 the primary objective of acquiring a better understanding of the parameters involved in these unsteady computations.

The unsteady airloads due to this forced, sinusoidal rigid body oscillation could

not be compared to any results in the literature because we were unable to locate similar experimental investigations. To the author's knowledge, this was the first attempt to capture the unsteady behavior of such a configuration undergoing sinusoidal pitching oscillations using a Navier-Stokes formulation. Happily, the unsteady calculations reproduced the expected flow features. Due to time constraints, however, we refrained from studying cases at lower reduced frequencies which probably would be more representative of actual flight conditions.

The study of a general hammerhead payload provided further confidence in the code developed by producing physically reasonable results for a transonic flow condition. Hammerhead vehicles are by no means simple geometries for computational simulation, because some form of flow separation is usually associated with the presence of a boattail in the forebody. This is in addition to the shock-induced separation due to the transonic shock impingement on the body surface. The steady state aerodynamic results reproduced the expected flow features. The aeroelastic calculations showed that the first configuration studied was free from instability at the flight conditions considered.

The stable aeroelastic behavior of this vehicle can be explained by the existence of a *longer* hammerhead section, i. e. , a longer cylindrical forebody region. It prevents the merging of the two separation regions mentioned above, therefore resulting in a milder unsteady aerodynamic environment. This observation agrees with existing empirical rules for the design of hammerhead payloads. Besides the physical considerations of aeroelastic stability of this configuration, its study was instrumental in developing the details of the structural-dynamic portion of the code. A more appropriate assessment of the computational requirements for aeroelastic analysis was possible, and acceptable time step levels could be selected.

For the Atlas-Able IV vehicle, steady state wind tunnel pressure coefficient distributions were available in the literature for various tunnel conditions in the transonic regime. Actual in flight transonic aeroelastic stability information was also available, as well as the results of semi-empirical analyses. The details of the exact flight conditions encountered were, unfortunately, rather sketchy. The configuration was studied at two different angles of attack, and for each flight condition the

dynamic pressure was the parameter varied in the search for the stability boundary.

The steady state results compared well with experiment, except that a better computational resolution of the shock region would be desirable. In the process of performing these calculations, some numerical difficulties with the present flow solver were uncovered. The artificial dissipation algorithm used showed some limitations in the sense that, in order to maintain numerical stability, the required magnitude of this parameter was already interfering with the physics of the flow. The turbulence model employed proved very sensitive to some of its parameters, producing a wide variety of flow topologies for the same flight condition when the only thing varied was the distance of the search for the maximum velocity in the boundary layer profile.

This last observation can probably be explained by the fact that the kind of massively separated flows which occur in this case may exceed what the turbulence model was originally derived for. A discussion of the possibilities for further upgrading the current flow solver algorithm will be presented in the next section. While on the subject of flow solutions, it must be said that the availability of a good graphics post-processing package is absolutely essential for interpretation and understanding of these three dimensional CFD calculations. The study of body pressure distributions only, even though important, is not enough to ensure that the correct solution is being obtained. A very good example was seen in the numerical experiments performed with the turbulence model parameters.

The aeroelastic calculations reproduced the known Atlas-Able IV results qualitatively very well. The second mode instability [4] was clearly observed at zero angle of attack and $M_\infty = 0.85$ . At an angle of attack of 6 degrees and the same freestream Mach number, no unstable aeroelastic behavior was predicted. However, the second mode again showed some tendency of becoming unstable for some portion of the dynamic pressure range investigated. The instability, when it occurs, is certainly a one degree of freedom phenomenon. The frequency of the response in each mode remains approximately unchanged, regardless of the variations in dynamic pressure.

The Atlas-Able IV configuration has a much shorter cylindrical forebody section than the first hammerhead configuration analyzed, which explains the merged

separation. As previously discussed, in these cases the shock-induced separated region merges with the flow separation due to the adverse pressure gradients at the boattail. The result, in terms of vehicle stability, is that the possibility is created of larger lags in the airloads with respect to the motion. Therefore, the risk of aeroelastic instability is increased. As extensively discussed in the previous chapter, the computational results also confirmed the prediction that the smaller angle of attack cases would be more susceptible to instability. However, despite the good qualitative agreement, improvements in the aerodynamic solver and more accurate structural data are still necessary for a quantitative prediction of flutter speeds by means of the present method.

The CPU time per iteration for aeroelastic analysis is only 20% higher than for steady state aerodynamic calculations. The time spent on purely structural-dynamic calculations in the present implementation is, however, truly negligible. All the computational time increase is associated with the need to regenerate the grid at every time step when performing aeroelastic calculations. Typically, approaches based on modal analysis will spend almost negligible time on the solution of the structural-dynamic equations. On the other hand, if the vehicle is represented by some finite element model, this time is certainly bound to increase.

It must be emphasized that the increase in overall system time per iteration is much higher for aeroelastic than for purely aerodynamic examples. Since the database is not core contained, some rather extensive I/O is required every iteration even in steady state calculations. Use of asynchronous I/O allows an efficiency of 60% for pure aerodynamic computations. Efficiency here is being measured as the ratio of CPU time to overall system time. For aeroelastic analyses, however, the code efficiency is reduced to only 30% , because of the considerable increase in the input/output required per iteration. These efficiency figures are, of course, very machine dependent. The discussion here applies only for the Cyber 205 , although other machines may experience similar trends for databases that are not core-contained.

It is true that the computational requirements for using of the present method are still quite high. However, considering recent improvements in hardware as well

as numerical methods, it is fair to say that we are getting very close to acceptable levels. On the the storage side, i. e. , in terms of the internal memory required, environments such as the Cray 2 supercomputer completely eliminate the need for *out-of-core* temporary storage. Our requirements, which are for about 7 million words in the database plus a comparable amount for temporary arrays, can be considered small for a 256 *mega-words* core machine.

Since in most systems a problem of this size would require reads/writes to temporary files, the subject of computational time must be looked at on the two levels of CPU time and overall system time. There is no question that, as far as the latter is concerned, the optimum condition is obtained when everything is kept *in-core* . The problem with I/O sometimes can be minimized by intelligent structuring of the database and by streaming the flow of information in the code to take advantage of that. As the statistics given in the previous chapters show, the present code was successful in doing this for steady state problems. For aeroelastic analyses, however, the performance dropped considerably.

A reduction in actual CPU time can be accomplished either by faster flow solver algorithms or by faster machines. The search for faster and more reliable computational schemes is a continuing objective of CFD research. A breakthrough in terms of raw machine speed was realized with vectorization. More recently, some attention has been given to the approach of having a multi-processor[1] computer, where each processor could work on a portion of the program at the same time. An example of this technology is the ETA-10 system. It is worth pointing out that the pencil data structure used in the present work is very suitable for such multi-processor environments.

A discussion of possible extensions for the method is now presented. The main purpose is to relate the work done here with similar applications, which may involve even more complex configurations or flight conditions than the ones described in the preceding chapters. The aerodynamic formulation is very general. Actually, it is as general as one would require for the flight regime and vehicle types

[1]Note that the nomenclature may be misleading, since there are many machines which have more than one processor but do not have the capability we are describing here.

under consideration, except with respect to the representation of turbulence. The structural-dynamic formulation, however, has several assumptions which may seem quite restrictive at first. These assumptions are believed adequate for the physical situation being treated by the present work. Nevertheless, a user may be interested in generalizing this formulation.

If we assume that a modal approach would still be used, the major generalizations that could be incorporated would be to introduce rigid body degrees of freedom, to consider that the modes might be elastically or inertially coupled, and to allow for a full three dimensional beam type of behavior. The present theoretical formulation already allows for rigid body degrees of freedom. However, they were never implemented in the code, and a few programming changes would be required for their introduction.

If normal vibration modes are not known, i. e. , the modes to be used are coupled either elastically or inertially, the method can be easily extended. The difference would be that, instead of solving for each of the generalized coordinates separately, the solution would have to be done considering the (now) coupled system of equations. In terms of computational effort, this means that matrices would have to be inverted, as opposed to the solution of a number of scalar equations. One should note, however, that the number of structural modes considered in a typical aeroelastic analysis is extremely small compared to the size of the matrices involved in the solution of the aerodynamic problem. As a result, the overall computational cost of the solution should not be affected very much.

The aerodynamic formulation allows for arbitrarily large angles of attack, which includes cases where asymmetric separation may occur. It would be interesting to give to the structural-dynamic formulation the capability of handling the same flight condition. This would involve considering bending in two planes and possibly torsion of the body about its longitudinal axis. This extension is very straightforward in concept, although its programming may require some very careful thought.

On the other hand, if the current *low* angle of attack restrictions are kept for the structural-dynamic formulation, some simplifications can be incorporated in the flow solver. The computational grid used in all the calculations presented here is a 360°

mesh in the circumferential direction. The results presented in the earlier chapters show that the flow solutions obtained are symmetric with respect to the pitching plane. In other words, the pitching plane can be used as a plane of symmetry for the flow solution, and almost half of the grid points could be saved. This simplification would cut the complete database in half, and the savings in computational time would be much larger since this time increases nonlinearly with the size of matrices.

The use of an algebraic grid generation scheme proved to be appropriate for the applications in the present work. However, this may not be true if more complex geometries are considered. There are some hammerhead configurations with very steep boattail angles. In such cases, the approximation used here of letting the *normal* grid lines come into the body surface at angles slightly different from 90° may be inadequate. Although algebraic schemes could still be used for these cases, more care would have to be exercised to ensure that normal grid lines do come in normal to the body. Some launch vehicle configurations have fins, or strap-on boosters, or even cluster designs. For these cases, certainly more elaborate grid generation schemes would be required.

The procedure for locating the downstream boundary followed in the present approach was possible because all the physical phenomena of interest were happening at the forebody. If configurations like the ones mentioned above are under consideration, the loads on the afterbody may significantly influence the overall vehicle's aeroelastic behavior. The more appropriate strategy for those cases would be to introduce the body base into the computational domain. The downstream computational boundary would have to be moved a least one body length downstream. This would make the flow solution more complex, in the sense that mixing layers and base flows would appear in this downstream portion of the computational domain. However, since we are not interested in these phenomena as far as our aeroelastic analysis is concerned, they would have to be resolved only to the extent of avoiding significant inaccuracies in the aerodynamic loads on the body.

In conclusion, the method developed in the present work seems to be an attractive option for aeroelastic analyses of launch vehicles in the transonic phase of flight. In this regime, the usual linearized methods break down, and an approach

that would take into consideration the aerodynamic nonlinearities is required. The applications presented provide confidence in the method, but it is clear that some details still need improvement before the code could be used in a production environment. There are launch vehicles being currently designed (e. g. , a commercial Atlas/Centaur and the Titan IV series) which probably could benefit from the techniques presented here in terms of reducing design costs.

It should be kept in mind that in the recent years there has been a substantial reduction in the cost of computation, whereas experiments are still very expensive. It is the author's belief that, eventually, computational procedures like the one proposed here will be capable of full integration into the design process. Thus, they may permit a more rational aeroelastic design instead of the usual *fixes* that characterized the aeroelastic clearance of flight vehicles over the years.

## 7.2 Recommendations for Future Work

The applications presented throughout the work exemplify the capabilities of the method. Despite the good qualitative agreement of the present results with existing data, it was clear that further consideration of a few computational problems was still necessary. The difficulties encountered with the artificial dissipation model deserve a more careful examination. For instance, a comparison of the magnitudes of the eddy viscosity coefficient and of the amount of artificial dissipation being introduced would be instructive. Moreover, the question left answered in the present work of why we are being forced to use such large amounts of artificial dissipation in order to keep the scheme stable should be resolved.

A possible solution to this problem might simply be that a more elaborate artificial dissipation scheme is necessary. Recent versions of the ARC3D code[52] have a nonlinear numerical dissipation model. The amount of artificial dissipation introduced at each computational point is weighted by a spectral radius scaling, which is a sum of the spectral radii of the Jacobian matrices. This model produces better results, and it may be helpful for solving the difficulties encountered by our present code with respect to artificial dissipation.

The foregoing discussion assumes, however, that the Beam and Warming approximate factorization scheme[67] will continue to be used. This does not have to be true. Recent so-called *upwind* schemes eliminate the need to explicitly introduce artificial dissipation into the scheme. The numerical dissipation is already built into the scheme by the way the governing equations are approximated by means of one-sided difference formulas. The replacement of the current solver by these upwind schemes may be a possible form of improving the present code. Furthermore, so-called TVD schemes[79] are well known for having very good shock capturing features. A possible drawback is that these schemes may be slower than the Beam and Warming algorithm.

As we have seen, another point of serious concern was the turbulence model. Some work could be done in this area in order to enhance the present flow solver algorithm. The tradeoff used to be that more elaborate models, despite producing better results for some flow cases, still would not yield significant enough improvements in most cases to justify the increase in complexity and computational requirements. Recently, however, some turbulence models have been created (e. g. , the Johnson and King model[80]) which advance the numerical representation of turbulence with very little increase in computational costs.

Another enhancement to the present code could be accomplished by incorporating some self-adaptive grid techniques[81, 82] into the current algorithm. These techniques let the position of the grid points be driven by the solution, concentrating them on regions of higher flow gradients. The tradeoff usually involved is that, by positioning the grid points in some optimum way, fewer points are necessary for a given accuracy. Thus, a faster run time is achieved. On the other hand, time is consumed to *adapt* the grid, which increases the total run time. Since in the present approach the grid is being regenerated at every time step for aeroelastic analysis, we would only get the advantages of self-adaptive grid methods without paying the additional costs.

The subject of improved graphic capabilities for visualization of flow results has been extensively discussed in the literature. The author believes that the currently available packages (e. g. , PLOT3D, RIP, GAS, etc. ) are very useful for the

analysis of steady state aerodynamic results. When dealing with unsteady problems, however, the requirements are more stringent. Static colored figures are not enough, and one has to resort to animation techniques in order to comprehend fully all the phenomena involved. The amount of data that has to be stored and then shipped across the network in order to use the existing graphic and animation packages is tremendously large.

As a result, there is a tendency to settle for an analysis of modal generalized deflections, as we did here, or some integrated aerodynamic quantity. Although these are important too, there is much more information being generated by the computation that is never studied because of the lack of practical ways of displaying it. For instance, a visualization of how the flow topology is modified as the body oscillates might be very helpful for understanding the mechanism behind a possible aeroelastic instability. Although the necessary tools for these visualizations exist today, their use is still so time consuming as to discourage a more widespread utilization.

The current trends in launch capabilities have given rise to a renewed interest in expendable launch vehicles. As discussed above, hammerhead payload configurations will certainly be under consideration. This fact should provide enough motivation for the continuing development of aeroelastic analysis techniques like the one presented here. Furthermore, it should also provide plenty of experimental data that could be used to validate these techniques and to guide their development.

# Appendix A

# Jacobian Matrices

The three-dimensional, inviscid flux Jacobian matrices in generalized curvilinear coordinates are given by

$$\hat{A} \text{ or } \hat{B} \text{ or } \hat{C} = \begin{bmatrix} \kappa_t & \kappa_x & \kappa_y & \kappa_z & 0 \\ \kappa_x\phi^2 - u\theta & \kappa_t + \theta - \kappa_x(\gamma-2)u & \kappa_y u - \kappa_x(\gamma-1)v & \kappa_z u - \kappa_x(\gamma-1)w & \kappa_x(\gamma-1) \\ \kappa_y\phi^2 - v\theta & \kappa_x v - \kappa_y(\gamma-1)u & \kappa_t + \theta - \kappa_y(\gamma-2)v & \kappa_z v - \kappa_y(\gamma-1)w & \kappa_y(\gamma-1) \\ \kappa_z\phi^2 - w\theta & \kappa_x w - \kappa_z(\gamma-1)u & \kappa_y w - \kappa_z(\gamma-1)v & \kappa_t + \theta - \kappa_z(\gamma-2)w & \kappa_z(\gamma-1) \\ \theta(2\phi^2 - \gamma e\rho^{-1}) & \kappa_x(\gamma e\rho^{-1} - \phi^2) - (\gamma-1)u\theta & \kappa_y(\gamma e\rho^{-1} - \phi^2) - (\gamma-1)v\theta & \kappa_z(\gamma e\rho^{-1} - \phi^2) - (\gamma-1)w\theta & \kappa_t + \gamma\theta \end{bmatrix} \tag{A.1}$$

where

$$\begin{aligned} \theta &= \kappa_x u + \kappa_y v + \kappa_z w \\ \phi^2 &= \frac{1}{2}(\gamma-1)\left(u^2 + v^2 + w^2\right) \end{aligned}$$

Here $\kappa = \xi$, $\eta$ or $\zeta$ for $\hat{A}$, $\hat{B}$ or $\hat{C}$, respectively.

## APPENDIX A. JACOBIAN MATRICES

The viscous flux Jacobian matrices are obtained from

$$\hat{M}_\kappa = \begin{bmatrix} 0 & 0 & 0 & 0 & 0 \\ m_{21} & \alpha_1\delta_\kappa(\rho^{-1}) & \alpha_2\delta_\kappa(\rho^{-1}) & \alpha_3\delta_\kappa(\rho^{-1}) & 0 \\ m_{31} & \alpha_2\delta_\kappa(\rho^{-1}) & \alpha_4\delta_\kappa(\rho^{-1}) & \alpha_5\delta_\kappa(\rho^{-1}) & 0 \\ m_{41} & \alpha_3\delta_\kappa(\rho^{-1}) & \alpha_5\delta_\kappa(\rho^{-1}) & \alpha_6\delta_\kappa(\rho^{-1}) & 0 \\ m_{51} & m_{52} & m_{53} & m_{54} & \alpha_0\delta_\kappa(\rho^{-1}) \end{bmatrix} \tag{A.2}$$

where

$$\begin{aligned}
m_{21} &= -\alpha_1\delta_\kappa(u/\rho) - \alpha_2\delta_\kappa(v/\rho) - \alpha_3\delta_\kappa(w/\rho) \\
m_{31} &= -\alpha_2\delta_\kappa(u/\rho) - \alpha_4\delta_\kappa(v/\rho) - \alpha_5\delta_\kappa(w/\rho) \\
m_{41} &= -\alpha_3\delta_\kappa(u/\rho) - \alpha_5\delta_\kappa(v/\rho) - \alpha_6\delta_\kappa(w/\rho) \\
m_{51} &= -\alpha_0\delta_\kappa\left[\left(e/\rho^2\right) - \left(u^2+v^2+w^2\right)/\rho\right] \\
&= -\alpha_1\delta_\kappa\left(u^2/\rho\right) - \alpha_4\delta_\kappa\left(v^2/\rho\right) - \alpha_6\delta_\kappa\left(w^2/\rho\right) \\
&= -2\alpha_2\delta_\kappa(uv/\rho) - 2\alpha_3\delta_\kappa(uw/\rho) - 2\alpha_5\delta_\kappa(vw/\rho) \\
m_{52} &= -\alpha_0\delta_\kappa(u/\rho) - m_{21} \\
m_{53} &= -\alpha_0\delta_\kappa(v/\rho) - m_{31} \\
m_{54} &= -\alpha_0\delta_\kappa(w/\rho) - m_{41} \\
\alpha_0 &= \gamma\left(Pr^{-1} + \tilde{\mu}_t Pr_t^{-1}\right)\left(\kappa_x^2+\kappa_y^2+\kappa_z^2\right) \\
\alpha_1 &= (1+\tilde{\mu}_t)\left(\frac{4}{3}\kappa_x^2+\kappa_y^2+\kappa_z^2\right) \\
\alpha_2 &= \frac{1}{3}(1+\tilde{\mu}_t)\kappa_x\kappa_y \\
\alpha_3 &= \frac{1}{3}(1+\tilde{\mu}_t)\kappa_x\kappa_z \\
\alpha_4 &= (1+\tilde{\mu}_t)\left(\kappa_x^2+\frac{4}{3}\kappa_y^2+\kappa_z^2\right) \\
\alpha_5 &= \frac{1}{3}(1+\tilde{\mu}_t)\kappa_y\kappa_z \\
\alpha_6 &= (1+\tilde{\mu}_t)\left(\kappa_x^2+\kappa_y^2+\frac{4}{3}\kappa_z^2\right)
\end{aligned}$$

As in the inviscid case, $\kappa = \xi$, $\eta$ or $\zeta$ for $\hat{M}_\xi$, $\hat{M}_\eta$ or $\hat{M}_\zeta$, respectively. Furthermore, we remind the reader that all variables in these expressions are dimensionless. In particular, $\tilde{\mu}_t = \mu_t/\mu_\infty$, where $\mu_\infty$ is the freestream (laminar) viscosity coefficient.

# Appendix B

# Periodic Tridiagonal Solver

A periodic, block tridiagonal matrix has the general form

$$\mathcal{A} = \begin{bmatrix} B_1 & C_2 & 0 & \cdots & 0 & A_0 \\ A_1 & B_2 & C_3 & \cdots & 0 & 0 \\ 0 & A_2 & B_3 & \ddots & \vdots & \vdots \\ \vdots & 0 & A_3 & \ddots & C_{n-1} & 0 \\ 0 & \vdots & \vdots & \ddots & B_{n-1} & C_n \\ C_{n+1} & 0 & 0 & \cdots & A_{n-1} & B_n \end{bmatrix} \tag{B.1}$$

For the present application, each element in $\mathcal{A}$ is a $5 \times 5$ matrix. However, there is another "dimension" to $\mathcal{A}$, which we are not showing here. Since the domain of calculation is a parallelepiped in computational space, we actually operate in a whole plane of data when performing the solution in a certain direction. This other dimension of $\mathcal{A}$, which one may call its "depth", is equal to the number of grid points in this plane. The reader should also realize that we are using a somewhat loose nomenclature by calling these entities "matrices". They would be (more appropriately) referred to as multi-dimensional arrays.

It is instructive to think in terms of matrices because they are easier to represent. Furthermore, for each point in this grid plane (or grid surface, if one thinks in terms of the physical space), the finite difference equations are matrix relations. On the other hand, it is important to remember that we are solving for a whole data plane

at once, since the storage requirements are determined by the size of the resulting multi-dimensional arrays.

The process of inversion involves an L-U decomposition of matrix $\mathcal{A}$, such that

$$\mathcal{A} = \mathcal{L}\mathcal{U} \tag{B.2}$$

where

$$\mathcal{L} = \begin{bmatrix} L_1 & 0 & 0 & \cdots & 0 & 0 \\ M_1 & L_2 & 0 & \cdots & 0 & 0 \\ 0 & M_2 & L_3 & \ddots & \vdots & \vdots \\ \vdots & \vdots & M_3 & \ddots & 0 & 0 \\ 0 & 0 & \vdots & \ddots & L_{n-1} & 0 \\ N_1 & N_2 & \cdots & N_{n-2} & M_{n-1} & L_n \end{bmatrix} \tag{B.3}$$

$$\mathcal{U} = \begin{bmatrix} I & U_2 & 0 & \cdots & 0 & V_1 \\ 0 & I & U_3 & \cdots & 0 & V_2 \\ 0 & 0 & I & \ddots & \vdots & \vdots \\ 0 & 0 & 0 & \ddots & U_{n-1} & V_{n-2} \\ \vdots & \vdots & \vdots & \ddots & I & U_n \\ 0 & 0 & 0 & \cdots & 0 & I \end{bmatrix} \tag{B.4}$$

Here $I$ is the identity matrix.

In order to present the algorithm for solution adopted in the present work, we will assume that the solution for a system of the form

$$\mathcal{A}X = Y \tag{B.5}$$

is being sought. Furthermore, we will call the intermediate result

$$\overline{X} = \mathcal{U}X = \mathcal{L}^{-1}Y$$

where

$$X = \begin{Bmatrix} x_1 \\ x_2 \\ \vdots \\ x_n \end{Bmatrix} \qquad Y = \begin{Bmatrix} y_1 \\ y_2 \\ \vdots \\ y_n \end{Bmatrix} \qquad \overline{X} = \begin{Bmatrix} \overline{x}_1 \\ \overline{x}_2 \\ \vdots \\ \overline{x}_n \end{Bmatrix}$$

## *APPENDIX B. PERIODIC TRIDIAGONAL SOLVER*

The solution algorithm can be written as follows:

Forward sweep

- First element ($i = 1$):

$$\begin{aligned} L_1 &= B_1 \\ M_1 &= A_1 \\ N_1 &= C_{n+1} \\ \mathbf{x}_1 &= L_1^{-1} y_1 \\ V_1 &= L_1^{-1} A_0 \\ T_a &= N_1 V_1 \end{aligned}$$

- For $i = 2$ until $n - 2$ :

$$\begin{aligned} U_i &= L_{i-1}^{-1} C_i \\ L_i &= B_i - M_{i-1} U_i \\ M_i &= A_i \\ N_i &= -N_{i-1} U_i \\ \mathbf{x}_i &= L_i^{-1} (y_i - M_{i-1} \mathbf{x}_{i-1}) \\ V_i &= -L_i^{-1} M_{i-1} V_{i-1} \\ T_a &= T_a + N_i V_i \end{aligned}$$

- Next-to-last element ($i = n - 1$):

$$\begin{aligned} U_i &= L_{i-1}^{-1} C_i \\ L_i &= B_i - M_{i-1} U_i \\ M_i &= A_i - N_{i-1} U_i \\ \mathbf{x}_i &= L_i^{-1} (y_i - M_{i-1} \mathbf{x}_{i-1}) \\ T_b &= M_{i-1} V_{i-1} \end{aligned}$$

- Last element ($i = n$):

$$\begin{aligned} U_n &= L_{n-1}^{-1}(C_n - T_b) \\ T_s &= T_s + M_{n-1}U_n \\ L_n &= B_n - T_s \\ \overline{x}_n &= L_n^{-1}(y_n - M_{n-1}\overline{x}_{n-1}) \end{aligned}$$

Backward sweep

- Last and next-to-last elements:

$$\begin{aligned} x_n &= \overline{x}_n \\ x_{n-1} &= \overline{x}_{n-1} - U_n x_n \end{aligned}$$

- For $i = n - 2$ until 1 :

$$x_i = \overline{x}_i - U_{i+1}x_{i+1} - V_i x_n$$

As the expressions above show, only the arrays required for the backward sweep have to be completely stored. At a given point along the forward sweep, only the arrays in the current "column" of $\mathcal{L}$ and in the preceding one are needed. All information prior to that can be discarded. Furthermore, the arrays in $\mathcal{A}$ are generated as they are needed during the forward sweep. In summary, care is exercised in order to reduce the storage requirements to a minimum. Further reduction in storage space could only be achieved at costly penalties to the computational time, since it would involve regenerating portions of $\mathcal{U}$ during the backward sweep.

# Bibliography


[1] Landahl, M.T., Unsteady Transonic Flow , Pergamon Press, 1961.

[2] Ballhaus, W.F, and Goorjian, P.M., *Computation of Unsteady Transonic Flows by the Indicial Method*, AIAA Journal, Vol. 16, No. 2, Feb. 1978, pp. 117-124.

[3] Nixon, D., *Notes on the Transonic Indicial Method*, AIAA Journal, Vol. 16, No. 6, June 1978, pp. 613-616.

[4] Woods, P., and Ericsson, L.E., *Aeroelastic Considerations in a Slender, Blunt-Nose, Multistage Rocket*, Aerospace Engineering, May 1962.

[5] Ericsson, L.E., and Reding, J.P., *Fluid Dynamics of Unsteady Separated Flow. Part I. Bodies of Revolution*, Prog. Aerospace Sci., Vol. 23, 1986, pp. 1-84.

[6] Rainey, A.G., *Progress on the Launch-Vehicle Buffeting Problem*, Journal of Spacecraft and Rockets, Vol. 2, No. 3, May-June 1965, pp. 289-299.

[7] Försching, H., *Introductory Survey of Aeroelastic Problems in Separated and Transonic Flow*, In: Unsteady Airloads and Aeroelastic Problems in Separated and Transonic Flow, Lecture Series 1981-4, Von Karman Institute for Fluid Dynamics, Rhode-Saint-Genese, Belgium, March 1981.

[8] Försching, H., *Aeroelastic Buffeting Prediction Techniques - A General Review*, In: Unsteady Airloads and Aeroelastic Problems in Separated and Transonic Flow, Lecture Series 1981-4, Von Karman Institute for Fluid Dynamics, Rhode-Saint-Genese, Belgium, March 1981.

[9] Jones, J.G., *Dynamic Response of Aircraft with Fluctuating Flow Fields*, In: Unsteady Airloads and Aeroelastic Problems in Separated and Transonic Flow, Lecture Series 1981-4, Von Karman Institute for Fluid Dynamics, Rhode-Saint-Genese, Belgium, March 1981.

[10] Mabey, D.G., *Some Remarks on Buffeting*, In: Unsteady Airloads and Aeroelastic Problems in Separated and Transonic Flow, Lecture Series 1981-4, Von Karman Institute for Fluid Dynamics, Rhode-Saint-Genese, Belgium, March 1981.

[11] Ashley, H., Lehman, L.L., and Nathman, J.K., *The Constructive Uses of Aeroelasticity*, AIAA Paper No. 80-0877, presented at the AIAA International Annual Meeting and Technical Display, Baltimore, Maryland, May 6-11, 1980 (also published in SUDAAR No. 529, Department of Aeronautics and Astronautics, Stanford University, 1982).

[12] Peterson, V.L., *Trends in Computational Capabilities for Fluid Dynamics*, AGARD-CP-374, Transonic Unsteady Aerodynamics and its Aeroelastic Applications, January 1985.

[13] McCroskey, W.J., Kutler, P., and Bridgeman, J.O., *Status and Prospects of Computational Fluid Dynamics for Unsteady Transonic Viscous Flows*, AGARD-CP-374, Transonic Unsteady Aerodynamics and its Aeroelastic Applications, January 1985.

[14] Ballhaus, W.F., and Goorjian, P.M., *Implicit Finite-Difference Computations of Unsteady Transonic Flow About Airfoils*, AIAA Journal, Vol. 15, No. 12, Dec. 1977, pp. 1728-1735.

[15] Houwink, R., and Van der Vooren, J., *Results of an Improved Version of LTRAN2 for Computing Unsteady Airloads on Airfoils Oscillating in Transonic Flow*, AIAA Paper 79-1553, AIAA 12th Fluid and Plasma Dynamics Conference, Williamsburg, Virginia, July 1979.

[16] Goorjian, P.M., *Implicit Computations of Unsteady Transonic Flow Governed by the Full Potential Equation in Conservation Form*, AIAA Paper 80-0150, AIAA 18th Aerospace Sciences Meeting, Pasadena, CA, January 1980.

[17] Yang, T.Y., Guruswamy, P., Striz, A.G., and Olsen, J.J., *Flutter Analysis of a NACA 64A006 Airfoil in Small Disturbance Transonic Flow*, Journal of Aircraft, Vol. 17, No. 4, April 1980, pp. 225-232.

[18] Bridgeman, J.O., Steger, J.L., and Caradonna, F.X., *A Conservative Finite Difference Algorithm for the Unsteady Transonic Potential Equation in Generalized Coordinates*, AIAA Paper 82-1388, AIAA 9th Atmospheric Flight Mechanics Conference, San Diego, CA, August 1982.

[19] Edwards, J.W., Bland, S.R., and Seidel, D.A., *Experience with Transonic Unsteady Aerodynamic Calculations*, NASA TM-86278, August 1984.

[20] Guruswamy, P., and Goorjian, P.M., *Computations and Aeroelastic Applications of Unsteady Transonic Aerodynamics About Wings*, Journal of Aircraft, Vol. 21, No. 1, Jan. 1984, pp. 37-43.

[21] Malone, J.B., and Sankar, N.L., *Application of a Three-Dimensional Steady and Unsteady Full Potential Method for Transonic Flow Computations*, AFWAL-TR-84-3011, June 1984.

[22] Isogai, K., *The Development of Unsteady Transonic 3-D Full Potential Code and its Aeroelastic Applications*, AGARD-CP-374, Transonic Unsteady Aerodynamics and its Aeroelastic Applications, January 1985.

[23] Goorjian, P.M., and Guruswamy, G.P., *Unsteady Transonic Aerodynamic and Aeroelastic Calculations About Airfoils and Wings*, AGARD-CP-374, Transonic Unsteady Aerodynamics and its Aeroelastic Applications, January 1985.

[24] Guruswamy, G.P., and Goorjian, P.M., *Efficient Algorithm for Unsteady Transonic Aerodynamics of Low-Aspect-Ratio Wings*, Journal of Aircraft, Vol. 22, No. 3, March 1985, pp. 193-199.

[25] Bennett, R.M., Seidel, D.A., and Sandford, M.C., *Transonic Calculations for a Flexible Supercritical Wing and Comparison with Experiment*, AIAA Paper 85-0665, AIAA 26th Structures, Structural Dynamics and Materials Conference, Orlando, April 1985.

[26] Batina, J.T., *Unsteady Transonic Flow Calculations for Two-Dimensional Canard-Wing Configurations with Aeroelastic Applications*, AIAA Paper 85-0585, AIAA 26th Structures, Structural Dynamics and Materials Conference, Orlando, April 1985.

[27] Guruswamy, G.P., Goorjian, P.M., and Tu, E.L., *Transonic Aeroelasticity of Wings with Tip Stores*, AIAA Paper 86-1007, AIAA/ASME/ASCE/AHS 27th Structures, Structural Dynamics and Materials Conference, San Antonio, Texas, May 19-21, 1986.

[28] Guruswamy, G.P., Goorjian, P.M., Ide, H., and Miller, G.D., *Transonic Aeroelastic Analysis of the B-1 Wing*, Journal of Aircraft, Vol. 23, No. 7, July 1986, pp. 547-553.

[29] Ide, H., and Shankar, V.J., *Applications of a Fast, Time Accurate Full Potential Scheme to a Statically Flexible Wing in the Transonic Regime*, AIAA Paper 87-0707, AIAA/ASME/ASCE/AHS 28th Structures, Structural Dynamics and Materials Conference, Monterey, CA, April 6-8, 1987.

[30] Guruswamy, G.P., Tu, E.L., and Goorjian, P.M., *Transonic Aeroelasticity of Wings with Active Control Surfaces*, AIAA Paper 87-0709, AIAA/ASME/ASCE/AHS 28th Structures, Structural Dynamics and Materials Conference, Monterey, CA, April 6-8, 1987.

[31] Steger, J.L., and Bailey, H.E., *Calculation of Transonic Aileron Buzz*, AIAA Journal, Vol. 18, No. 3, March 1980, pp. 249-255.

[32] Salmond, D.J., *Calculation of Harmonic Aerodynamic Forces on Aerofoils and Wings from the Euler Equations*, AGARD-CP-374, Transonic Unsteady Aerodynamics and its Aeroelastic Applications, January 1985.

[33] Bendiksen, O.O., and Kousen, K.A., *Transonic Flutter Analysis Using the Euler Equations*, AIAA Paper 87-0911, AIAA Dynamics Specialists Conference, Monterey, CA, April 9-10, 1987.

[34] Hankey, W.L., Graham, J.E., and Shang, J.S., *Navier-Stokes Solution of a Slender Body of Revolution at Incidence*, AIAA Journal, Vol. 20, No. 6, June 1982, pp. 776-781.

[35] Nixon, D., *Prediction of Aeroelastic and Unsteady Aerodynamic Phenomena in Transonic Flow*, In: Unsteady Airloads and Aeroelastic Problems in Separated and Transonic Flow, Lecture Series 1981-4, Von Karman Institute for Fluid Dynamics, Rhode-Saint-Genese, Belgium, March 1981.

[36] Thompson, P.A., Compressible-Fluid Dynamics, McGraw-Hill, 1972.

[37] Liepmann, H.W., and Roshko, A., Elements of Gasdynamics, John Wiley & Sons, 1957.

[38] Anderson, D.A., Tannehill, J.C., and Pletcher, R.H., Computational Fluid Mechanics and Heat Transfer, McGraw-Hill, 1984.

[39] Hinze, J.O., Turbulence, 2nd Edition, McGraw-Hill, 1975.

[40] Deiwert, G.S., and Bailey, H.E., *Time-Dependent Finite-Difference Simulation of Unsteady Interactive Flows*, In: Numerical and Physical Aspects of Aerodynamic Flows II, T. Cebeci, ed. , Springer-Verlag, New York, 1984, pp. 63-78.

[41] Pulliam, T.H., Efficient Solution Method for the Navier-Stokes Equations , In: Numerical Techniques for Viscous Flow Computations in Turbomachinery Bladings, Lecture Series 1986-02, Von Karman Institute for Fluid Dynamics, Rhode-Saint-Genese, Belgium, January 1986.

[42] Chaussee, D.S., and Pulliam, T.H., *Two-Dimensional Inlet Simulation Using a Diagonal Implicit Algorithm*, AIAA Journal , Vol. 19, No. 2, February 1981, pp. 153-159.

[43] Pulliam, T.H., and Chaussee, D.S., *A Diagonal Form of an Implicit Approximate-Factorization Algorithm*, Journal of Computational Physics, Vol. 39, 1981, pp. 347-363.

[44] Viviand, H., *Conservation Forms of the Gas Dynamics Equations*, Recherche Aerospatiale, Vol. 1, 1974, pp. 153-158.

[45] Vinokur, M., *Conservation Equations of Gas-Dynamics in Curvilinear Coordinate Systems*, Journal of Computational Physics, Vol. 14, 1974, pp. 105-125.

[46] Baldwin, B.S., and Lomax, H., *Thin Layer Approximation and Algebraic Model for Separated Turbulent Flows* , AIAA Paper No. 78-257, January 1978.

[47] Deiwert, G.S., *Supersonic Axisymmetric Flow over Boattails Containing a Centered Propulsive Jet*, AIAA Journal , Vol. 22, No. 10, Oct. 1984, pp. 1358-1365.

[48] Deiwert, G.S., Andrews, A.E., and Nakahashi, K., *Theoretical Analysis of Aircraft Afterbody Flows* , AIAA Paper 84-1524, AIAA 17th Fluid Dynamics, Plasma Dynamics, and Lasers Conference, Snowmass, Colorado, June 1984.

[49] Beam, R.M., and Warming, R.F., *An Implicit Finite-Difference Algorithm for Hyperbolic Systems in Conservation-Law Form*, Journal of Computational Physics, Vol. 22, 1976, pp. 87-110.

[50] Warming, R.F., and Beam, R.M., *On the Construction and Application of Implicit Factored Schemes for Conservation Laws*, SIAM-AMS Proceedings 11, 1978, pp. 85-129.

[51] Warming, R.F., Beam, R.M., and Hyett, B.J., *Diagonalization and Simultaneous Symmetrization of the Gas-Dynamic Matrices*, Mathematics of Computation, Vol. 29, No. 132, Oct. 1975, pp. 1037-1045.

[52] Pulliam, T.H., and Steger, J.L., *Recent Improvements in Efficiency, Accuracy and Convergence for Implicit Approximate Factorization Algorithms*, AIAA Paper 85-0360, AIAA 23rd Aerospace Sciences Meeting, Reno, Nevada, January 1985.

[53] Ying, S.X., *Three-Dimensional Implicit Approximately Factored Schemes for the Equations of Gasdynamics*, SUDAAR No. 557, Department of Aeronautics and Astronautics, Stanford University, June 1986. (Contract NCA 2-074, NASA Ames Research Center)

[54] Schlichting, H., Boundary Layer Theory, McGraw-Hill, 1955.

[55] Deiwert, G.S., and Rothmund, H., *Three-Dimensional Flow Over a Conical Afterbody Containing a Centered Propulsive Jet: A Numerical Simulation*, AIAA Paper 83-1709, AIAA 16th Fluid and Plasma Dynamics Conference, Danvers, Mass. , July 1983.

[56] Vinokur, M., *On One-Dimensional Stretching Functions for Finite-Difference Calculations*, NASA CR-3313, 1980.

[57] Deiwert, G.S., *Numerical Simulation of Three-Dimensional Boattail Afterbody Flowfields*, AIAA Journal, Vol. 19, No. 5, May 1981, pp. 582-588.

[58] Pulliam, T.H., and Steger, J.L., *Implicit Finite-Difference Simulations of Three-Dimensional Compressible Flow*, AIAA Journal, Vol. 18, No. 2, Feb. 1980, pp. 159-167.

[59] Bisplinghoff, R.L., Ashley, H., and Halfman, R.L., Aeroelasticity, Addison-Wesley, 1955.

[60] Bisplinghoff, R.L., and Ashley, H., Principles of Aeroelasticity, Dover, 1962.

[61] Meirovitch, L., Analytical Methods in Vibrations, Macmillan, 1967.

[62] Meirovitch, L., Elements of Vibration Analysis, 2nd Edition, McGraw-Hill, 1986.

[63] Dowell, E.H., *et al.* , A Modern Course in Aeroelasticity, Sijthoff & Noordhoff, 1978.

[64] Ashley, H., *Role of Shocks in the "Sub-Transonic" Flutter Phenomenon*, Journal of Aircraft, Vol. 17, No. 3, March 1980, pp. 187-197.

[65] Guruswamy, P., and Yang, T.Y., *Aeroelastic Time Response Analysis of Thin Airfoils by Transonic Code LTRAN2*, Computers and Fluids, Vol. 9, No. 4, 1981, pp. 409-425.

[66] Borland, C.J., and Rizzetta, D.P., *Nonlinear Transonic Flutter Analysis*, AIAA Journal, Vol. 20, No. 11, Nov. 1982, pp. 1606-1615.

[67] Beam, R.M., and Warming, R.F., *An Implicit Factored Scheme for the Compressible Navier-Stokes Equations*, AIAA Journal, Vol. 16, No. 4, April 1978, pp. 393-402.

[68] Ying, S.X., Steger, J.L., Schiff, L.B., and Baganoff, D., *Numerical Simulation of Unsteady, Viscous, High-Angle-of-Attack Flows Using a Partially Flux-Split Algorithm*, AIAA Paper 86-2179, AIAA 13th Atmospheric Flight Mechanics Conference, Williamsburg, Virginia, August 18-20, 1986.

[69] Hsieh, T., *An Investigation of Separated Flows About a Hemisphere-Cylinder at Incidence in the Mach Number Range from* 0.6 *to* 1.5, AIAA Paper 77-179, AIAA 15th Aerospace Sciences Meeting, Los Angeles, Calif. , January 1977.

[70] Hsieh, T., *Low Supersonic Flow over Hemisphere-Cylinder at Incidence*, Journal of Spacecraft and Rockets, Vol. 14, No. 11, Nov. 1977, pp. 662-668.

[71] Dallmann, U., *Topological Structures of Three-Dimensional Flow Separations*, DFVLR Report No. 221-82 A 07, April 1983.

[72] Dallmann, U., *Topological Structures of Three-Dimensional Vortex Flow Separation*, AIAA Paper No. 83-1735, AIAA 16th Fluid and Plasma Dynamics Conference, Danvers, Mass. , July 1983.

[73] Kaynak, Ü. , Holst, T.L., and Cantwell, B.J., *Computation of Transonic Separated Wing Flows Using an Euler/Navier-Stokes Zonal Approach*, NASA TM 88311, July 1986.

[74] Deiwert, G.S., *Topological Analysis of Computed Three-Dimensional Viscous Flow Fields*, in Recent Contributions to Fluid Mechanics, W. Haase, ed. , Springer-Verlag, New York, 1982, pp. 40-49.

[75] Graham, F.J., and Butler, C.B., *Static Pressure Distribution on a* 0.07*-Scale Aerodynamic Model of the Atlas-Able IV at Free-Stream Mach Numbers from* 0.50 *to* 1.60 , AEDC-TN-60-128, July 1960.

[76] Coe, C.F., *Steady and Fluctuating Pressures at Transonic Speeds on Two Space-Vehicle Payload Shapes*, NASA TM X-503, March 1961.

[77] Robinson, R.C., Wilcox, P.R., Gambucci, B.J., and George, R.E., *Dynamic Response of a Family of Axisymmetric Hammerhead Models to Unsteady Aerodynamic Loading*, NASA TN D-4504, June 1968.

[78] Zucrow, M.J., and Hoffman, J.D., Gas Dynamics, Vol. 1, John Wiley, 1976 (Table C.5, pp. 708-709).

[79] Harten, A., *A High Resolution Scheme for the Computation of Weak Solutions of Hyperbolic Conservation Laws*, J. Comp. Phys. , Vol. 49, 1983, pp. 357-393.

[80] Johnson, D.A., and King, L.S., *A Mathematically Simple Turbulence Closure Model for Attached and Separated Turbulent Boundary Layers*, AIAA Journal, Vol. 23, No. 11, Nov. 1985, pp. 1684-1692.

[81] Nakahashi, K., and Deiwert, G.S., *A Self-Adaptive-Grid Method with Application to Airfoil Flow*, AIAA Paper 85-1525-CP, 1985.

[82] Deiwert, G.S., Rothmund, H.J., and Nakahashi, K., *Simulation of Complex Three-Dimensional Flows*, NASA TM-86773, July 1985.

# Report Documentation Page

| 1. Report No. | 2. Government Accession No. | 3. Recipient's Catalog No. |
|---|---|---|
| NASA CR-4186 | | |

| 4. Title and Subtitle | 5. Report Date |
|---|---|
| Transonic Aeroelastic Analysis of Launch Vehicle Configurations | October 1988 |
| | 6. Performing Organization Code |

| 7. Author(s) | 8. Performing Organization Report No. |
|---|---|
| João Luiz Filgueiras de Azevedo | |
| | 10. Work Unit No. 505-63-21 |

| 9. Performing Organization Name and Address | 11. Contract or Grant No. |
|---|---|
| Stanford University<br>Dept. of Aeronautics and Astronautics<br>Stanford, CA 94305 | NGL 05-020-243 |
| | 13. Type of Report and Period Covered: Contractor Report |

| 12. Sponsoring Agency Name and Address | 14. Sponsoring Agency Code |
|---|---|
| National Aeronautics and Space Administration<br>Langley Research Center<br>Hampton, VA 23665-5225 | |

15. Supplementary Notes

Adapted from Ph.D. Dissertation, February 1988
Langley Technical Monitor: Robert V. Doggett, Jr.
Topical Report

16. Abstract

A numerical study of the aeroelastic stability of typical launch vehicle configurations in transonic flight is performed. Recent computational fluid dynamics techniques are used to simulate the transonic aerodynamic flowfields, as opposed to relying on experimental data for the unsteady aerodynamic pressures. The flow solver is coupled to an appropriate structural-dynamic representation of the vehicle.

The aerodynamic formulation is based on the thin layer approximation to the Reynolds-Averaged Navier-Stokes equations, where the account for turbulent mixing is done by the two-layer Baldwin and Lomax algebraic eddy viscosity model. The strucutral-dynamic equations are developed considering free-free flexural vibration of an elongated beam with variable properties and are cast in modal form. Aeroelastic analyses are performed by integrating simultaneously in time the two sets of equations. By tracing the growth or decay of a perturbed oscillation, the aeroelastic stability of a given configuration can be ascertained.

The method is described in detail, and results that indicate its application are presented. Applications include some validation cases for the algorithm developed, as well as the study of configurations known to have presented flutter programs in the past.

| 17. Key Words (Suggested by Author(s)) | 18. Distribution Statement |
|---|---|
| Aeroelasticity<br>Structural Dynamics<br>Launch Vehicles<br>Transonic Speeds | Unclassified - Unlimited<br>Subject Category 02 |

| 19. Security Classif. (of this report) | 20. Security Classif. (of this page) | 21. No. of pages | 22. Price |
|---|---|---|---|
| Unclassified | Unclassified | 168 | A08 |

NASA FORM 1626 OCT 86

NASA-Langley, 1988

For sale by the National Technical Information Service, Springfield, Virginia 22161-2171

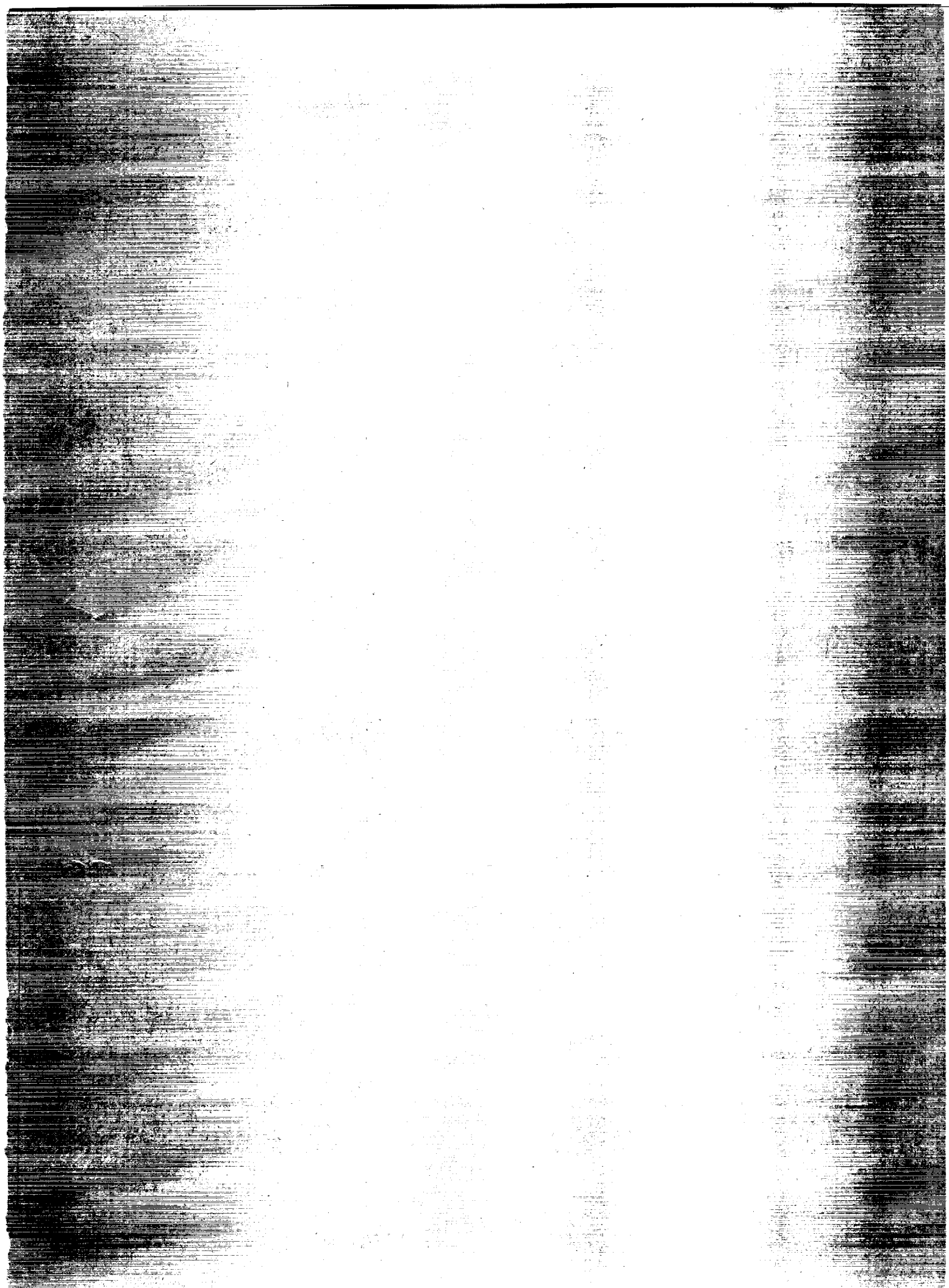

NASA

National Aeronautics and
Space Administration

Washington, D.C.
20546

Postage and Fees Paid
National Aeronautics and
Space Administration
NASA-451

Official Business
Penalty for Private Use $300

SPECIAL FOURTH CLASS MAIL
BOOK